AD-A248 505

||||||||||||||||||||||||

Defense Nuclear Agency
Alexandria, VA 22310-3398

DTIC
S ELECTE
APR 1992 D
C

DNA-TR-91-195

Instabilities and Turbulence in Intermediate Altitude Fireballs

Theodore C. Carney
Charles E. Needham
S-CUBED
Albuquerque Office
A Division of Maxwell Laboratories, Inc.
2501 Yale Boulevard, S.E., Suite 300
Albuquerque, NM 87106

April 1992

Technical Report

92-09496
||||||||||||||||||||||||

92 4 13 084

DISTRIBUTION LIST UPDATE

This mailer is provided to enable DNA to maintain current distribution lists for reports. We would appreciate your providing the requested information.

☐ Add the individual listed to your distribution list.

☐ Delete the cited organization/individual.

☐ Change of address.

> **NOTE:**
> *Please return the mailing label from the document so that any additions, changes, corrections or deletions can be made more easily.*

NAME: _____

ORGANIZATION: _____

OLD ADDRESS	CURRENT ADDRESS
_____	_____
_____	_____
_____	_____

TELEPHONE NUMBER: ( ) _____

SUBJECT AREA(s) OF INTEREST:

_____	_____
_____	_____
_____	_____

DNA OR OTHER GOVERNMENT CONTRACT NUMBER: _____

CERTIFICATION OF NEED-TO-KNOW BY GOVERNMENT SPONSOR (if other than DNA):

SPONSORING ORGANIZATION: _____

CONTRACTING OFFICER OR REPRESENTATIVE: _____

SIGNATURE: _____

CUT HERE AND RETURN

Director
Defense Nuclear Agency
ATTN: TITL
Washington, DC 20305-1000

REPORT DOCUMENTATION PAGE

Form Approved
OMB No. 0704-0188

1. AGENCY USE ONLY (Leave blank)	2. REPORT DATE	3. REPORT TYPE AND DATES COVERED
	920401	Technical 880502 – 900330

4. TITLE AND SUBTITLE

Instabilities and Turbulence in Intermediate Altitude Fireballs

5. FUNDING NUMBERS

C   - DNA 001-88-C-0031
PE - 62715H
PR - SA
TA - SA
WU - DH048170

6. AUTHOR(S)

Theodore C. Carney and Charles E. Needham

7. PERFORMING ORGANIZATION NAME(S) AND ADDRESS(ES)

S-CUBED
Albuquerque Office
A Division of Maxwell Laboratories, Inc.
2501 Yale Boulevard, S.E., Suite 300
Albuquerque, NM 87106

8. PERFORMING ORGANIZATION REPORT NUMBER

SSS-DTR-90-11647

9. SPONSORING/MONITORING AGENCY NAME(S) AND ADDRESS(ES)

Defense Nuclear Agency
6801 Telegraph Road
Alexandria, VA 22310-3398
RAAE/Berggren

10. SPONSORING/MONITORING AGENCY REPORT NUMBER

DNA-TR-91-195

11. SUPPLEMENTARY NOTES

This work was sponsored by the Defense Nuclear Agency under RDT&E RMC Code B7600D SA SA 00185 RAAE 3200A 25904D.

12a. DISTRIBUTION/AVAILABILITY STATEMENT

Approved for public release; distribution is unlimited.

12b. DISTRIBUTION CODE

13. ABSTRACT *(Maximum 200 words)*

Higher order and finely zoned calculations with the SHARC code have indicated that the tops of intermediate altitude fireballs are unstable. This report describes the characteristics of the instabilities and their evolution. To aid in the understanding and interpretation of the computed fireball instabilities, a number of idealized numerical experiments of the Rayleigh-Taylor and Richtmyer-Meshkow instabilities were completed. A strong zoning dependent numerical viscosity was noted. Results from the numerical experiments and their implications to fireball calculations are presented.

The current SHARC turbulence model, when applied to fireballs, generates few identifiable effects. However, evidence is provided that the model, as currently implemented, provides an inadequate treatment for flows in which the dominant turbulence generation mechanism is due to the interaction of the density and pressure fields. Steps are underway to provide a more general formulation of the model.

14. SUBJECT TERMS			15. NUMBER OF PAGES
Intermediate Altitude	SHARC Code	Turbulence Modeling	116
Nuclear Effects	Hydrodynamics	K-ε Turbulence Model	16. PRICE CODE
Instabilities	Fireball		

17. SECURITY CLASSIFICATION OF REPORT	18. SECURITY CLASSIFICATION OF THIS PAGE	19. SECURITY CLASSIFICATION OF ABSTRACT	20. LIMITATION OF ABSTRACT
UNCLASSIFIED	UNCLASSIFIED	UNCLASSIFIED	SAR

PREFACE

Accession For

NTIS GRA&I	☑
DTIC TAB	☐
Unannounced	☐
Justification	

By

Distribution/

Availability Codes

Dist | Avail and/or Special

A-1

CONVERSION TABLE

Conversion factors for U.S. Customary to metric (SI) units of measurement

MULTIPLY ⟶ BY ⟶ TO GET

TO GET ⟵ BY ⟵ DIVIDE

angstrom	$1.000\,000 \times E\,-10$	Meters (m)
atmosphere (normal)	$1.013\,25 \times E\,+2$	Kilo pascal (kPa)
bar	$1.000\,000 \times E\,+2$	Kilo pascal (kPa)
barn	$1.000\,000 \times E\,-28$	meter^2 (m^2)
British thermal unit (thermochemical)	$1.054\,350 \times E\,+3$	joule (J)
cal (thermochemical)/cm^2	$4.184\,000 \times E\,-2$	mega joule/m^2 (MJ/m^2)
calorie (thermochemical)	$4.184\,000$	joule (J)
calorie (thermochemical/g)	$4.184\,000 \times E\,-3$	joule per kilogram (J/kg)
curies	$3.700\,000 \times E\,+1$	giga becquerel (Gbc)*
degree Celsius	$t_K = t^o{}_K + 273.15$	degree kelvin (K)
degree (angle)	$1.745\,329 \times E\,-2$	radian (rad)
degree Fahrenheit	$t_K = t^o{}_K + 459.67/1.8$	degree kelvin (K)
electron voit	$1.602\,19 \times E\,-19$	joule (J)
erg	$1.000\,000 \times E\,-7$	joule (J)
erg/second	$1.000\,000 \times E\,-7$	watt (W)
foot	$3.048\,000 \times E\,-1$	meter (m)
foot-pound-force	$1.355\,818$	joule (J)
gallon (U.S. liquid)	$3.785\,412 \times E\,-3$	meter^3 (m^3)
inch	$2.540\,000 \times E\,-2$	meter (m)
jerk	$1.000\,000 \times E\,+9$	joule (J)
joule/kilogram (J/kg) (radiation dose absorbed)	$1.000\,000$	gray (Gy)
kilotons	4.183	terajoules
kip (1000 lbf)	$4.448\,222 \times E\,+3$	newton (N)
kip/inch^2 (ksi)	$6.894\,757 \times E\,+3$	kilo pascal (kPa)
ktap	$1.000\,000 \times E\,+2$	newton-second/m^2 (N-s/m^2)
micron	$1.000\,000 \times E\,-6$	meter (m)
mil	$2.540\,000 \times E\,-5$	meter (m)
mile (international)	$1.609\,344 \times E\,+3$	meter (m)
ounce	$2.934\,952 \times E\,-2$	kilogram (kg)
pound-force (lbf avoirdupois)	$4.448\,222$	newton (N)
pound-force inch	$1.129\,848 \times E\,-1$	newton-meter (N. m)
pound-force/inch	$1.751\,268 \times E\,+2$	newton/meter (N/m)
pound-force/foot^2	$4.788\,026 \times E\,-2$	kilo pascal (kPa)
pound-force/inch^2 (psi)	$6.894\,757$	kilo pascal (kPa)
pound-mass (lbm avoirdupois)	$4.535\,924 \times E\,-1$	kilogram (kg)
pound-mass-foot^2 (moment of inertia)	$4.214\,011 \times E\,-2$	kilogram-meter^2 (kg. m^2)
pound/mass/foot^3	$1.061\,846 \times E\,+1$	kilogram-meter^3 (kg/m^3)
rad (radiation dose absorbed)	$1.000\,000 \times E\,-2$	gray (Gy)**
roentgen	$2.579\,760 \times E\,-4$	coulomb/kilogram (C/kg)
shake	$1.000\,000 \times E\,-8$	second (s)
slug	$1.459\,390 \times E\,-1$	kilogram (kg)
torr (mm Hg, 0°C)	$1.333\,22 \times E\,-1$	kilo pascal (kPa)

* The becquerel (Bq) is the SI unit of radioactivity; 1 Bq =1 event/s.

** The Gray (Gy) is the SI unit of absorbed radiation.

TABLE OF CONTENTS

TABLE OF CONTENTS (Continued)

LIST OF ILLUSTRATIONS

LIST OF ILLUSTRATIONS (Continued)

SECTION 1
INTRODUCTION

Hydrocodes have been applied to problems of nuclear fireball evolution for many years. As the codes and the computers on which they ran became more robust, and their builders and users more experienced, the calculations have become quite successful in modeling observed fireball behavior. With realistic initial conditions, equations-of-state, and ambient atmosphere models, modern codes are capable of reasonable predictions of fireball growth and rise rates, debris distributions, and shock/fireball interactions. Given this success and current interest in the structured environment of intermediate altitude fireballs, it was natural to attempt calculations at even higher resolution.

Early hydrocodes were first order and therefore, diffusive. As a consequence, their solutions were usually "smooth". In the quest for ever higher resolution, and to control numerical diffusion prior to turbulence modeling, modern codes are employing improved numerics. SHARC (S-CUBED Hydrodynamic Advanced Research Code) has kept pace. Within the past two years, its first phase (a Lagrangian advancement of the momentum and energy equations) was modified for improved accuracy and its second phase (remap of mass, momentum and energy) was replaced with a second order algorithm. During this same period, a turbulence option employing a K-ε model was also incorporated. Application of the improved models to fireballs has yielded some unexpected results, specifically, the development of large scale structures.

Simply stated, the second order results differ considerably from previous first order results and are quite sensitive to seemingly slight changes in the implementation of the numerics. One major consequence of the less diffusive numerics is that pressure and density gradients are maintained to the extent that conditions are favored for the growth of instabilities. Our current turbulence model has not significantly altered the evolution of the instabilities.

Higher order calculations with SHARC indicate that intermediate altitude fireballs are unstable. This report describes the characteristics of the instabilities, the conditions necessary for their formation, and their evolution in time. In the process of interpreting these results we completed a series of calculations of known instabilities to characterize the interaction between zoning and higher order differencing. Time and budgetary restrictions have prevented the expenditure of the level of effort necessary to fully explore the results.

1

The numerical experiments which demonstrate the response of finite difference codes to known instabilities are described in Section 2. In Section 3 we describe the characteristics and evolution of our computed fireball instabilities. Section 4 discusses the S-CUBED turbulence model and the results of its application to fireballs. Section 5 provides a summary, conclusions and recommendations for further research.

SECTION 2
NUMERICAL EXPERIMENTS

The instabilities observed in the SHARC fireball calculations developed in relatively complex flows involving large density differences, possible effects due to compressibility, an imposed length scale due to atmospheric gradients, and curved streamlines. To aid our understanding of the development and growth of instabilities we completed a series of calculations of unstable flows in planar geometries. Although we gained considerable insight through these efforts, we raised not a few unresolved questions.

The Rayleigh-Taylor instability (Chandrasekhar, 1981; Sharp, 1984) occurs in regions where the pressure and density gradients are of opposite sign. Large gradients favor its formation and growth. The best known and most studied example is where a lighter fluid is attempting to support a fluid of greater density against gravity. The slightest perturbation causes the surface to rapidly deform and the fluids to exchange places. Another unstable example from gas dynamics occurs when a shock accelerates a light fluid into a heavier fluid. The resulting instability is known as the Richtmyer-Meshkov or shock excited Rayleigh-Taylor instability (Richtmyer, 1960; Sturtevant, 1987). Examples of calculations from both instabilities are presented in this section. Calculations of idealized Kelvin-Helmholtz unstable flows were also planned but not undertaken due to budgetary constraints.

2.1 DISPERSION RELATION.

Consider two uniform, viscous, incompressible fluids in a gravitational field. The fluids are separated by a horizontal interface that is perturbed in amplitude by a disturbance of wave number k. The density of the upper fluid is ρ_1 and the density of the lower fluid is ρ_2. Linear, small amplitude theory shows that the disturbance amplitude Y satisfies the equation

$$\frac{dY}{dt} = nY. \tag{1}$$

where t is time and n is growth rate. Chandrasekhar (1981) provides a thorough analysis of this situation and a rather complex dispersion relation for the growth rate. Duff (1962) gives the following approximation:

3

$$n = (Agk + \nu^2 k^4)^{1/2} - \nu k^2. \tag{2}$$

where n is the growth rate, A the Atwood number = $(\rho_1 - \rho_2)/(\rho_1 + \rho_2)$, g is gravitational acceleration, k is the wave number and ν is the kinematic viscosity. Equation (2) has the same asymptotic limits as the expression by Chandrasekhar, namely

$$n^2 \rightarrow Agk \quad (k{\rightarrow}0) \quad n \rightarrow \frac{A}{2k} \quad (k{\rightarrow}\infty) \tag{3}$$

and approximately the same maximum growth $(=n_m)$ at the most unstable wave number $(=k_m)$. Expressions for n_m and k_m are given below:

$$n_m = \frac{(Ag)^{2/3}}{2\nu^{1/3}}, \quad km = \frac{1}{2}\left(\frac{Ag}{\nu^2}\right)^{1/3}. \tag{4}$$

2.2 GRAVITATIONAL EXCHANGE RAYLEIGH-TAYLOR EXPERIMENTS.

The CLOUD code (Libersky, 1983) was used to simulate the gravity driven rollup of the unstable interface between a heavy fluid overlaying a lighter one. CLOUD is a finite difference, incompressible (anelastic approximation), hydrocode formulated with the stream-function / vorticity transport equations. Its main advantage over SHARC is that it is extremely fast (5μ s/(cell-cycle). Its use for these calculations was many times more economical than a similar set completed with the fully compressible SHARC code because the latter's time step would have been limited by sound speed. It was felt, however, that the CLOUD response would be similar to that from SHARC because they use essentially the same advection algorithm. The assumption here is that numerical diffusion in the advection phase is the major source of departure from the inviscid growth rate.

Two groups of calculations, differing in the way the interface was perturbed, were completed with the CLOUD code. In the first group, the interface was initialized as a sinusoid of finite amplitude. In the second, the interface was initially flat and the surface disturbance was allowed to develop in time by means of a sinusoidal velocity perturbation that was normal to the interface. Figures 1a and 1b, respectively, illustrate the geometries.

4
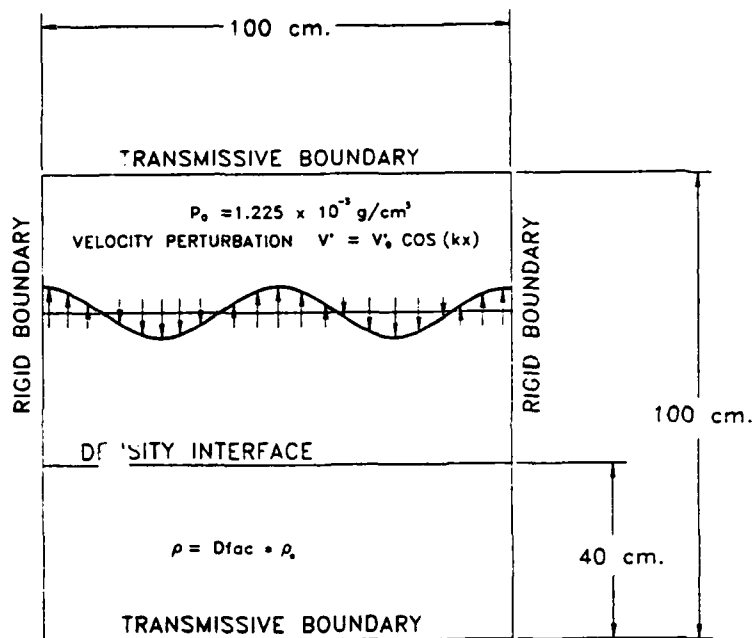
1a. Infinitesimal initial disturbance.
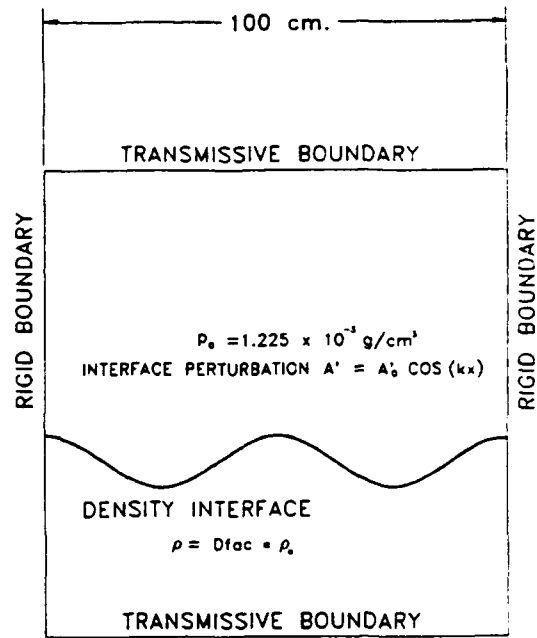
1b. Finite initial disturbance.
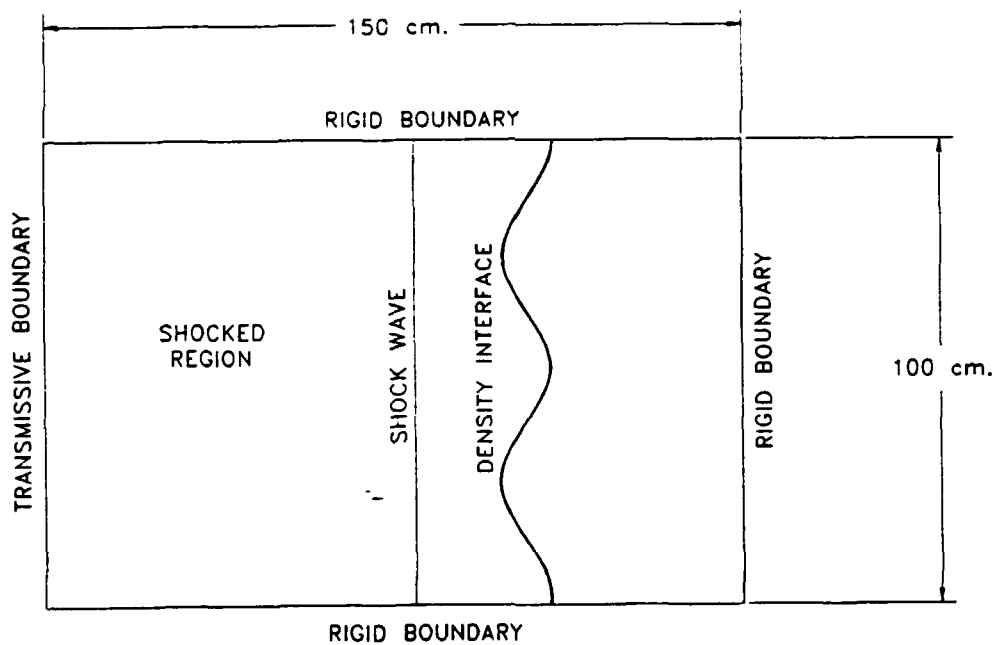
1c. Richtmyer-Meskov

Figure 1. Calculational geometry and setup.

Each group included a series of calculations at several different resolutions; three for the finite initial disturbance and four for the infinitesimal initial disturbance. Within each series of calculations, the wave number of the applied perturbation was varied from $\pi/25$ to $\pi/2$. Both groups of calculations were completed in a two-dimensional Cartesian mesh 100 by 100 cm on a side. All calculations were completed at an Atwood number of 0.053 (density ratio of 0.9) and the density of the upper gas was 1.225×10^{-3} gm/cc. Tables 1 summarizes the zoning and the initial interface conditions.

Table 1.   Initialization summary - finite amplitude disturbance.

Zoning	Zone size	Initial amplitude
50 x 50	2.0 cm	2 zones
100 x 100	1.0 cm	4 zones
100 x 100	1.0 cm	2 zones
200 x 200	0.5 cm	1 zone

Table 1.   Initialization summary - infinitesimal disturbance.

Zoning	Zone size	Initial velocity
50 x 50	2.0 cm	0.1 cm/s
76 x 76	1.3 cm	0.1 cm/s
100 x 100	1.0 cm	0.1 cm/s
200 x 200	0.5 cm	0.1 cm/s

During each cycle of each calculation, the mesh was searched for the top and bottom of the crests in the mixing region and this information, along with the time, was written to a file. Subsequent to the calculation, a least-squares fit of exponential form $(y = a \bullet \exp(n \bullet T))$ was applied to the data to determine the growth rate n. Equation 2 was then solved for the effective viscosity.

The calculations that were initialized with an infinitesimal disturbance did not respond until the surface had been sufficiently deformed by the perturbation velocity. For these calculations, the time scale was shifted by the startup time before fitting and in addition,

the "a" term from the fit was interpreted as the minimum perturbation amplitude capable of being seen by the code.

Before presenting the growth rate results, it is instructive to discuss qualitatively the effects of zoning on the evolution of the interface. Appendices A through D show the time evolution of the interface growth for several wave numbers from calculations initialized with finite amplitude disturbances. The reader is referred to Table 2 for the contents of the appendices.

Table 2. Appendix contents.

Appendix	Problem zoning
A	50 x 50 - 2 zone amplitude
B	100 x 100 - 1 zone amplitude
C	100 x 100 - 2 zone amplitude
D	200 x 200 - 4 zone amplitude

It is clear from the plots in the appendices that, for the same wave number disturbance, problems zoned differently evolve differently. This is contrary to the lore from the days of first order codes, which proposed that continued doubling of resolution would lead to convergence.

Several processes contribute to the observed results. The first and most basic is that, although the calculations were nominally initialized with the same wave number disturbance, finite zoning resulted in the introduction of components of higher frequency. Differences evolve because variations in zoning result in variations in the dissipative and dispersive characteristics of the advection. The resulting differences in the density field then feed back to the driving terms and the solutions further diverge.

The center-concave crests in the 100 x 100 calculations at small wave numbers and the corresponding center-convex crests in the 200 x 200 zone calculations are particularly striking. Also of note are the high frequency features at edges of the waves in the most finely zoned calculations and the aliasing at the higher wave numbers.

Figure 2 compares the growth rates determined from the calculations with a finite initial disturbance with those computed from the calculations initialized with a flat interface.
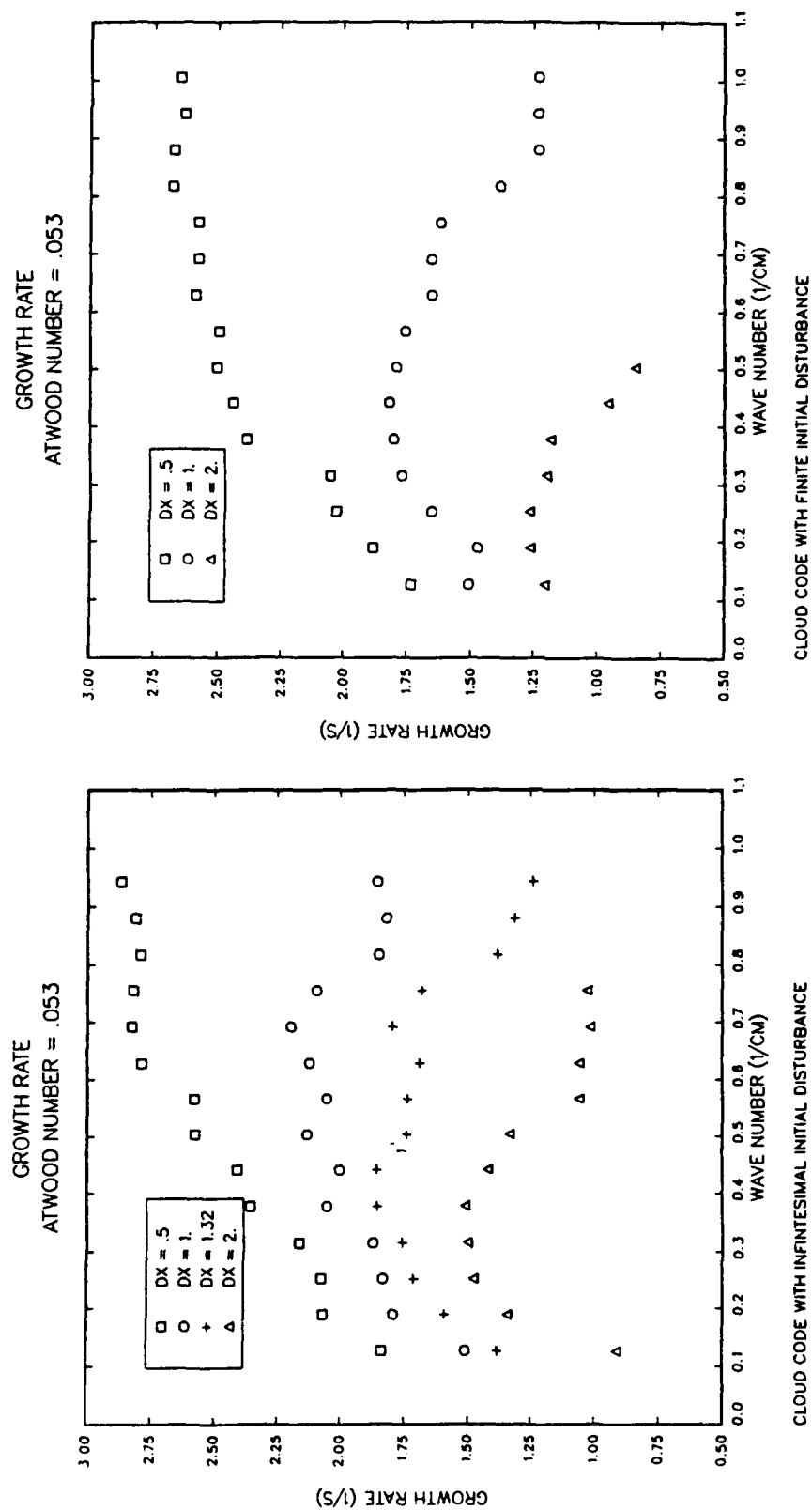
Figure 2. Growth rates from Rayleigh-Taylor calculations.

The results are remarkably similar although a clear trend indicates that, for a given wave number and zoning, the calculations initialized with a flat interface had the highest growth rates. Figure 3 exhibits the same data in non-dimensional form and indicates that, in non-dimensional space, the results essentially collapse to a line. In these plots, the growth rates were made dimensionless by dividing by the inviscid growth rate $(Agk)^{1/2}$. Dimensionless wave numbers were formed by expressing them as $dx/\lambda = 2\pi dx/k$, where λ is the wavelength of the imposed disturbance. The dimensionless wave number is inversely proportional to the number of zones across a wavelength and is indicative of how well the driving disturbance is resolved.

The version of CLOUD used in this series of calculations was inviscid. That is, no viscous terms were included in the governing equations. The non-ideal response of the code, however, can be interpreted by means of an apparent viscosity through Equation 2. Figure 4 shows the apparent viscosity plotted against dimensionless wave number for both series of calculations and indicates that less resolved zoning results in a correspondingly high apparent mesh viscosity. Figure 5 shows the same information plotted in terms of a disturbance Reynolds number $= n/vk^2$ (Yih, 1988).

Most disturbing (confusing) about these results is the high apparent viscosity at the smaller wave numbers. Examination of Equation 3 indicates that for small wave numbers, the growth rates should approach the inviscid rates. Chandrasekhar (1981) stresses this point and states "viscosity plays no role among the very long wavelengths". Several factors, acting alone or in concert, have been identified that can contribute to the observed disparity between theory and our numerical results.

The first involves the possibility that equation 2 isn't adequate for our analysis and that perhaps a more complicated model such as the diffusion analysis of Duff (1962) should be employed. For example, Duff shows that diffusion decreases the amplitude of mean density. This effectively reduces the horizontal gradients, and therefore, the driving mechanism for vorticity generation (g dp/dx). For poorly resolved (in amplitude) disturbances, this leads to strong damping. The same mechanism is also active for long wavelengths because the code responds to a surface of large radius-of-curvature as if it were flat. For sinusoids, the largest radii-of-curvature occur at the crests.
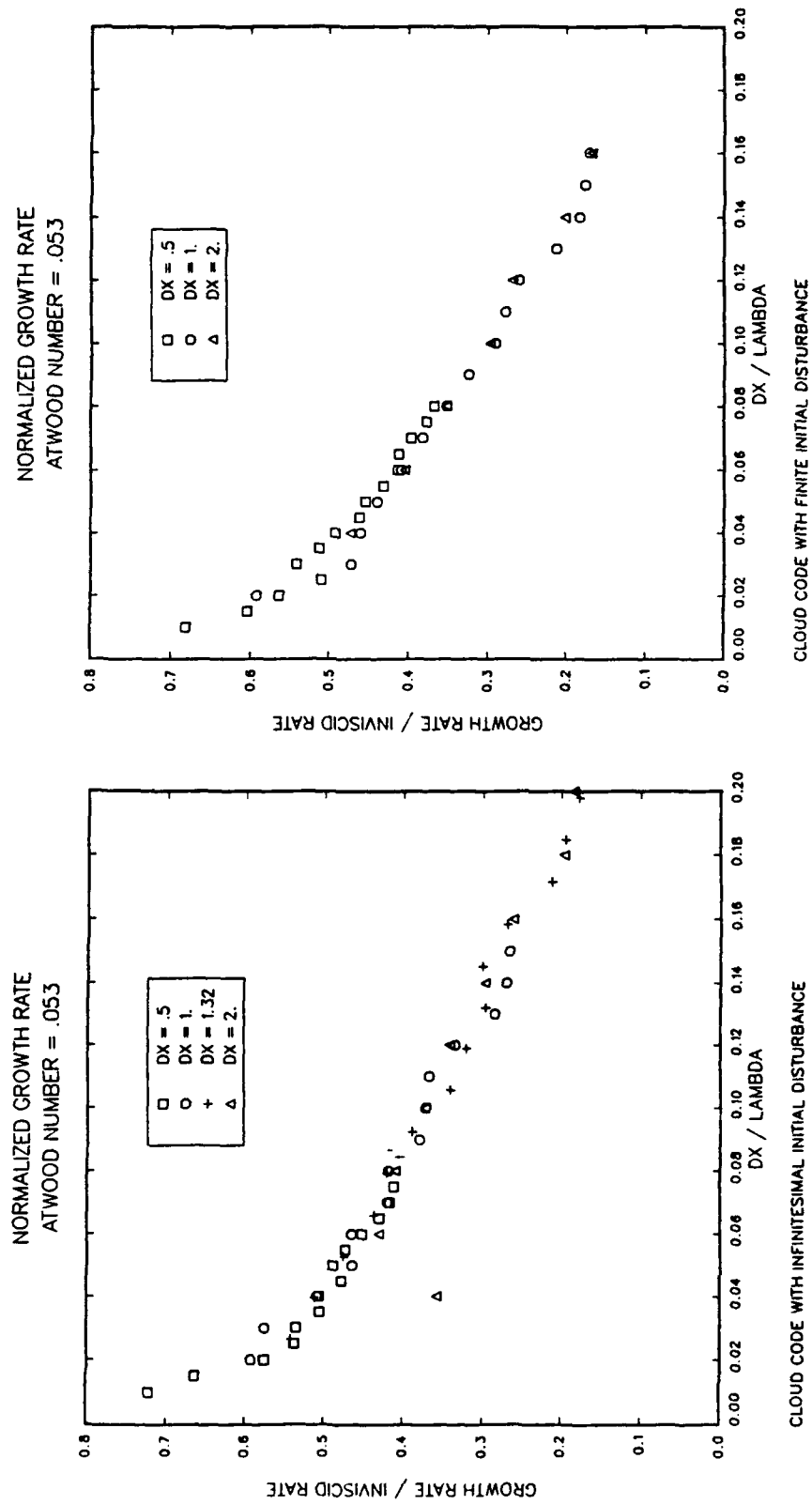
Figure 3. Dimensionless growth rates from Rayleigh-Taylor calculations.
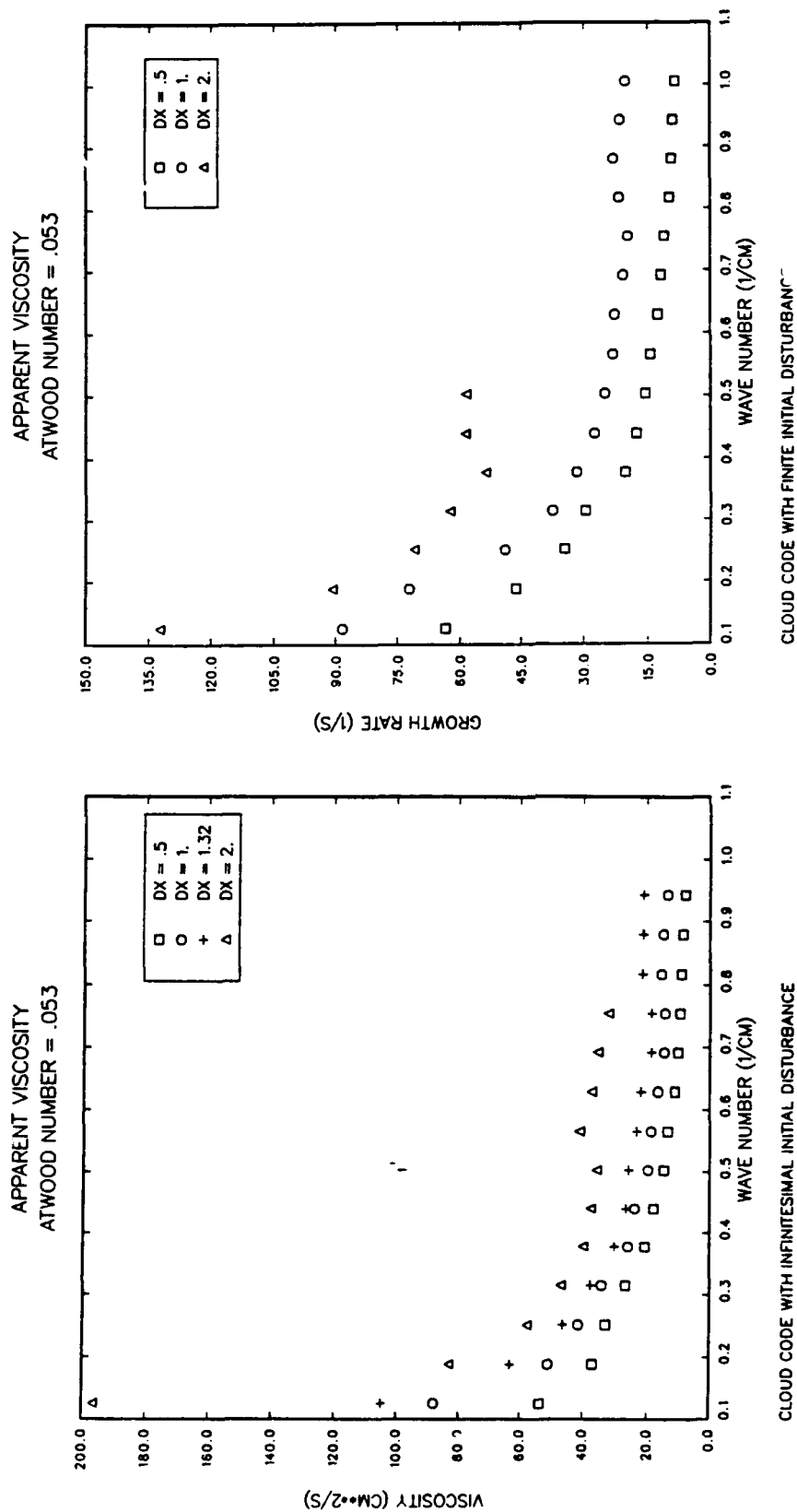
10

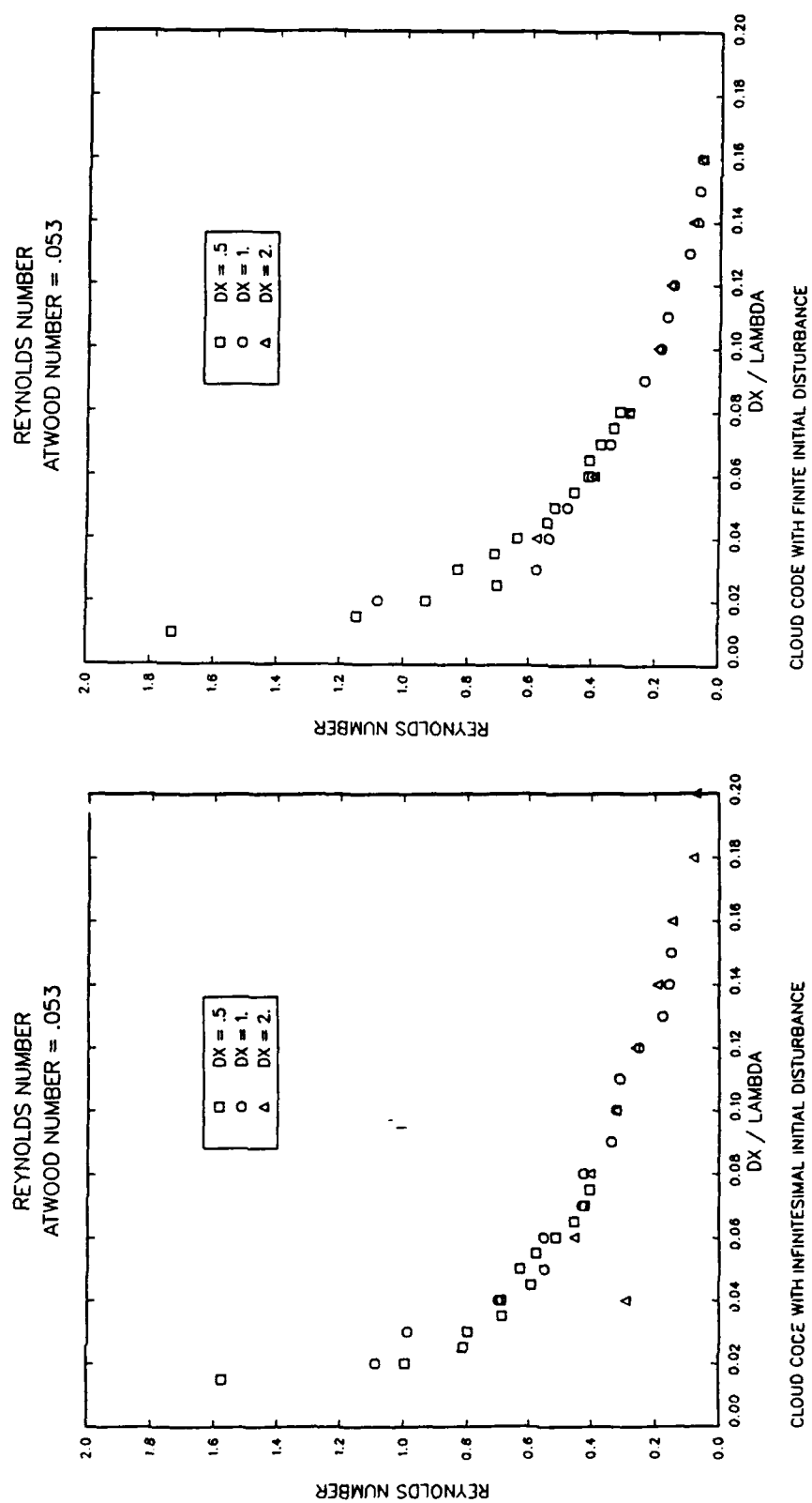Figure 4. Viscosity from Rayleigh-Taylor calculations.

Figure 5. Reynolds number from Rayleigh-Taylor calcul..tions.

A second possibility involves the fact that, because inviscid growth rates are small for small wave numbers, a systematic error in the procedures for growth rate determination could result in a large apparent viscosity. One source of systematic error that was considered pertained to the magnitude of the amplitudes used in the analysis. The validity of linear theory is based on the assumption that $YK<<1$, although Jacobs and Catton (1988,2) observed that good agreement between theory and experiment is obtained for values of $YK=1$. Our analysis used values of $YK<\pi$ to obtain sufficient data for fitting at large wave numbers. Growth rate comparisons with results obtained for $YK<1$ showed little difference, however.

For the calculations initialized with a flat interface, the two parameter least-squares fit yields, in addition to the growth rate, a number that can be interpreted as the minimum disturbance amplitude sensed by the code. These results, shown in Figure 6, indicate that CLOUD responds to signals that are approximately 0.7 of cell size. The shallow slope indicates that there is a slight trend towards a larger ratio as the signal becomes less resolved.

The plots in Appendices B and C show the interface evolution for identically zoned calculations that were initialized with amplitudes of two and four zone heights. Growth rate results from these calculations are displayed in Figure 7 and indicate that the interface perturbations that were initially better resolved were deformed at a slower rate. Equation 1 (and perhaps, one's intuition) says the opposite.

Although we have no clear explanation, we suspect the discrepancy is caused by an incomplete initialization of the problem. We failed to include the initial velocity field associated with the finite amplitude disturbance. These comments also offer an explanation as to why the largest growth rates were noted in calculations in which interface was allowed to grow from an undisturbed state.

2.3 RICHTMYER-MESHKOV EXPERIMENTS.

The SHARC code was used to demonstrate the response of a fully compressible finite-difference hydrocode to a hydrodynamically unstable interface. Figure 1c shows the computational setup within the two-dimensional Cartesian mesh. In all calculations, a Mach 1.25 shock was driven from a light gas into a heavy gas through an interface that was perturbed in amplitude by a disturbance of wave number k. The shock, traveling from left to right, was initialized 20 zones to the left of the interface and was continuously fed from
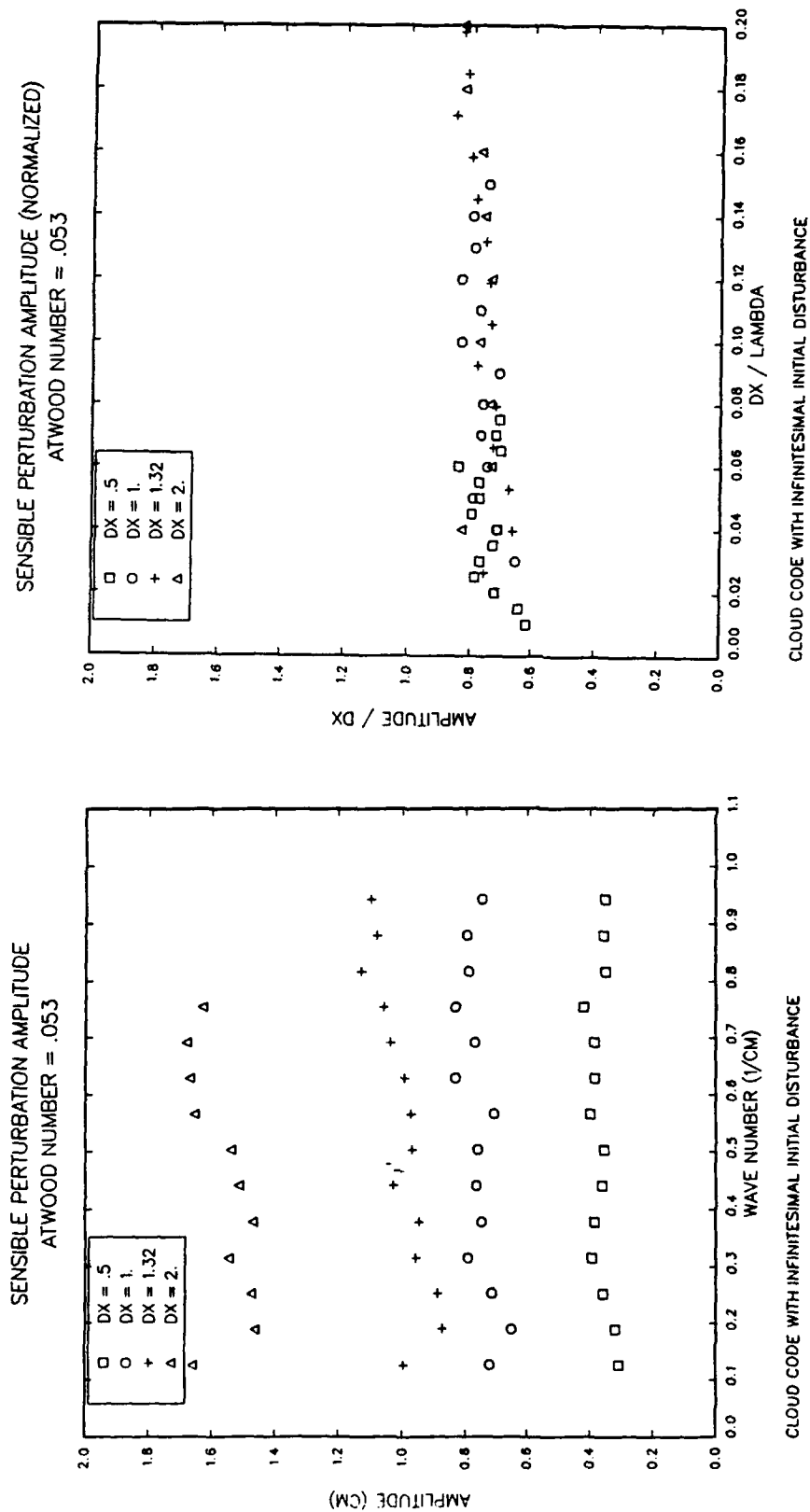
13

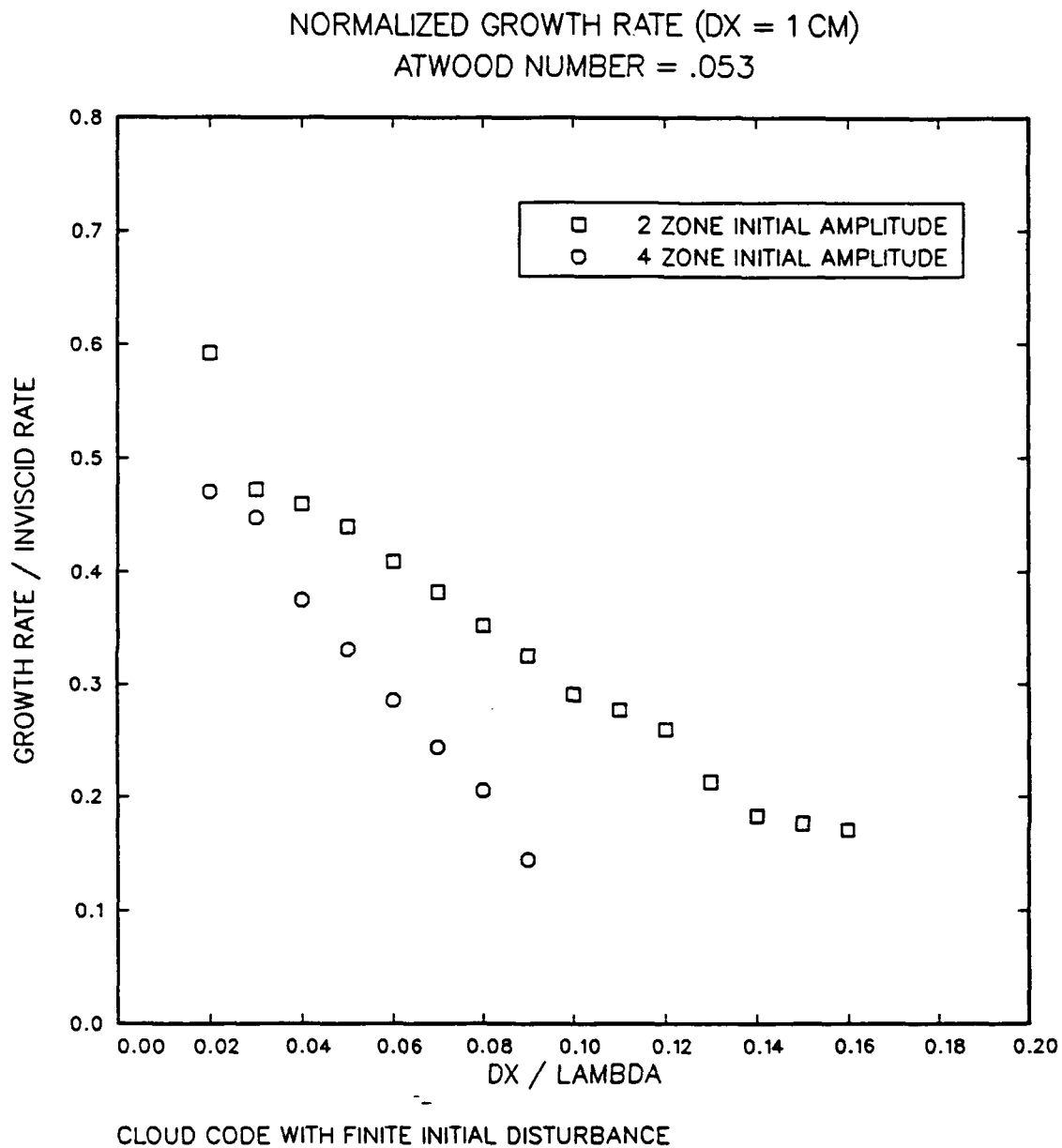Figure 6. Sensible amplitude from Rayleigh-Taylor calcuations.

Figure 7. Effect of initial amplitude on dimensionless growth rates -
Rayleigh-Taylor calculations.

the left boundary. The Atwood ratio, based on the density behind the shock (ρ_2) and the unshocked density (1.225×10^{-3} g/cc) to the right of the interface (ρ_1) was 0.91. Analogous to the CLOUD calculations, the zonal resolution and the wave number of the applied disturbance were varied to determine their effects on the growth rate of the disturbance. Table 3 summarizes the zoning and initial disturbance amplitude.

Table 3. Initialization summary - Richtmyer-Meshkov experiments.

Zoning	Zone size	Initial amplitude
76 x 50	2.0 cm	2 zones
150 x 100	1.0 cm	2 zones
300 x 200	0.5 cm	4 zones

Sturtevant (1987) and Youngs (1984) have presented analyses of the Richtmyer-Meshkov instability. Sturtevant's work was experimentally based; Youngs numerical. Both employed Richtmyer's (1960) results that showed "if the initial compression of the interface and of the fluids is taken into account, the ultimate rate of growth of the corrugation agrees, to within 5 to 10 percent, with that given by the incompressible theory." Because the shock induced acceleration of the interface is short lived, $g = U_I \delta t$ and Equation 1 becomes for the impulsive case

$$\frac{dY}{dt} = kU_I A Y'$$

(5)

where U_I is the post shock mean velocity of the interface and Y' is the post shock amplitude of the initial disturbance. "Thus in the impulsive case the growth is linear in time rather than exponential, and acceleration in either direction leads to unbounded growth." (Sturtevant, 1987). Considerable ambiguity exists for choosing Y' and U_I as there exist two time scales for the interaction of the shock with the interface, one in the fast gas and one in the slow. We used the small compression model described in Sturtevant for the post shock amplitude

$$\frac{Y'}{Y_0} = 1 - \frac{U_I}{U_s}.$$

(6)

16

where U_s is the incident shock velocity and Y_o is the initial perturbation amplitude. For U_I we used 2.2×10^4 cm/s, a value numerically and theoretically determined for a flat interface. No correction for the Atwood number was applied because Sturtevant indicates that the post-shock Atwood ratio is not much different from the pre-shock, even for strong shocks.

Appendices E through G show the time evolution of the interface growth for several wave numbers from calculations zoned with 2 cm, 1 cm, and 0.5 cm resolution. Clearly, the more finely-zoned calculations do a better job in maintaining gradients. Little difference is evident in the amplitudes of the corrugations in the calculations with 0.5 and 1.0 cm resolution; both of which were initialized with an amplitude of 2.0 cm.

The calculations with 2.0 cm resolution were initialized with a disturbance amplitude of 4.0 cm. For these, the absolute amplitudes remained greater, especially in the high density fingers, but the growth rates were smaller.

Growth rates were determined for each calculation using procedures similar to those described for the Rayleigh-Taylor experiments. A linear least squares fit, instead of the previously used exponential fit, was employed in accordance with Equation 5. Figure 8 summarizes the growth rate data for the three levels of resolution used in the calculations in dimensional and non-dimensional form. Considerable scatter is evident and the results in non-dimensional form do not collapse to a line. Equation 5 indicates that the calculations with the larger initial perturbation (2 cm resolution) should have exhibited the highest growth rates. Because they did not, we conclude that the growth rate differences are due to resolution.

2.4 DISCUSSION.

The methodology presented in Sections 2.2 and 2.3 provides a means for quantifying the non-ideal response characteristics of hydrocodes. A discussion of growth rate effects alone, however, is incomplete. In fact, growth rate errors are symptoms of more basic errors. Some sources of these errors are briefly discussed in this section. Rood (1987) provides a thorough review of the problems associated with advection algorithms and the attempts that have been made to reduce these errors. Much of the material in the next few paragraphs is based on that article. Material in quotes is taken verbatim.

RICHTMYER–MESHKOV INSTABILITY
MACH NO. = 1.25, ATWOOD NO. = .91
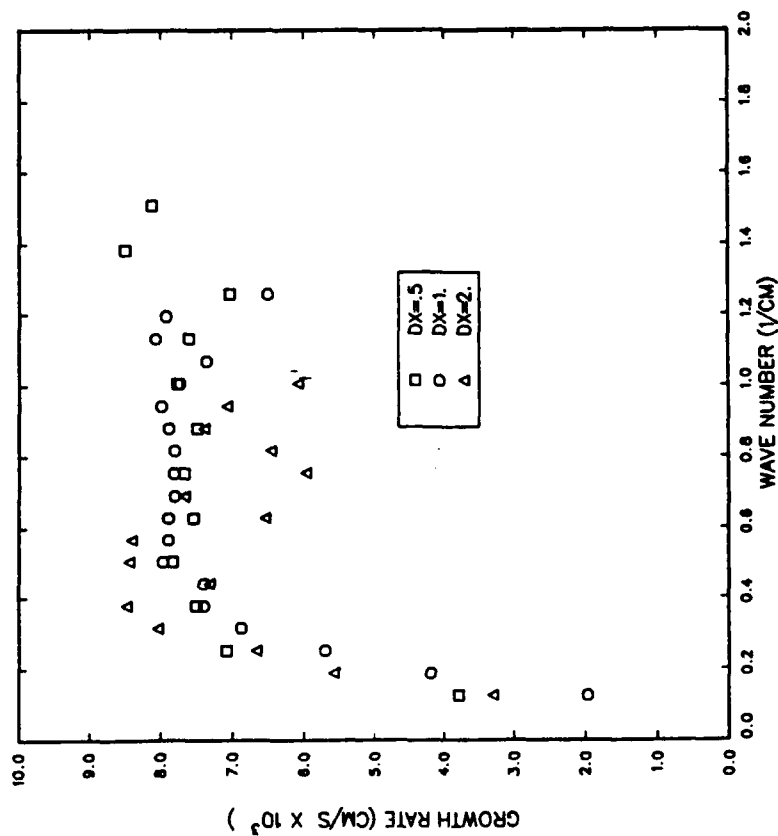
RICHTMYER–MESHKOV INSTABILITY
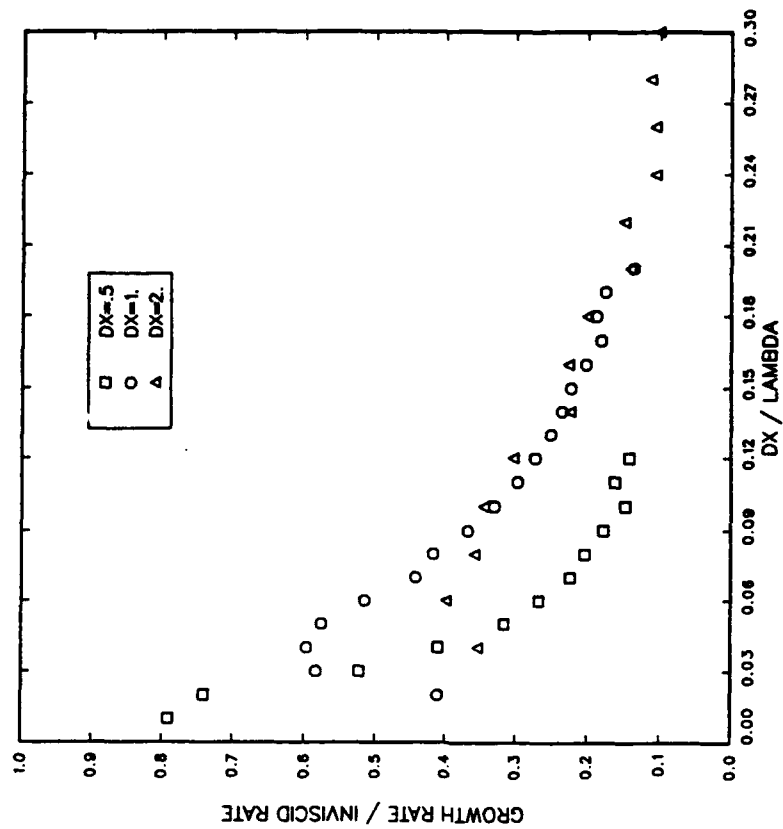MACH NO. = 1.25, ATWOOD NO. = .91

Figure 8. Growth rates from Richtmyer-Meshkov calculations.

18

Numerical advection algorithms are subject to both dissipation and dispersion errors. Dispersion errors cause the production of small waves and results "from different Fourier components of the original distribution propagating at different phase speeds." Dissipation errors exhibit many of the properties of diffusion and this diffusion, in some contexts, can dominate the problem. "Odd order schemes tend to be diffusive and even order dispersive."

Advection algorithms are also subject to aliasing errors which arise "when it is attempted to resolve high wave number features on a grid that is too coarse to resolve the features." Aliasing errors cause the reflection of higher frequency energy into lower frequencies; errors which are evident in some of the plots in the appendices to this report.

The advection algorithms used in the SHARC and CLOUD codes are monotone. That is, they are designed to prevent the generation of new maxima or minima, and thus reduce dispersion errors. However, Rood (1987) quotes that "no linear scheme of second order or higher accuracy can be made free from dispersion errors." Because phase errors are worse for poorly resolved wavelengths, "distributions that are rich in high wave number components, high-order accurate differencing may reduce the accuracy of the solution."

With the above comments in mind, "it can be argued that the short wavelengths should be selectively diffused to eliminate those modes which are not accurately modeled." This implies that for modes which approach the resolution of the mesh, subscale turbulence modeling must be invoked to represent subscale process. Rood (1987) calls physical diffusion "an essential mechanism in any transport model." A turbulence model was not invoked in any of the numerical experiments discussed here.

Sharp (1984) states his belief that a Rayleigh-Taylor unstable interface is subject to the Kelvin-Helmholtz instability and he poses the question as to whether this property might eventually lead to the late time self-similarity and independence from initial conditions noted by Youngs (1984). The finely resolved calculations presented in Appendix D show the formation of unstable regions at the edge of the spikes that might result from a Kelvin-Helmholtz instability. Future work could address this question specifically. Another physical source for these features could be the baroclinic generation of vorticity due to density gradients normal to the gravitational field. This mechanism has been noted previously by Klaassen and Clark (1985) and Grabowski (1989).

Close inspection of the plots from the high resolution, long-wavelength CLOUD calculations reveals that fine scale structure was evident at problem initialization. This indicates that, if the late time structure developed from these features, some sort of scale dependent filter (read diffusion) would be necessary to suppress their growth. However, it is likely that both processes, the physical mechanisms mentioned in the preceding paragraph, and the errors due to advection and initialization, contributed to the development of the observed structure. This makes specification of the diffusion model more difficult, especially if the response was driven mainly by initialization errors.

Features similar to the center concave corrugations evident in the long- wavelength calculations at 1 cm resolution were noted in the cumulus cloud calculations of Klaassen and Clark (1985). These authors also noted an associated downdraft that was not evident in the current calculations. As mentioned earlier, we suspect the initialization procedures in the current calculations introduced wave number components that grew at differential rates.

SECTION 3
INTERMEDIATE ALTITUDE FIREBALL INSTABILITIES

Calculations with the SHARC code indicate that the tops of intermediate altitude fireballs are unstable. These results contrast with prior first order results which, except for a few instances, revealed a smooth evolution in time. This section reviews the development and evolution of the instabilities in calculations of buoyant, transitional, and fully ballistic fireballs. Where possible, knowledge and experience gained from the idealized numerical experiments in the previous section is applied.

The plots in Appendix H demonstrate the development of instabilities in a calculation of 200 KT at 50 km. First order results are provided for comparison. Differences are readily apparent, most noticeably in the development of structure at the fireball edge and in the definition of the torus region. Also note the enhanced gradients at the fireball top and side. Although the differences shown in the appendix are specific to one yield and height-of-burst combination, they are typical of those seen in other similar comparisons involving buoyant and transitionally ballistic fireballs.

Figure 9 shows the computed time development of the fireball from the same calculation of 200 KT at 50 km. The secondary thermal which develops at the fireball top subsequent to 50 seconds has not been noted in any prior calculation of this yield and height-of-burst combination. Figures 10 and 11 present comparable plots for calculations of 4 MT at 45 km and 1 MT at 60 km, respectively. The 1 MT calculation employed non-equilibrium chemistry. The other two were completed with an equilibrium equation-of-state.

One trend identified in viewing Figures 9 through 11 is that the tangential length scale (with respect to the fireball diameter) of the structures at the fireball tops decreases as the height-of-burst is increased. In addition, the largest growth rates are experienced directly at the fireball top for the two lowest bursts. For the 60 km scenario, the largest growth rates develop slightly off axis. The fireball top deformities evident in the plots are similar to those shown by Klaassen and Clark (1985) in their cumulus cloud calculations. The latter, however, were limited to thermodynamic and moisture fields and were later shown (Grabowski, 1989) to result from advection errors.

We speculate that the instabilities noted in the SHARC calculations are not numerical artifacts but result as the code attempts to respond to true hydrodynamically unstable
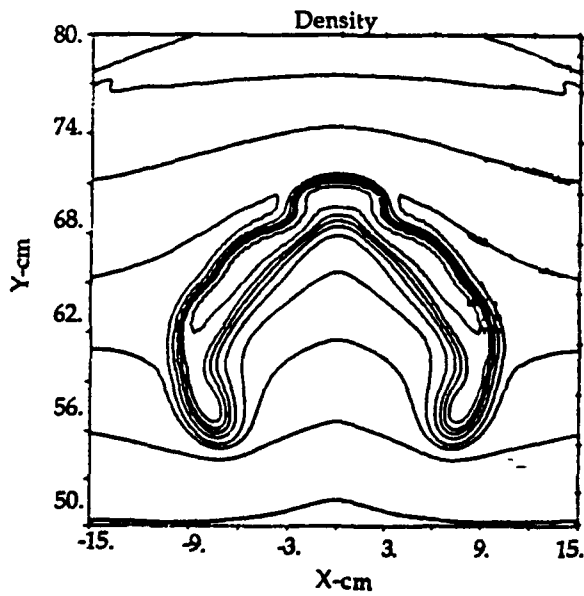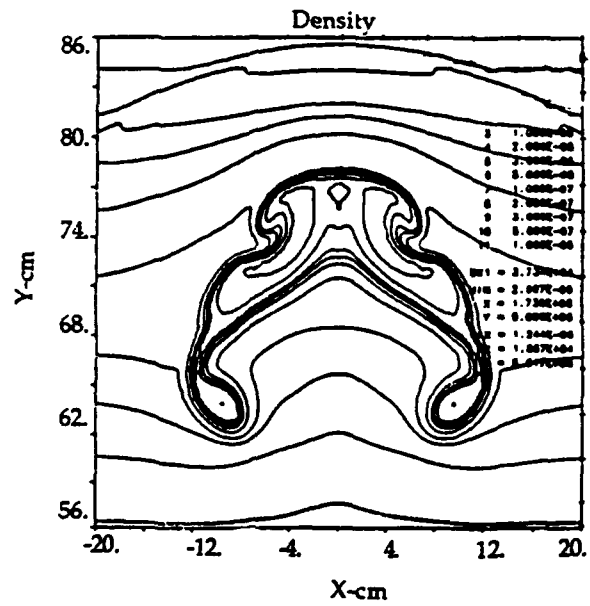
21
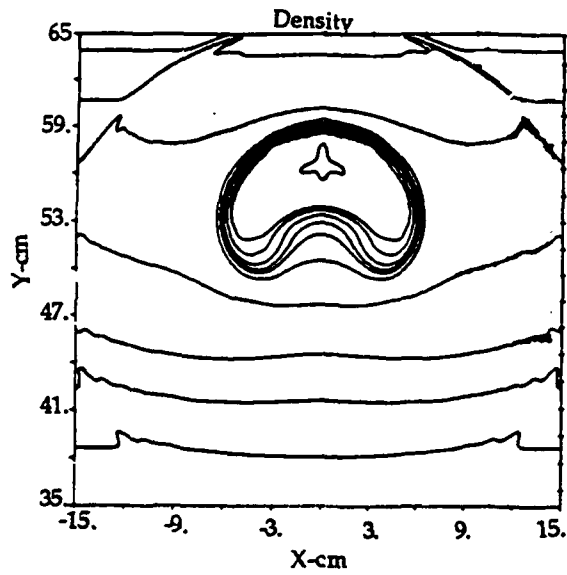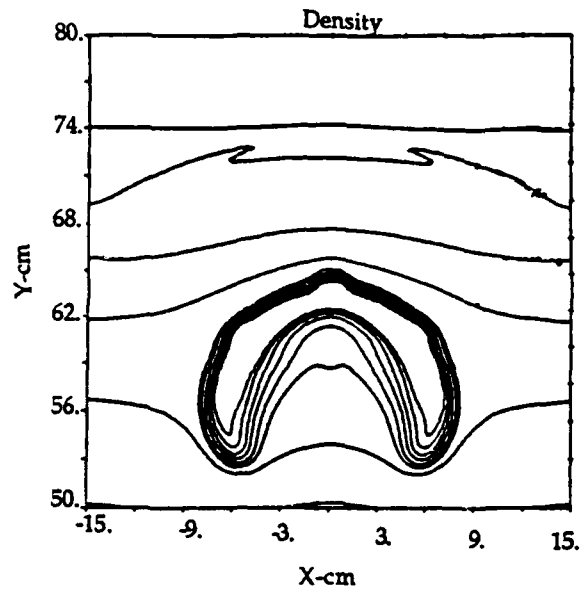
200 KT AT 50 KM

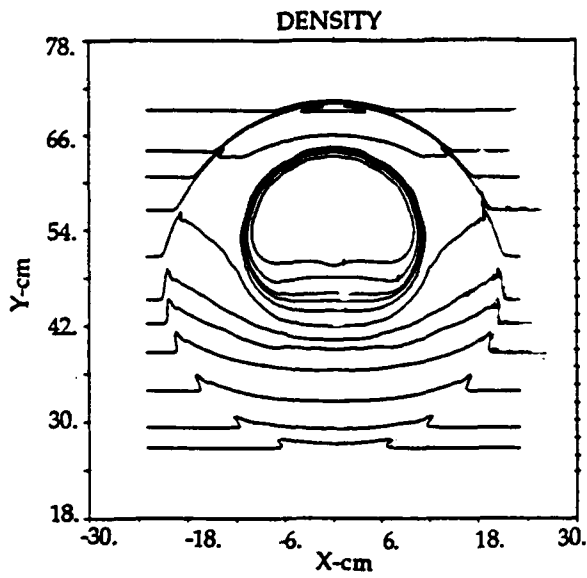Figure 9. Fireball evolution - 200 KT at 50 km.

MULTI-MT AT 45 KM
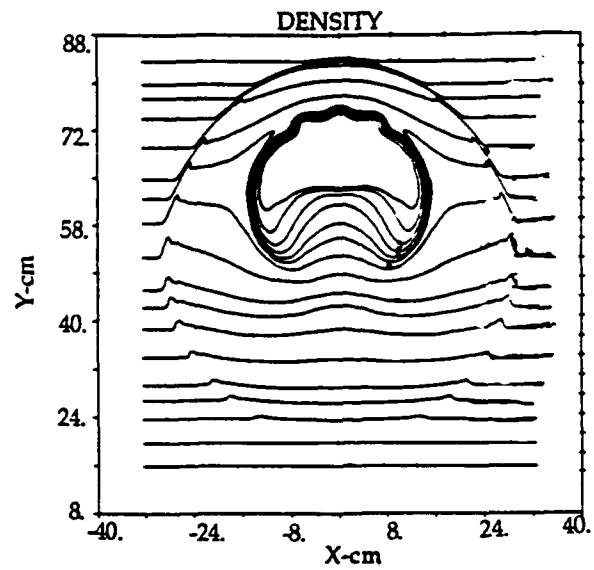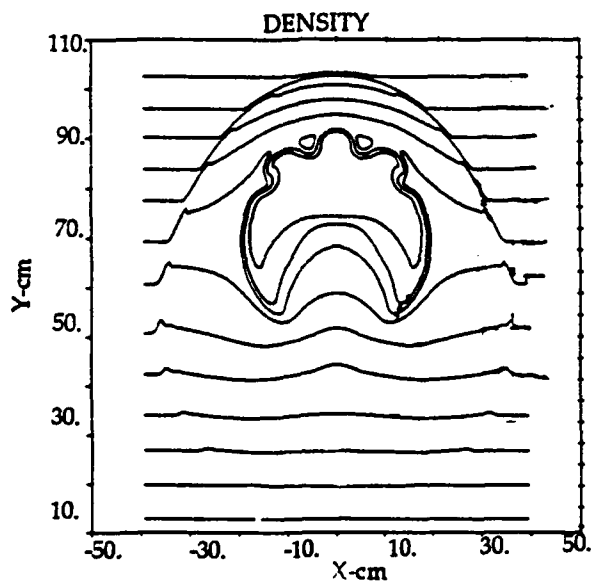
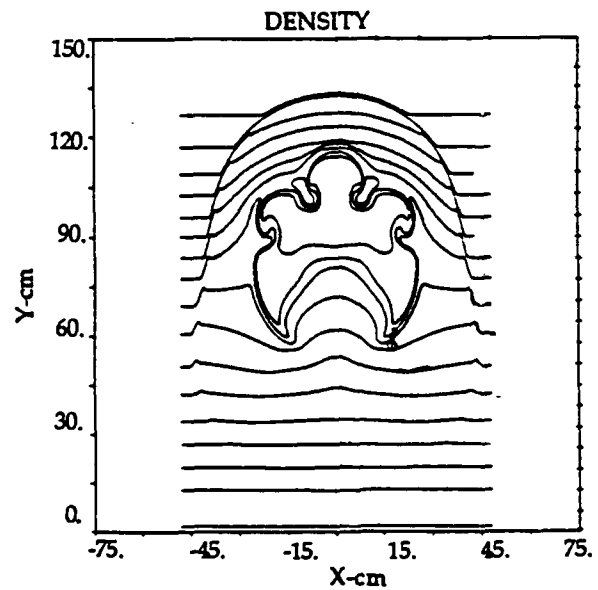Figure 10. Fireball evolution - multi-MT at 45 km.

1 MT AT 60 KM

TEMPERATURE

T = 30 s

TEMPERATURE

T = 60 S

TEMPERATURE

T = 90 S

TEMPERATURE
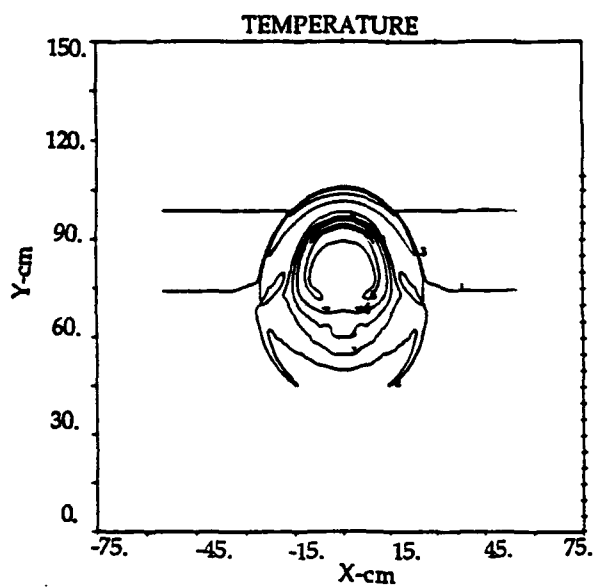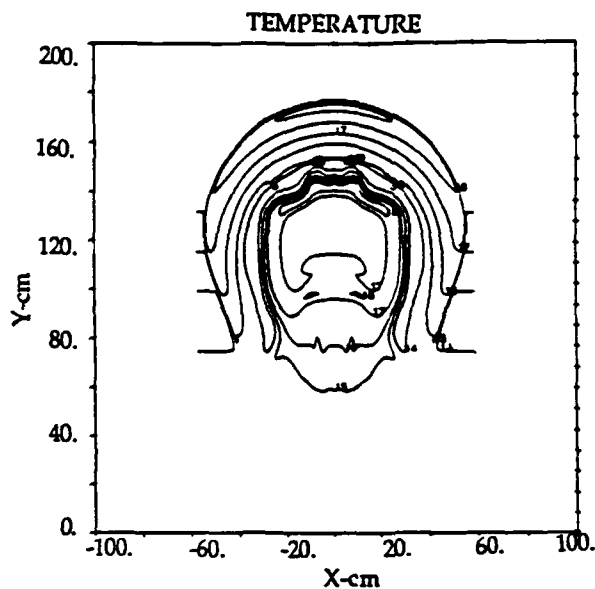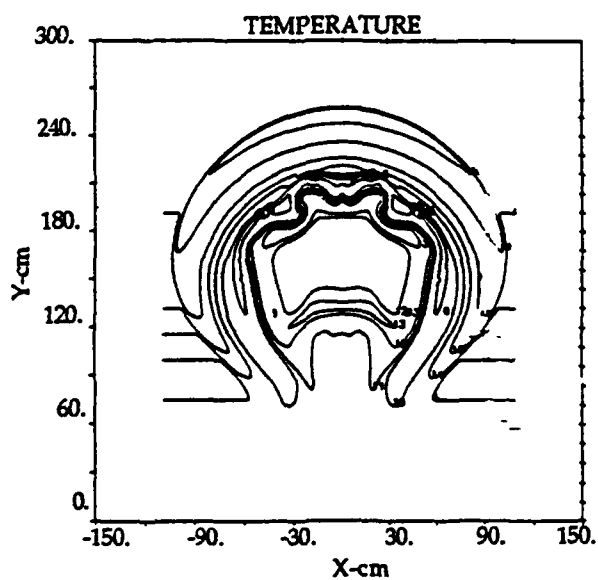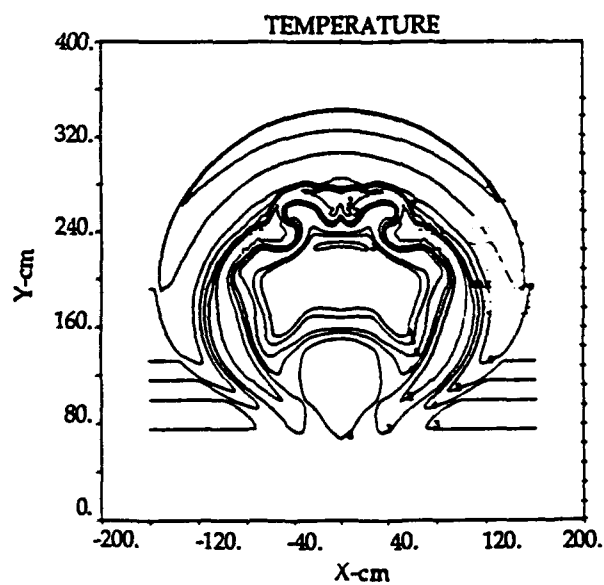
T = 120 S

Figure 11. Fireball evolution - 1 MT at 60 km.

24

situations. Higher order differencing steepens the gradients near the fireball edge which in turn favors the growth of instabilities at larger wave numbers than possible in first order calculations. Wavelengths long with respect to the thickness of the gradient region see it as a discontinuity and respond with growth at a large fraction of the inviscid rate. Wavelengths that are small with respect to the gradient region grow correspondingly slower or are stable, depending on their size. Further work is needed to prove this premise but, on the surface it seems consistent with published theory (McCartor, et al., 1973) and our own numerical experiments.

Our original chemistry implementation in the second order code used an algorithm that moved total mass in second order and constituent masses in first order. Because chemical energy moves with the mass, this algorithm is diffusive in both mass and energy. Figures 12 and 13 compare energy and density contours at 90 seconds from equation-of-state and non-equilibrium calculations of 200 KT and 50 km. Results from the non-equilibrium calculation are noticeably more diffuse and the secondary thermal at the fireball top is much less developed. We attribute the differences to the diffusion in the advection algorithm employed in the chemistry calculation. This suggests that, since diffusion has such a large effect, physically real diffusive process like radiation and turbulence should be included in fireball calculations.

Current calculations of fully ballistic fireballs are exhibiting instabilities unlike those seen in other calculations. The features described in the preceding paragraphs formed in regions where a light gas was pushing a heavier gas; the classic Rayleigh-Taylor unstable situation. In the ballistic calculations, no such region forms. However, instabilities do develop in the heaved region. At first, we suspected that responsibility lay with the unrealistic chemical rate processes related to the constituent diffusion noted above. We addressed this by developing a new algorithm that transported the constituents, in addition to the total mass, in a second order manner. The new advection algorithm had little effect on the development of the instabilities.

Figure 14 compares density contours at 60 seconds from first order and second order material transport calculations of multi-MT at 80 km. The new advection algorithm was used in the second order calculation. Structures in the higher order calculation are clearly visible at the later time. Dr. Bill Shih of PRI suggested at the 1989 AESOP meeting in Santa Barbara that instabilities could develop in the heaved region of intermediate altitude fireballs. Dr. Shih compared the flow in the heaved region to jet flows with an inflection
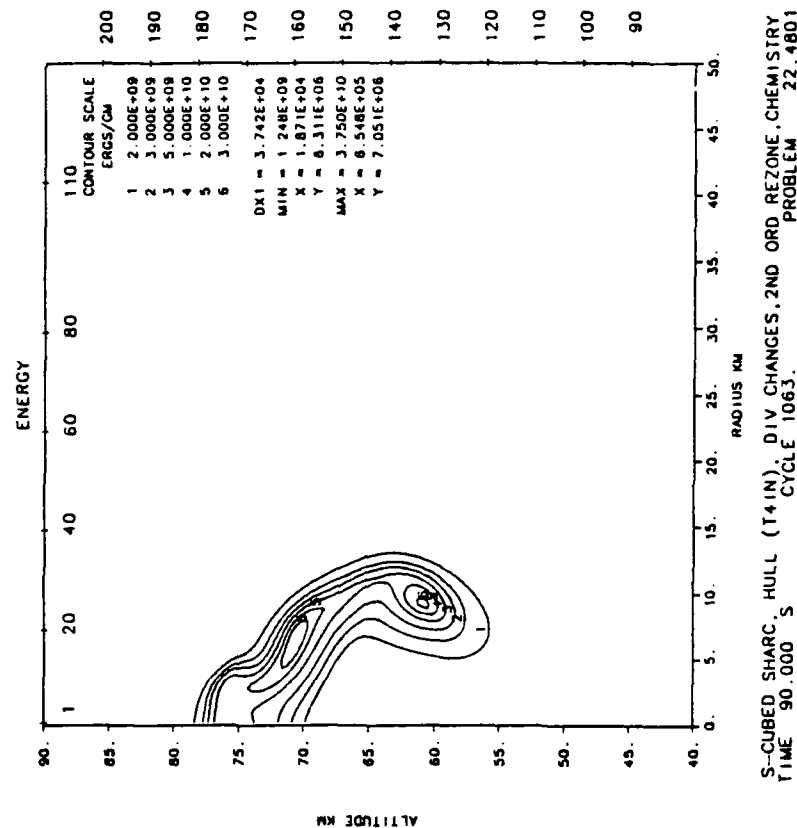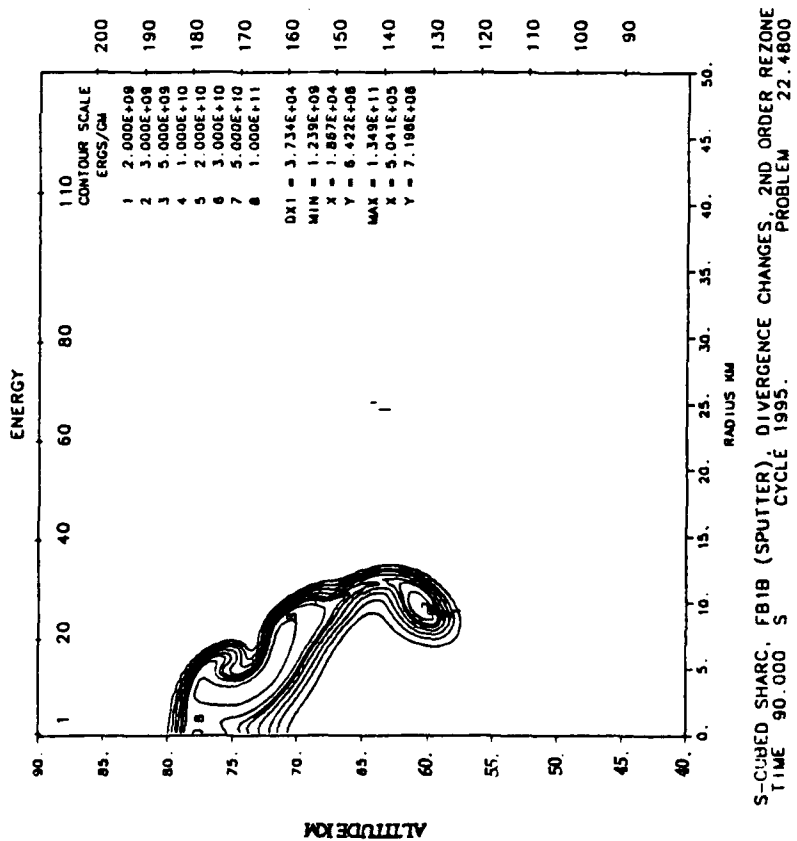
25

Figure 12. Energy contours at 90 seconds - 200 KT at 50 km - equation-of-state versus non-equilibrium chemistry.
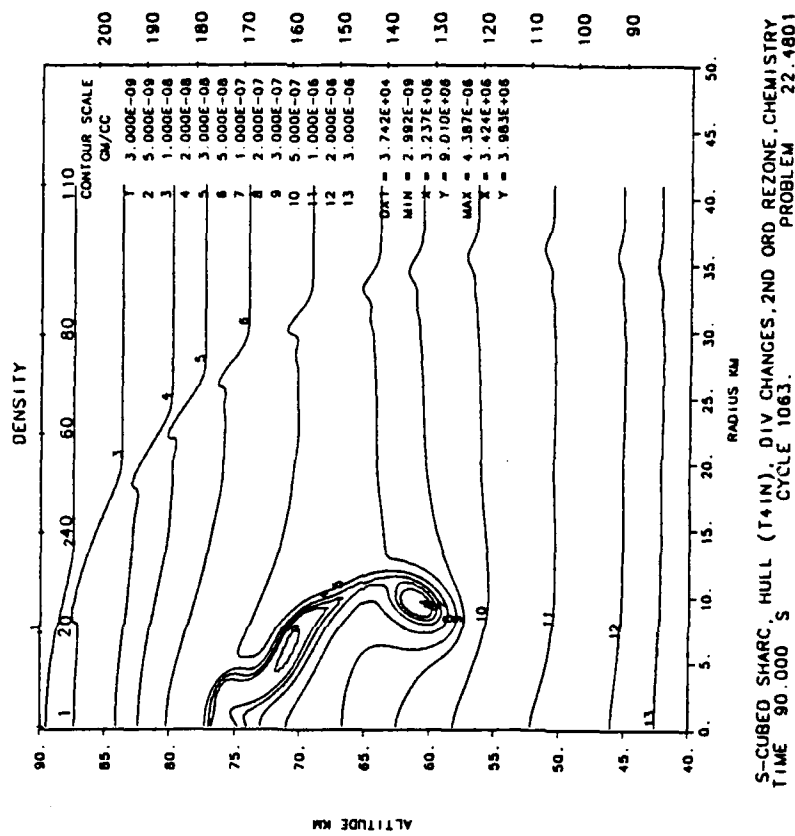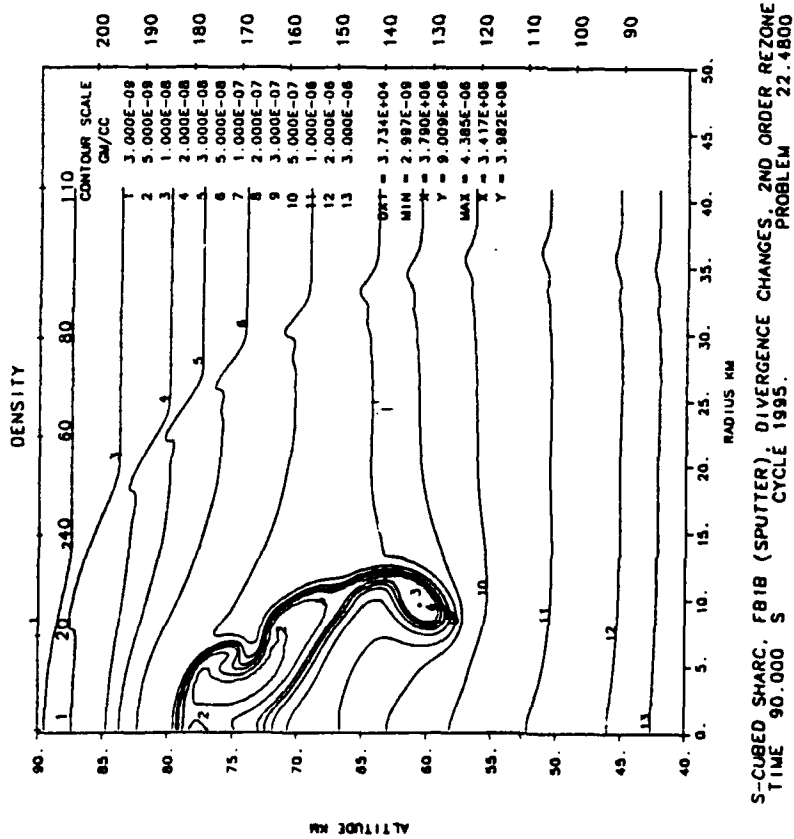
Figure 13. Density contours at 90 seconds - 200 KT at 50 km - equation of state versus non-equilibrium chemistry.
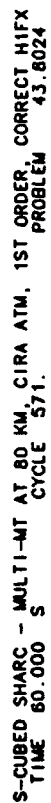
Figure 14. Density contours at 60 seconds, multi-MT at 80 km, first-order versus second-order

point in the velocity profiles. Such flows are known to be unstable (Yih, 1977). Further research would be necessary to definitively make this connection. Another possible source of instability for these flows is what Book (1984) calls a convective instability. It develops when the derivative of the entropy in the direction of motion is less than zero. It is possible that such situations could arise in flows which involve complex chemical rate processes. It is pertinent to note that there is no unambiguous evidence for instabilities in ballistic fireballs.

So far in our discussions, we have ignored the real geometry of the problem. It is assured that real fireball instabilities are three dimensional. They are subject to wind shears, asymmetric disassembly effects, and three dimensional random perturbations. Two dimensional axisymmetric calculations do not account for variations in the azimuthal direction and real dynamical effects such as vortex stretching. Consequently, questions arise as to whether results from two dimensional calculations are realistic. A non-linear analysis of the Rayleigh-Taylor instability by Jacobs and Catton (1988) indicates that "axisymmetric instabilities grow faster than other shapes in their respective geometries". This suggests that current calculations, which force axisymmetry, might overestimate the size of the structured region, and thus influence researchers to overstate its importance.

Further questions come to mind concerning the ability of a finite-difference code to represent response realistically at all wave numbers. Our numerical experiments in Section 2 indicate significant damping at wavelengths not resolved over many zones. At best, therefore, the high wave-number cutoff is governed by the zoning, as in first order calculations. Concomitant effects on the energy cascade from large to small scales are uncertain, but to prevent aliasing, a subscale turbulence model is considered necessary for high resolution calculations.

SECTION 4
FIREBALL TURBULENCE MODELING

The SHARC turbulence model is based on the well known K-ε model, (Launder and Spalding, 1972), which employs transport equations for the turbulent kinetic energy K and its dissipation rate ε. The specifics of the version used in SHARC are described in the reports by Barthel (1985) and Pierce (1986).

Two formulations of the turbulence model have been incorporated and tested in the SHARC code. They differ in the calculation of the turbulent eddy viscosity ($V_T = C_\mu k^2/\varepsilon$). In the first, which follows the derivation of Launder and Spalding (1972), C_μ is a constant with a value of 0.09. In the second (Rodi, 1976, and Lakshminarayana, 1986), C_μ is a variable that depends on the ratio of local production of turbulence to its dissipation. The second formulation, called an algebraic Reynolds stress model, reduces to the first for equilibrium turbulence; i.e. production equals dissipation. Both models have been validated against incompressible jet flows, and the variable C_μ formulation has been successfully employed in calculations of precursed airblast. To date, however, results from applying these models to fireballs have been inconclusive.

Both formulations of the model have been applied to calculations of buoyant (200 KT at 50 km) and transition (multi-MT at 45 km) fireballs. A strong sensitivity to initial values of K and ε was found in calculations which employed the constant C_μ formulation. If the time scale for dissipation (K/ε) was too large, unrealistically high turbulent energies were generated very rapidly and the calculation ceased with energy errors. For small K/ε, no turbulence was generated. Three variable C_μ calculations, which had initial turbulence energy to dissipation rate ratios (K_0/ε_0) of $10^5/1$, $10^5/900$, and $10^7/10^7$, were completed for 200 KT at 50 km. These, for reasons discussed in subsequent paragraphs, failed to generate sufficient turbulent energy to influence the fireball evolution noticeably.

The variable C_μ model is coded with limiters that prevent K and ε from falling below their initial values. In calculations where K_0/ε_0 was $10^7/10^7$, limiters kept both K and ε at their initial values and C_μ remained near the equilibrium value of 0.09. The net result was a near-constant turbulent eddy viscosity of approximately 10^6. This appears to be an extremely high value until comparison is made with data such as that presented in Figure 15 (Reaction Rate Handbook, 1979), which shows the range of V_T as a function of

30

Effective Atmospheric Diffusion Coefficient D as a Function of Altitude. From: DNA 1948H, Reaction Rate Handbook, Page 3-30.
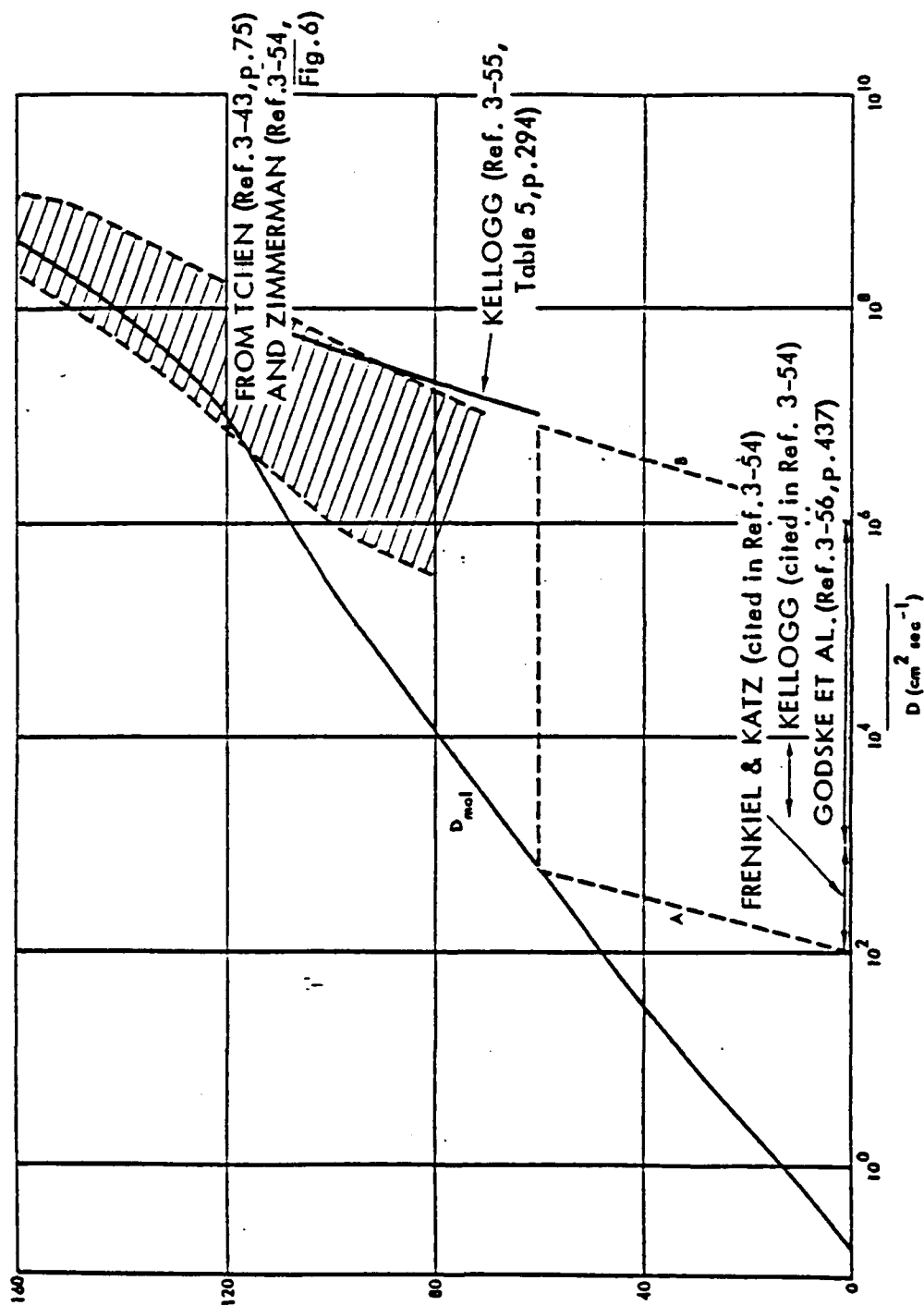

Figure 15. Effective atmospheric diffusion coefficient as a function of altitude.

altitude in the ambient atmosphere. The value of 10^6 falls well within the range of data at 50^7 km.

Calculations of 200 KT at 50 km and multi-MT at 45 km were run with an approximately constant V_T of 10^6. Figures 16 and 17 compare the 90-second density contours with their inviscid counterparts. Discernible but insignificant effects are evident. Comparison with Figure 3 indicates that the numerical errors noted for the advection of multi-component flows has a larger effect than the 10^6 viscosity.

The SHARC turbulence model accounts for turbulence generation due to the interaction of the density and pressure fields through the term

$$G = C_{RT} \frac{V_T}{\rho} \nabla P \cdot \nabla \rho \tag{7}$$

where P is pressure, ρ is density, and V_T is the turbulent kinematic (eddy) viscosity. C_{RT} is a constant (Barthel, 1985), that until recently was assigned the value of 4/3. Recent experience (Pierce, 1989) suggests a smaller value might be more appropriate. We often refer to Equation 7 as the Rayleigh-Taylor production term, although "enthalpic production" (Issa, 1980) might be more generally applied.

The variable V_T is a function of the local turbulent kinetic energy K and dissipation rate e through the relation $V_T = C_\mu k^2/\mu$. In the algebraic Reynolds stress model, C_μ is proportional to the local production-dissipation ratio; C_μ is zero for very low and high values of the ratio and peaks at the equilibrium value of 0.09 for ratios near 1. In the calculations described in the preceding paragraphs, the Rayleigh-Taylor production was included in the calculation of C_μ. Consequently, turbulence production in regions where the Rayleigh-Taylor term was large was artificially limited.

Pierce (1989) has suggested that the variable C_μ be used only in connection with the calculation of shear stresses and that it be constant in the calculation of the Rayleigh-Taylor term. We have not yet applied this approach to intermediate altitude fireballs because of time constraints and uncertainties in the proper value for C_{RT}. An effort involving calibration of C_{RT} remains to be completed. The first step is to find a well documented experiment that can be used as a test calculation.
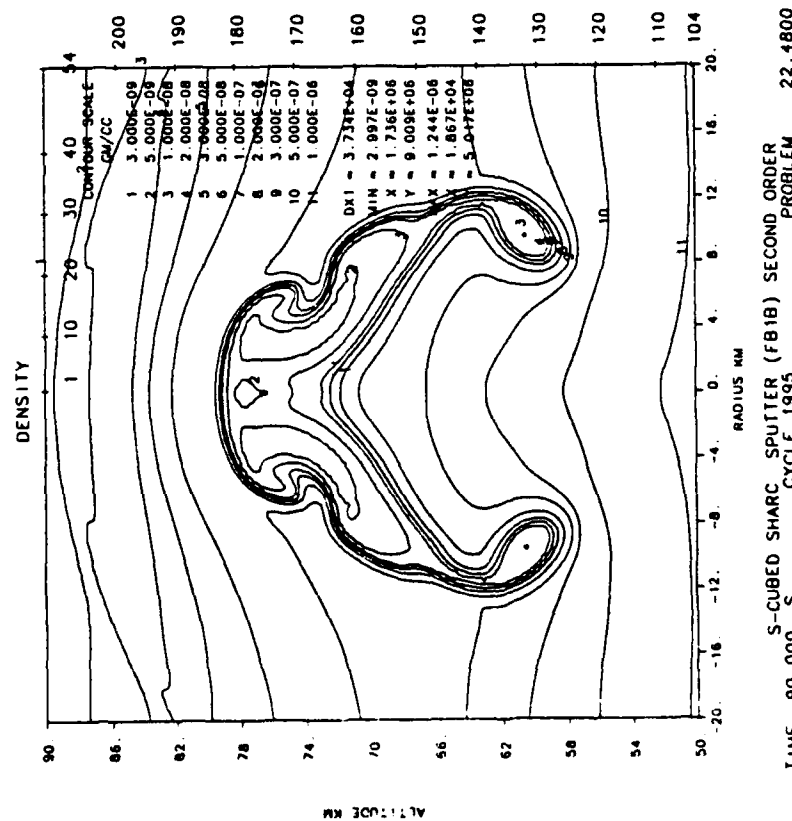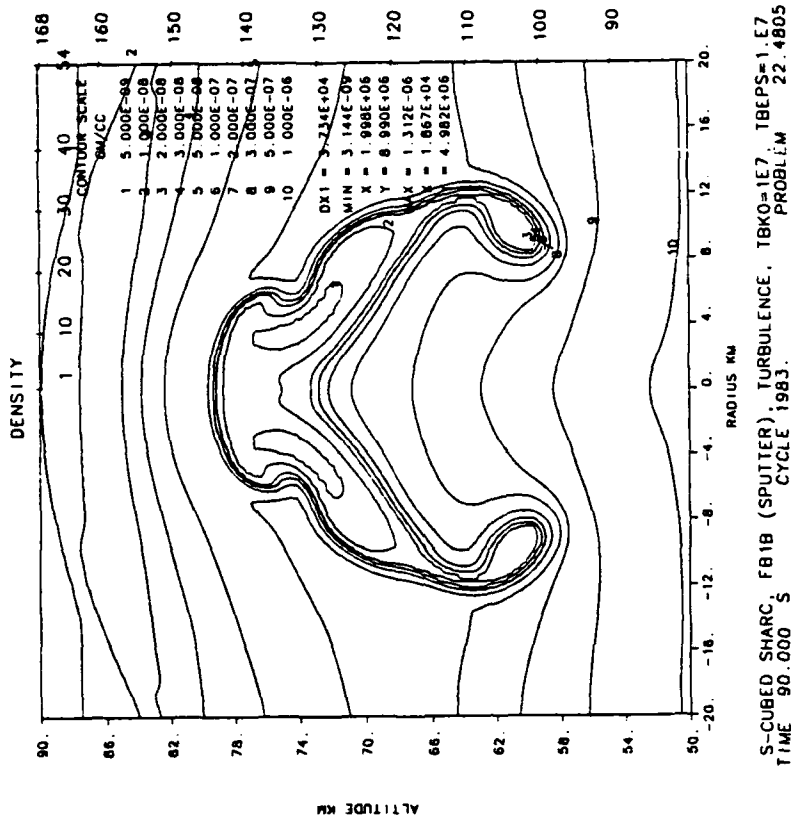
Figure 16. Density contours at 90 seconds, 200 KT at 50 km, inviscid versus turbulent, VT~106.
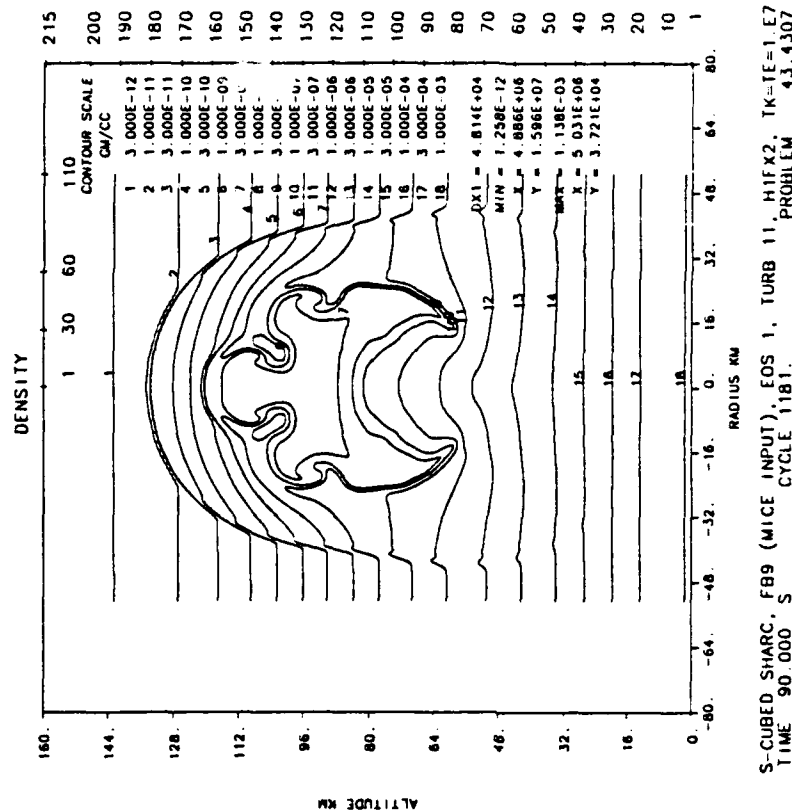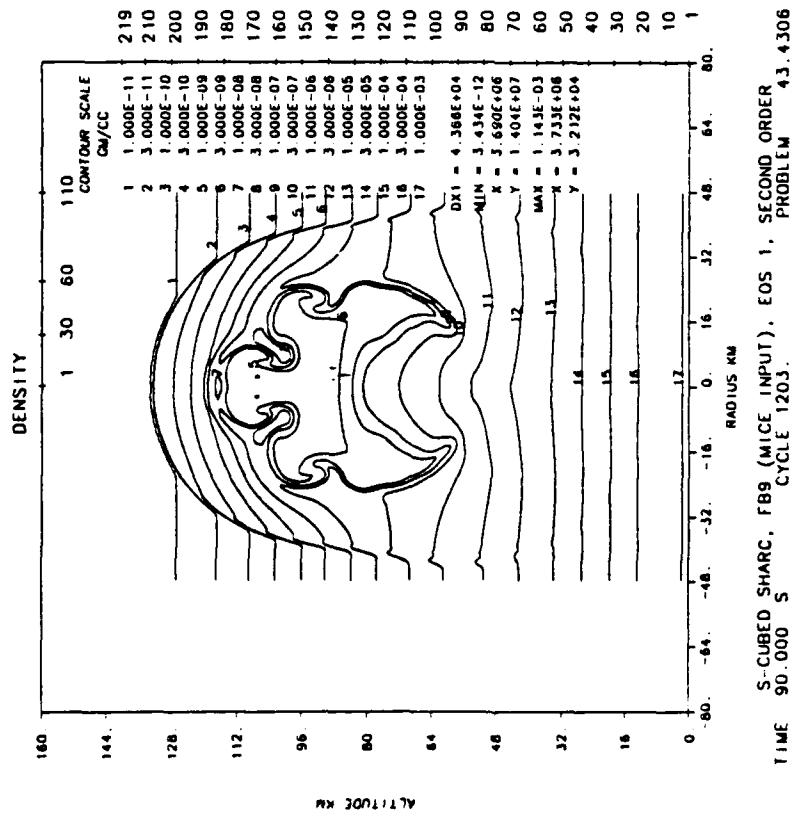
Figure 17. Density contours at 90 seconds, multi-MT at 45 km, inviscid versus turbulent, VT~106.

An alternate, and perhaps more general, approach would be to derive, in a manner analogous to that used for the shear terms, algebraic stress equations for the Rayleigh-Taylor terms. This approach has been applied with considerable success by Freeman (1987) in a one-dimensional model. Implementation of this approach in SHARC would require considerable work, due to differences in formulation and application between SHARC and the one-dimensional model.

:-

SECTION 5
SUMMARY AND CONCLUSIONS

A series of numerical experiments of the Rayleigh-Taylor instability were completed with the CLOUD code. The calculations were inviscid and involved driving disturbances that were nominally of a single frequency. Results indicate that numerical viscosity provides a major influence on the evolution of the instability and that the numerical viscosity is decidedly zoning dependent. Diffusive effects are clearly evident in the least resolved calculations. In addition, continued doubling of the resolution did not lead to the convergence that is usually experienced with first order codes. Zoning dependent differences in the dispersive and dissipative characteristic of the advection algorithm contributed to these results, which were exacerbated by the introduction of higher than desired frequency components at initialization. The latter were a direct result of attempting to initialize a sinusoid on a rectangular grid.

Anomalous results were experienced at both the low and high wave number limits imposed by the grid. Low wave number disturbances experienced the greatest viscosities. Consequently, the inviscid growth rates predicted by theory at "small" wave numbers could not be attained. Finite zoning provided an upper limit on the wave numbers that could be resolved, let alone transported. Aliasing effects were evident in calculations of "high" frequency disturbances.

A comparable set of calculations of the Richtmyer-Meshkov instability were completed with the SHARC code. Growth rate effects were observed that were qualitatively similar to those noted for the CLOUD calculations.

Taken in aggregate, the numerical experiments and our fireball results emphasize the important influence of zoning and numerics on hydrodynamic calculational results. Most importantly, they suggest that brute force attempts at high resolution calculations which involve a large number of fine zones, without consideration of physically real diffusive processes such as turbulence and radiation, will likely lead to erroneous results. Real processes which take place on spatial scales of the order of the mesh size must be either explicitly included or parameterized in hydrodynamic calculations. In addition, more work is warranted to further define the effects of the energy cascade truncation which results from the high wave number cutoff imposed by the grid. The latter comment also applies to azimuthal wave number limitations imposed by axisymmetric calculations.

Two turbulence models, which vary in the calculation of the turbulent eddy viscosity, have been implemented in SHARC and have been applied to fireball calculations. Results were inconclusive. Shortcomings in the models have been identified and work is continuing in these areas.

SECTION 6
LIST OF REFERENCES

Baker, M. B. , Breidenthal, R. E., Choularton, T. W., and Latham, J., "The Effects of Turbulent Mixing in Clouds," *Journal of the Atmospheric Sciences*, Vol. 41 No. 2, 1984.

Book, D. L., "Rayleigh-Taylor Instability in Compressible Media," Laboratory for Computational Physics, Naval Research Laboratory, Memorandum Report 5373, August 1984.

Broadwell, J. E. and Breidenthal, R. E., "A Simple Model of Mixing and Chemical Reaction in a Turbulent Shear Layer," *J. Fluid Mech.*, Vol. 125, pp. 397-410, 1982.

Brown, G. L. and Roshko, A., "On Density Effects and Large Structure in Turbulent Mixing Layers," *J. Fluid Mech*, Vol. 64, Part 4, pp. 775-816, 1974.

Carpenter, R. L., Jr., Droegemeier, K. K., Woodward, P. R., and Hane, C. E., "Application of the Piecewise Parabolic Method (PPM) to Meteorological Modeling," Monthly Weather Review, Vol. 118 No. 3, 1990.

Chandrasekhar, S., "Hydrodynamic and Hydromagnetic Stability," Dover 1981 (Orig. 1961 Oxford).

DNA Reaction Rate Handbook, Defense Nuclear Agency Report DNA 1948-H, Rev. 8, April 1979.

Duff, R. E., Harlow, F. H., and Hirt, C. W., "Effects of Diffusion on Interface Instability between Gases," *The Physics of Fluids*, Vol. 5, No. 4, 1962.

Fox, D. G., "Numerical Simulation of Three-Dimensional, Shape-Preserving Convective Elements," *Journal of the Atmospheric Sciences*, Vol. 29, pp 322-341, 1972.

Freeman, B. E., "A Turbulence Model Incorporating Transients for Thermal Layer Application," Maxwell Laboratories, S-CUBED Division SSS-TR-89-1006, October 1987.

Grabowski, W. W., "Numerical Experiments on the Dynamics of the Cloud-Environment Interface: Small Cumulus in a Shear-Free Environment," *Journal of the Atmspheric Science*, Vol. 46, No. 23, 1989.

Hunter, J. H., Jr. and Whitaker, R., W., "Anisentropic, Magnetized Kelvin-Helmholtz and Related Instabilities in the Interstellar Medium," The Astrophysical Journal, Vol. 71, No. 4, December 1989.

Issa, R. I., "Modeling of Turbulent Mixing at Density Discontinuities in Nonsteady Compressible Flows," AFWL-TR-81-105, R&D Associates, September 1981.

Jacobs, J. W. and Catton, I., "Three-Dimensional Rayleigh-Taylor Instability; Part 1. Weakly Nonlinear Theory," *J. Fluid Mech.*, Vol. 187, pp. 329-352, 1988.

Jacobs, J. W. and Catton, I., "Three-Dimensional Rayleigh-Taylor Instability; Part 2. Experiment," *J. Fluid Mech.*, Vol. 187, pp. 329-352, 1988.

Klaassen, G. P. and Clark, T. L., "Dynamics of the Cloud-Environment Interface and Entrainment in Small Cumuli: Two-Dimensional Simulations in the Absence of Ambient Shear," *Journal of the Atmospheric Science*, Vol. 42 No. 23, 1985.

Lakshminarayana, B., "Turbulence Modeling for Complex Shear Flows, *AIAA Journal*, Vol. 24 No. 12, 1986.

Launder, B. E., Reece, G. J., and Rodi, W., "Progress In the Development of a Reynolds-Stress Turbulence Closure," *J. Fluid Mec*, Vol. 68, Part 3, pp 537-566, 1975.

Launder, B. E. and Spalding, D. B., *"Mathematical Models of Turbulence,"* Academic Press, London, 1972.

Libersky, L. D., "The Calculation of Turbulence in Fireballs Using the CLOUD Hydrodynamics Code, AFTL-TR-82-129, June 1983.

McCartor, G., Messier, M. A., and Longmire, C. L., "Flow Instabilities in Rising Fireballs, "DNA 3077T, Defense Nuclear Agency, January 1973.

Richtmyer, R. D., "Taylor Instability in Shock Acceleration of Compressible Fluids," *Communications on Pure and Applied Mathematics*, Vol. XIII, pp. 297-319, 1960.

Rodi, W., "A New Algebraic Relation for Calculating the Reynolds Stresses," ZAMM 56 T219, 1976.

Rood, R. B., "Numerical Advection Algorithms and Their Role in Atmospheric Transport and Chemistry Models," *Reviews of Geophysics*, Vol. 25, No. 1, pp. 71-100, February 1987.

Sharp, D. H., "An Overview of Rayleigh-Taylor Instability," *Physica* 12D, pp. 3-18, 1984.

Sturtevant, B., "Rayleigh-Taylor Instability in Compressible Fluids," *Shock Tubes and Waves*, Proceedings of the Sixteenth International Symposium on Shock Tubes and Waves, Aachen, West Germany, July 26-31, 1987.

Tennekes, H., "Turbulent Flow in Two and Three Dimensions," American Meteorological Society, Vol 59, No. 1, 1978.

Yih, Chia-Shun, "Fluid Mechanics, A Concise Introduction to the Theory" West River Press, Ann Arbor, MI, 1988.

Youngs, D. L., "Numerical Simulation of Turbulent Mixing by Rayleigh-Taylor Instability," *Physica* 12D, pp. 32-44, 1984.

:-

APPENDIX A
RAYLEIGH-TAYLOR EXPERIMENTS AT 2-CM RESOLUTION, 2-ZONE INITIAL AMPLITUDE
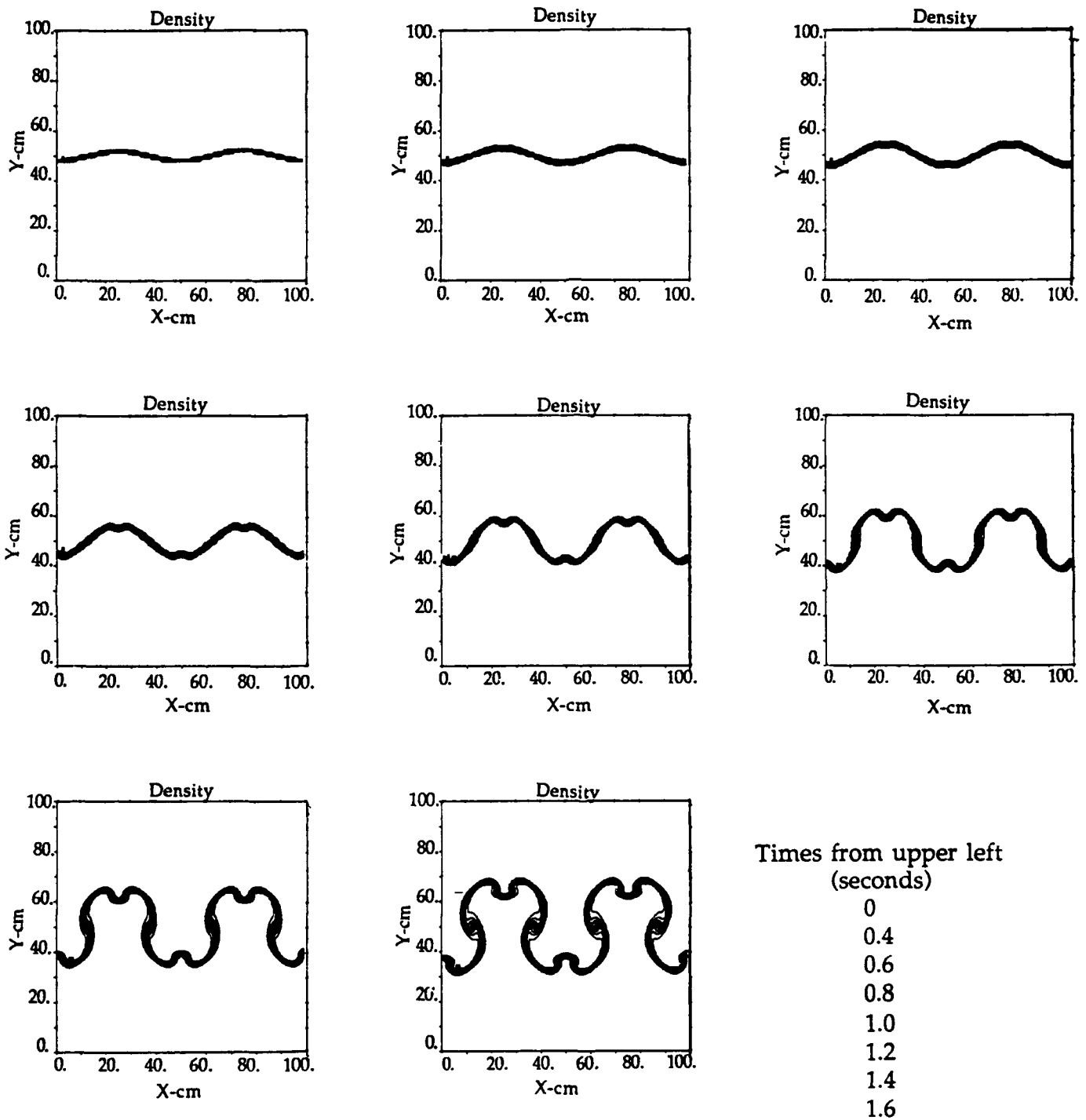
:-

Rayleigh-Taylor Experiments with CLOUD Code

Density

Density

Density

Density

Density

Density

Density

Density

Times from upper left
(seconds)

0

0.4

0.6

0.8

1.0

1.2

1.4

1.6
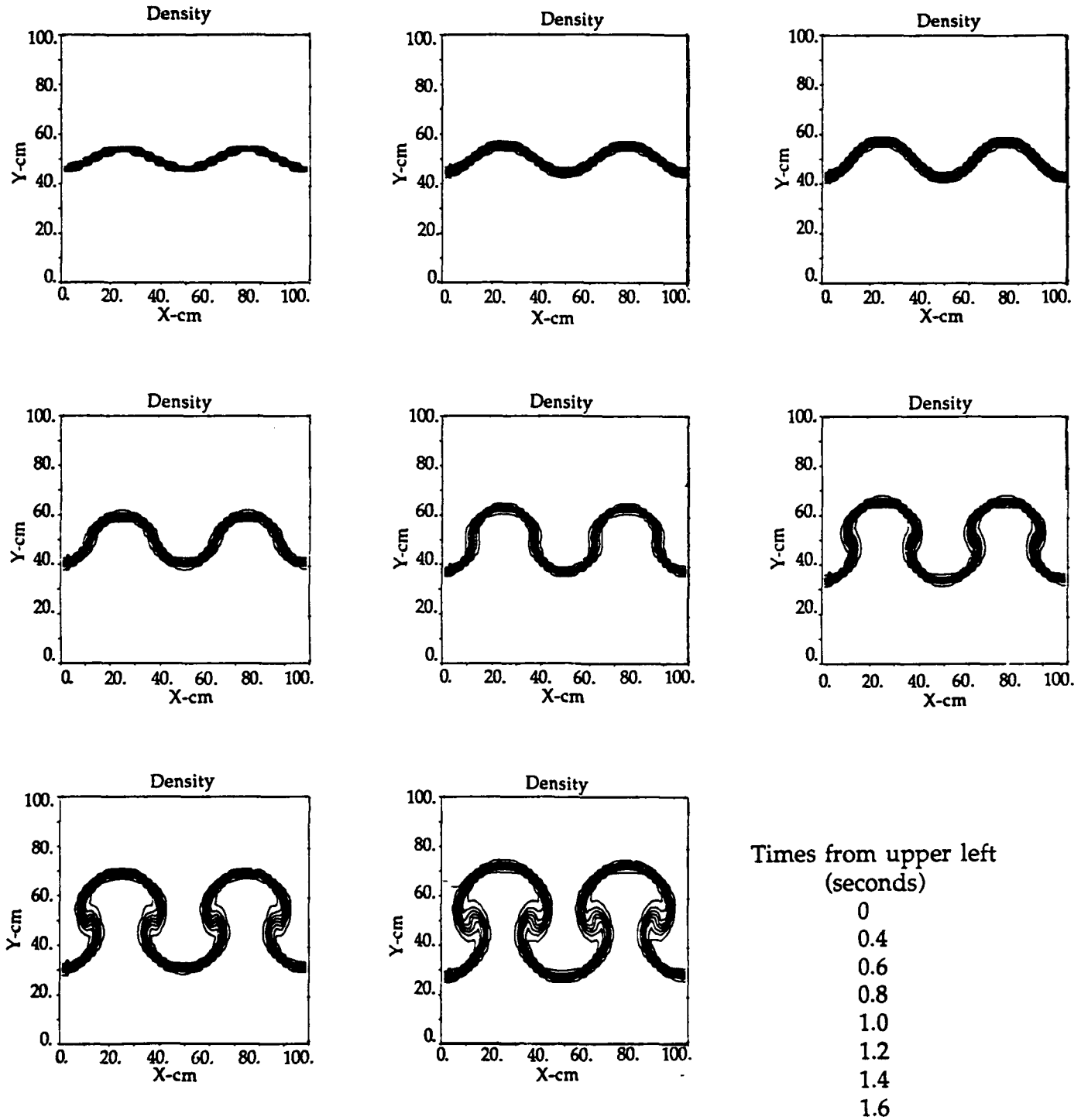
Figure 18. 2.0-cm resolution - 2-zone initial amplitude
wave number = 0-.04 •π.

Times from upper left
(seconds)

0

0.4

0.6

0.8

1.0

1.2

1.4

1.6
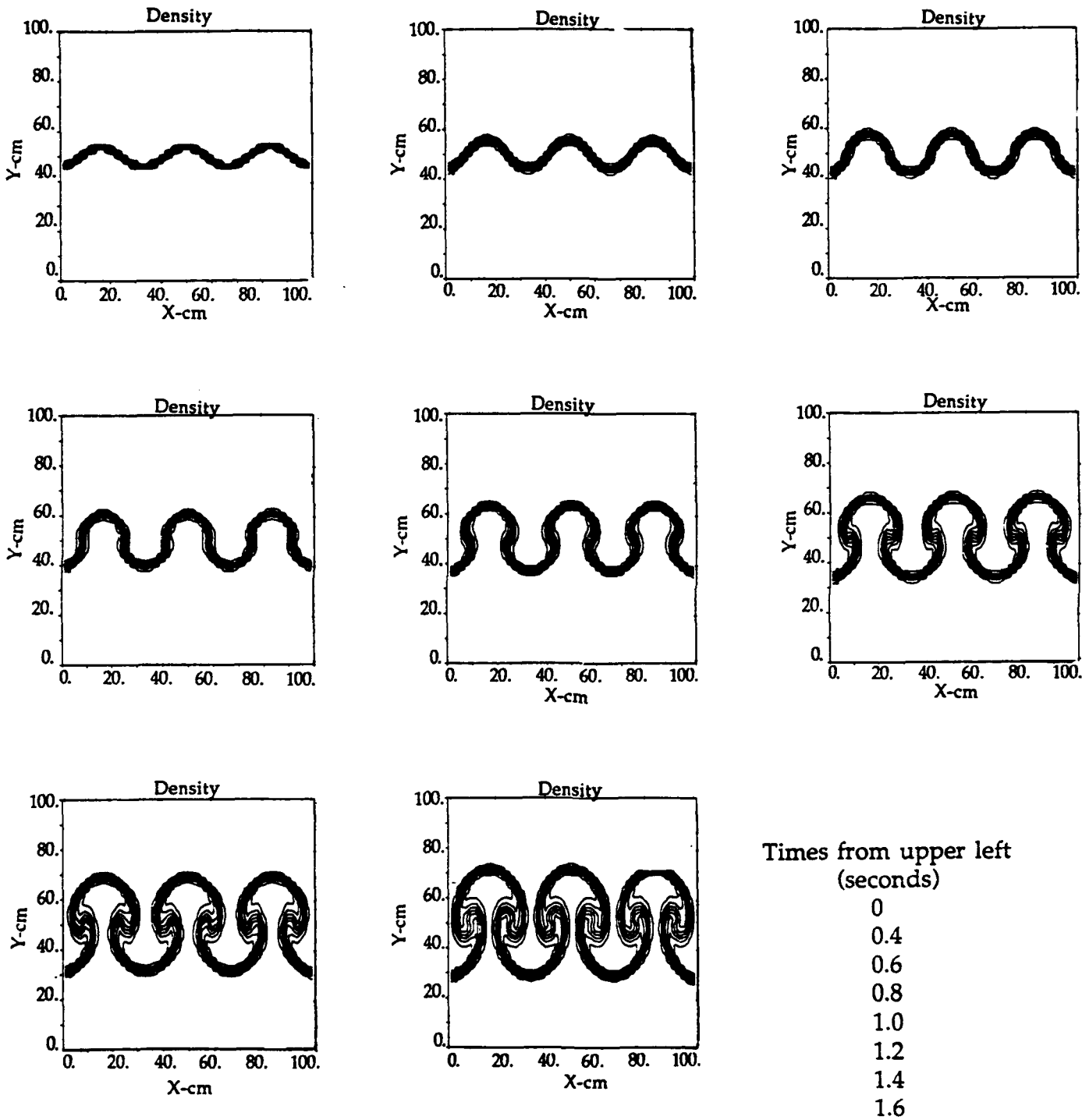
Figure 19. 2.0-cm resolution - 2-zone initial amplitude
wave number = 0.06 •π.

43

Times from upper left
(seconds)
0
0.4
0.6
0.8
1.0
1.2
1.4
1.6
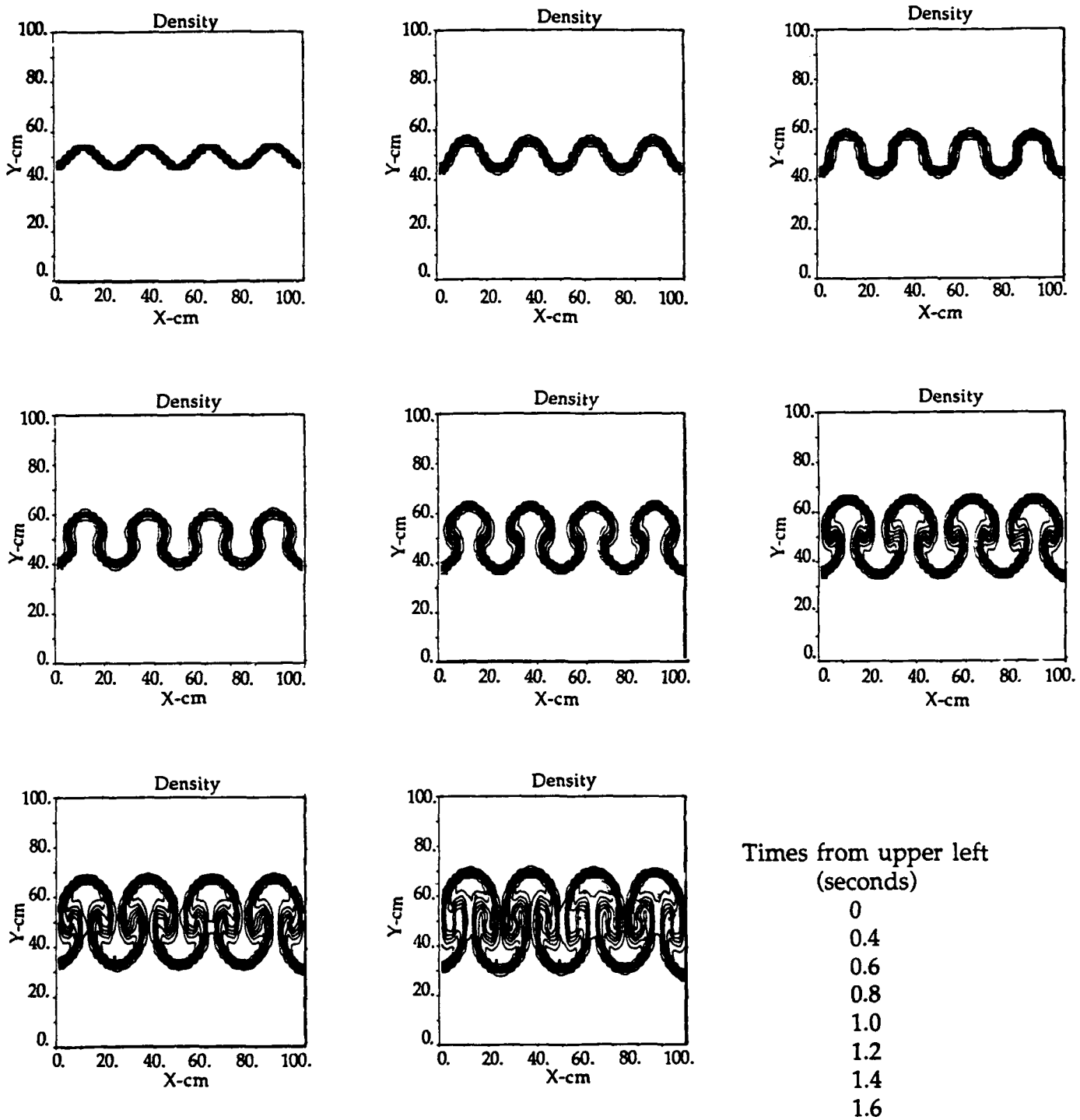
Figure 20. 2.0-cm resolution - 2-zone initial amplitude
wave number - 0.08 •π.
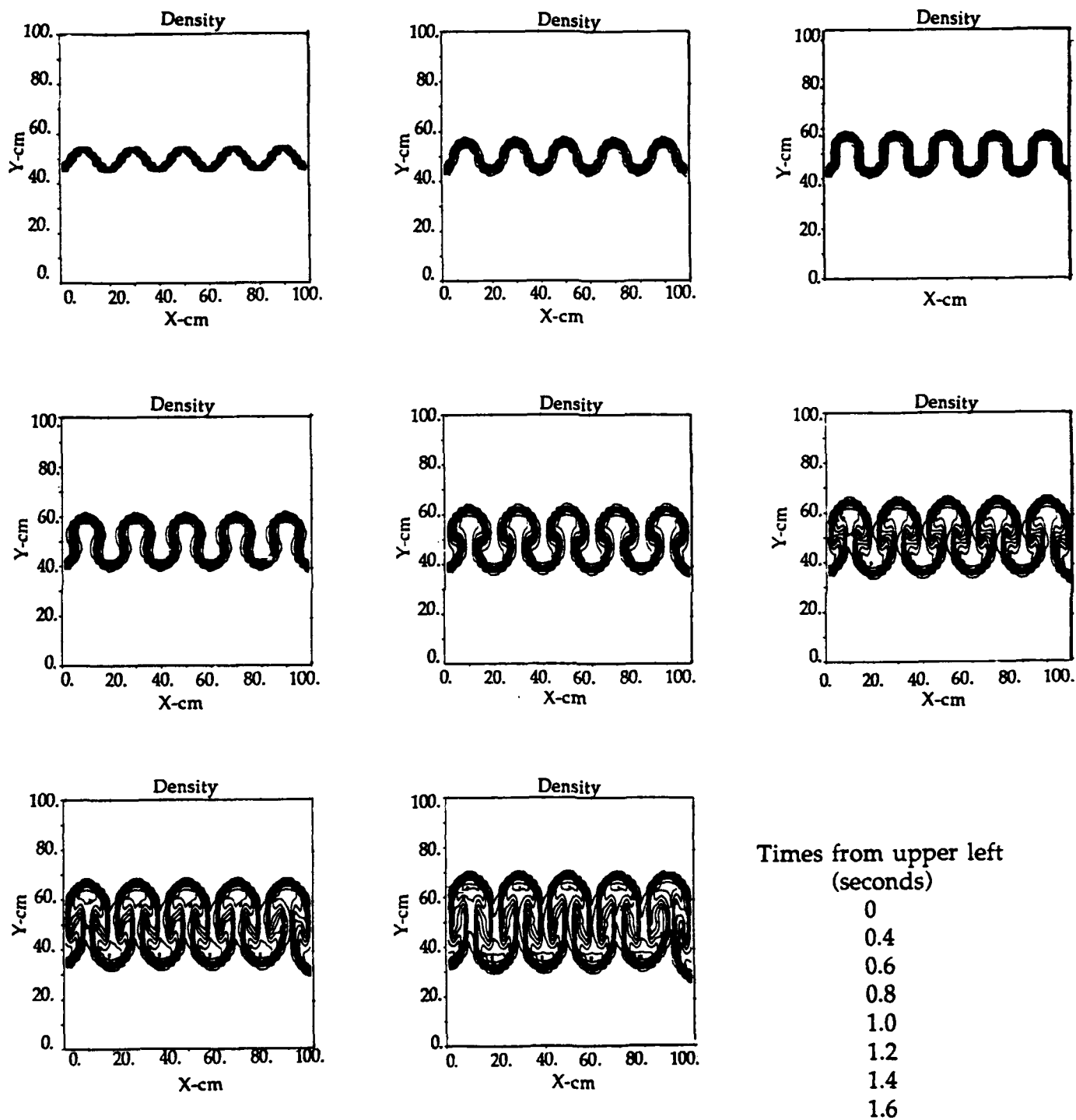
Figure 21. 2.0-cm resolution - 2-zone initial amplitude
wave number - 0.10 •π.

Times from upper left
(seconds)
0
0.4
0.6
0.8
1.0
1.2
1.4
1.6

Times from upper left
(seconds)
0
0.4
0.6
0.8
1.0
1.2
1.4
1.6
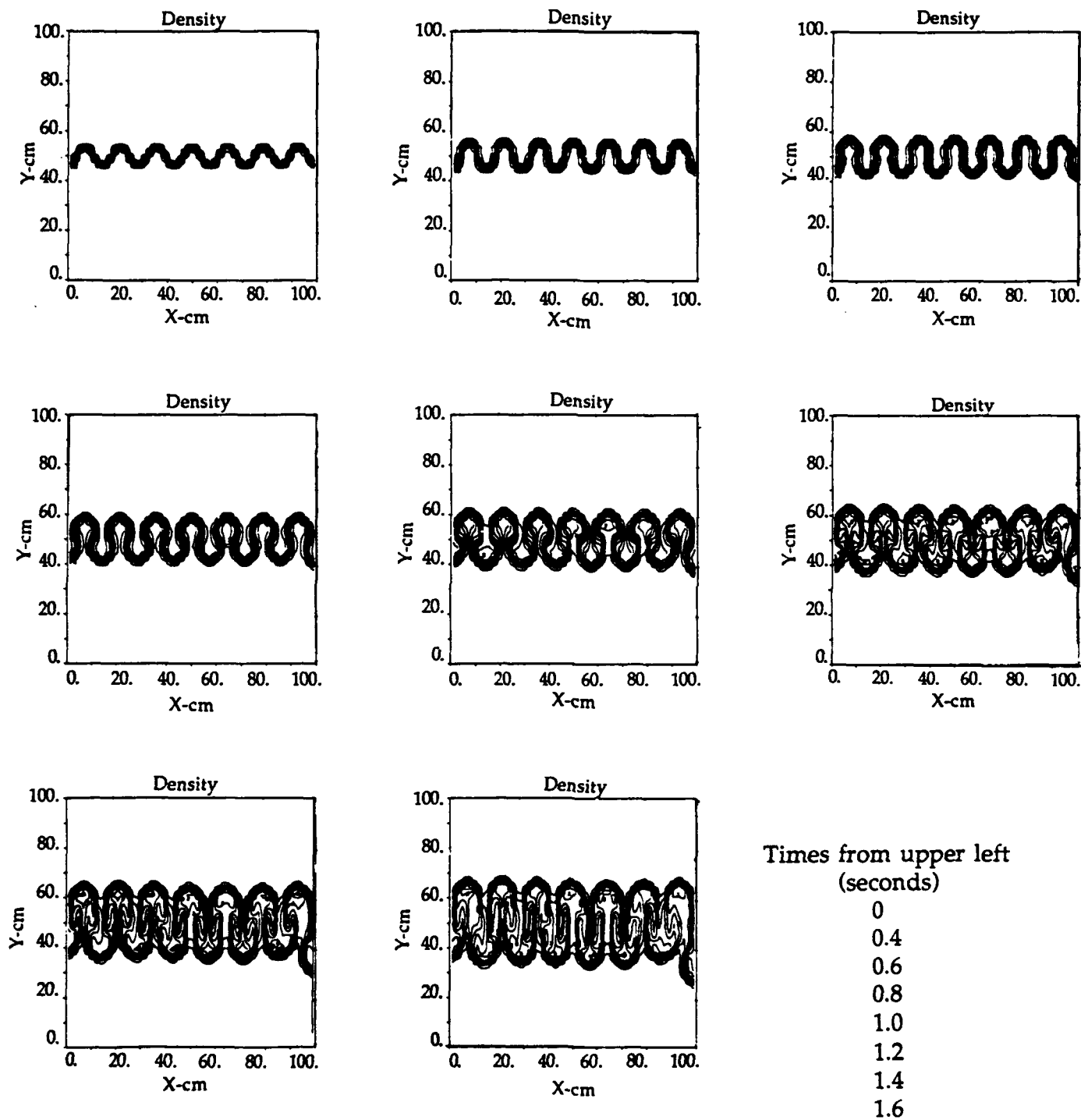
Figure 22. 2.0-cm resolution - 2-zone initial amplitude
wave number = 0.14 •π.

Times from upper left
(seconds)
0
0.4
0.6
0.8
1.0
1.2
1.4
1.6
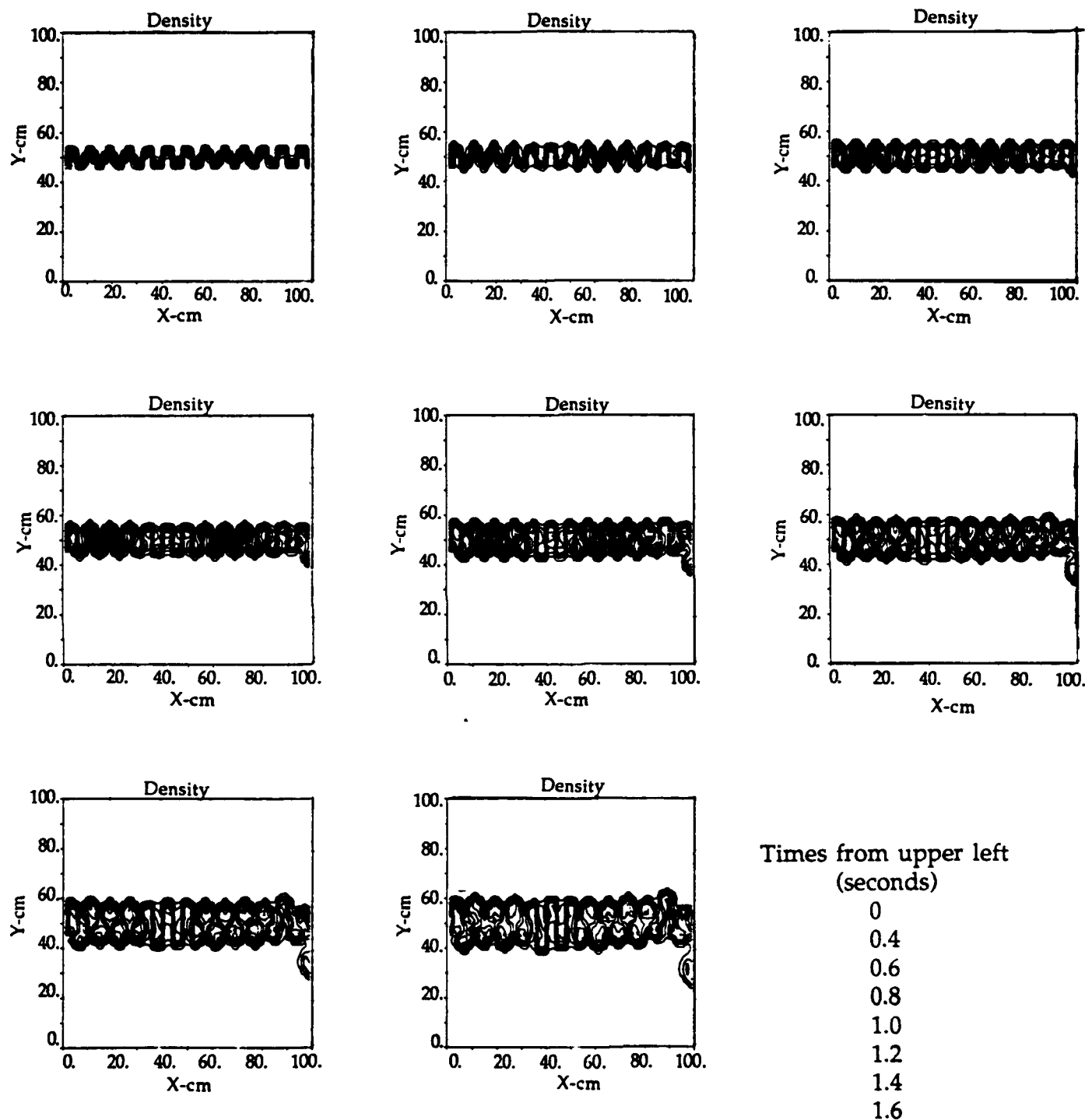
Figure 23. 2.0-cm resolution - 2-zone initial amplitude
wave number = 0.26 •π.

47

APPENDIX B
RAYLEIGH-TAYLOR EXPERIMENTS AT 1-CM RESOLUTION, 4-ZONE INITIAL AMPLITUDE

Figure 24. 1-cm resolution - 4-zone initial amplitude
wave number = 0.04 •π.
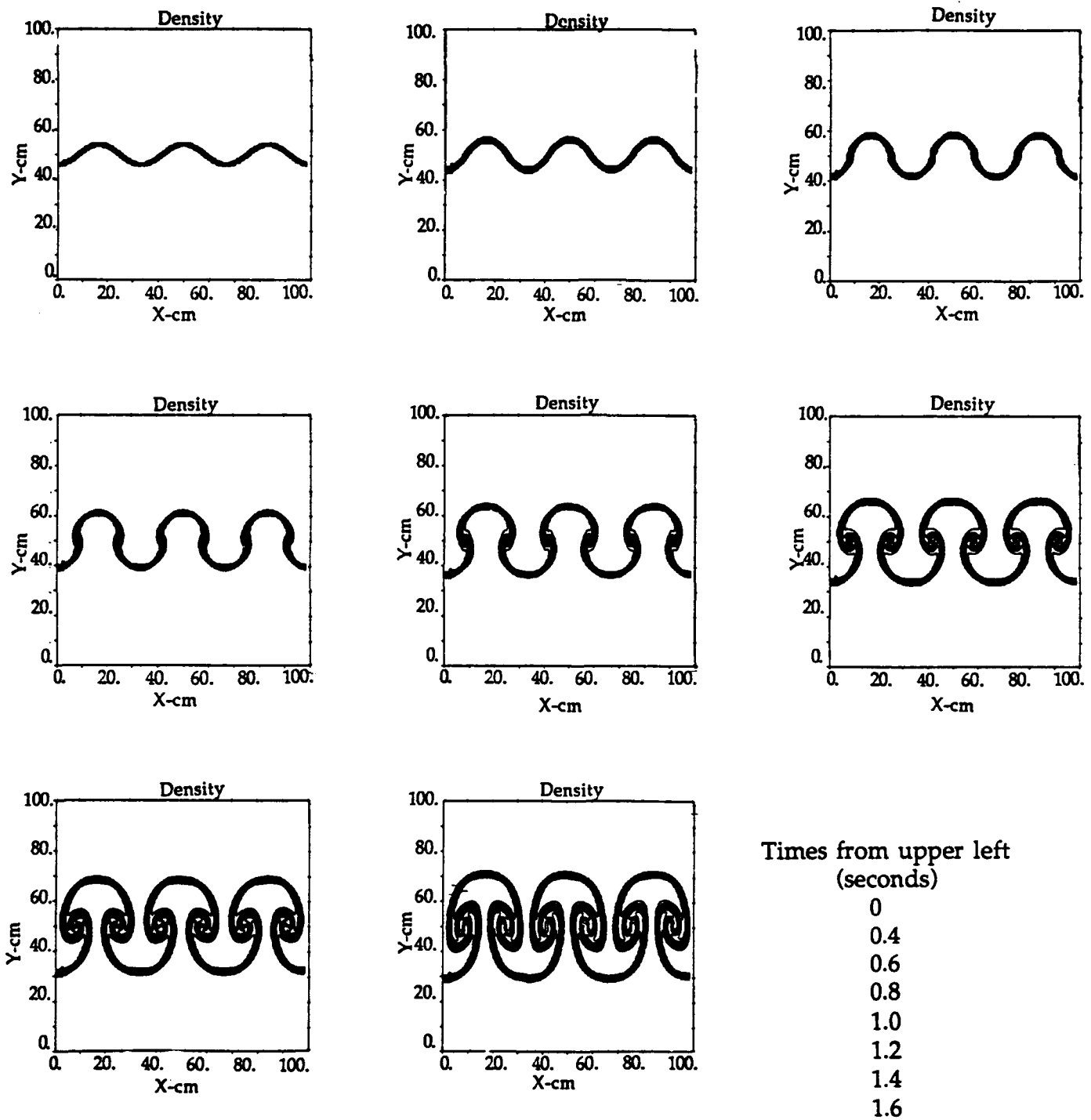
Figure 25. 1-cm resolution - 4-zone initial amplitude
wave number = 0.06 •π.

Times from upper left
(seconds)
0
0.4
0.6
0.8
1.0
1.2
1.4
1.6
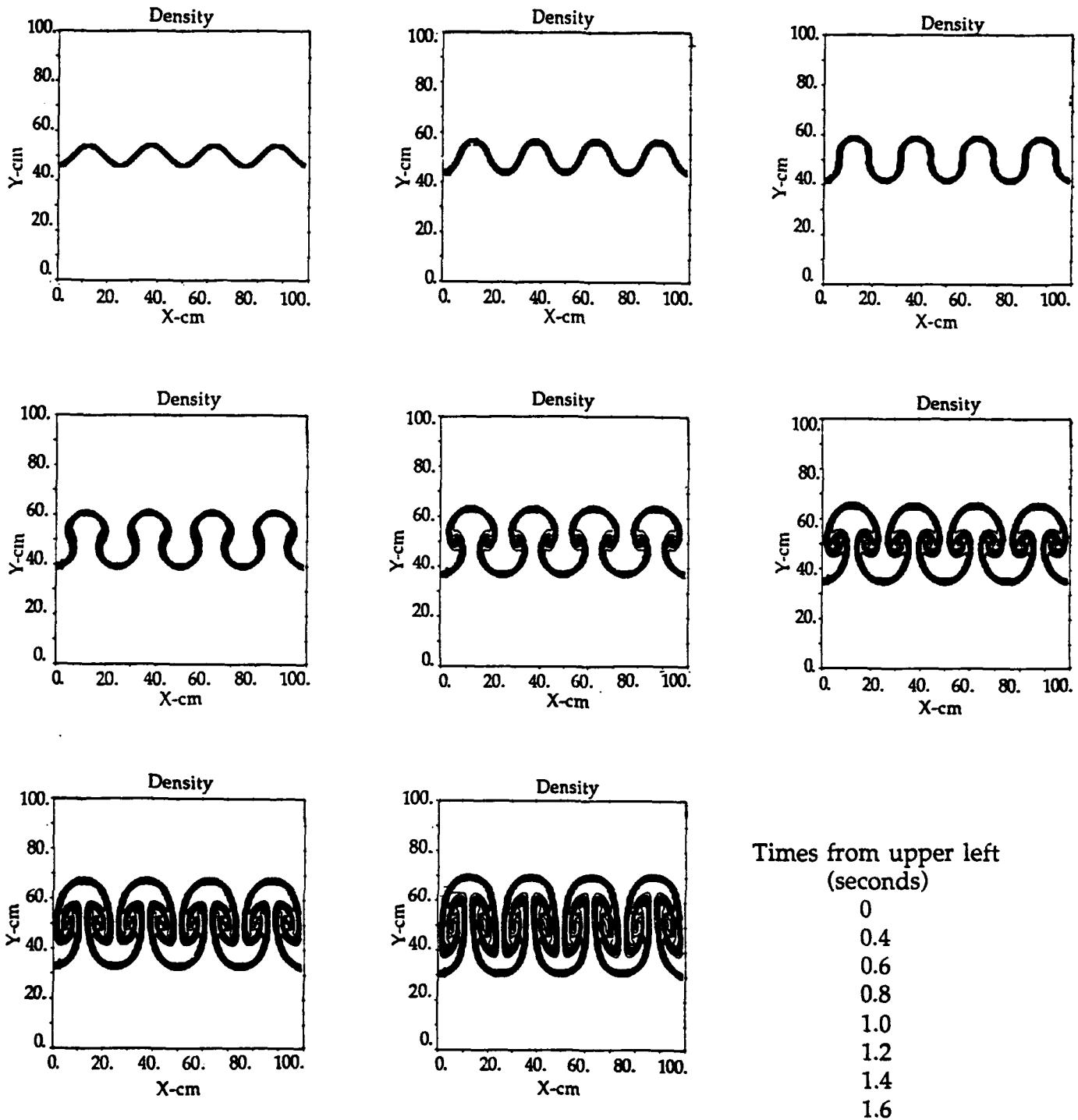
Figure 26. 1-cm resolution, 4-zone initial amplitude, wave number = 0.08 •π.

Times from upper left (seconds)

0

0.4

0.6

0.8

1.0

1.2

1.4

1.6
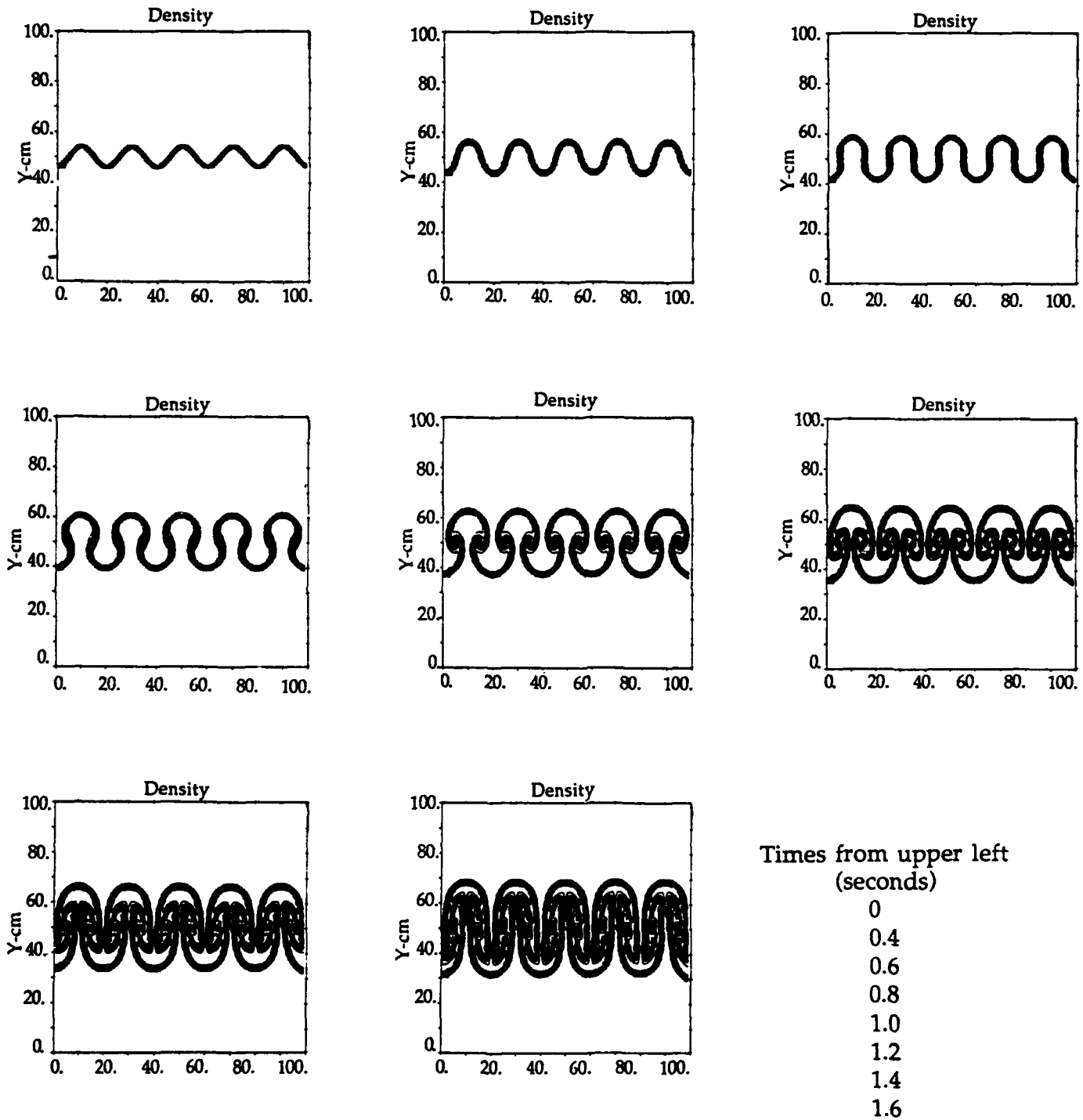
Figure 27. 1-cm resolution, 4-zone initial amplitude, wave number = 0.10 •π.

53
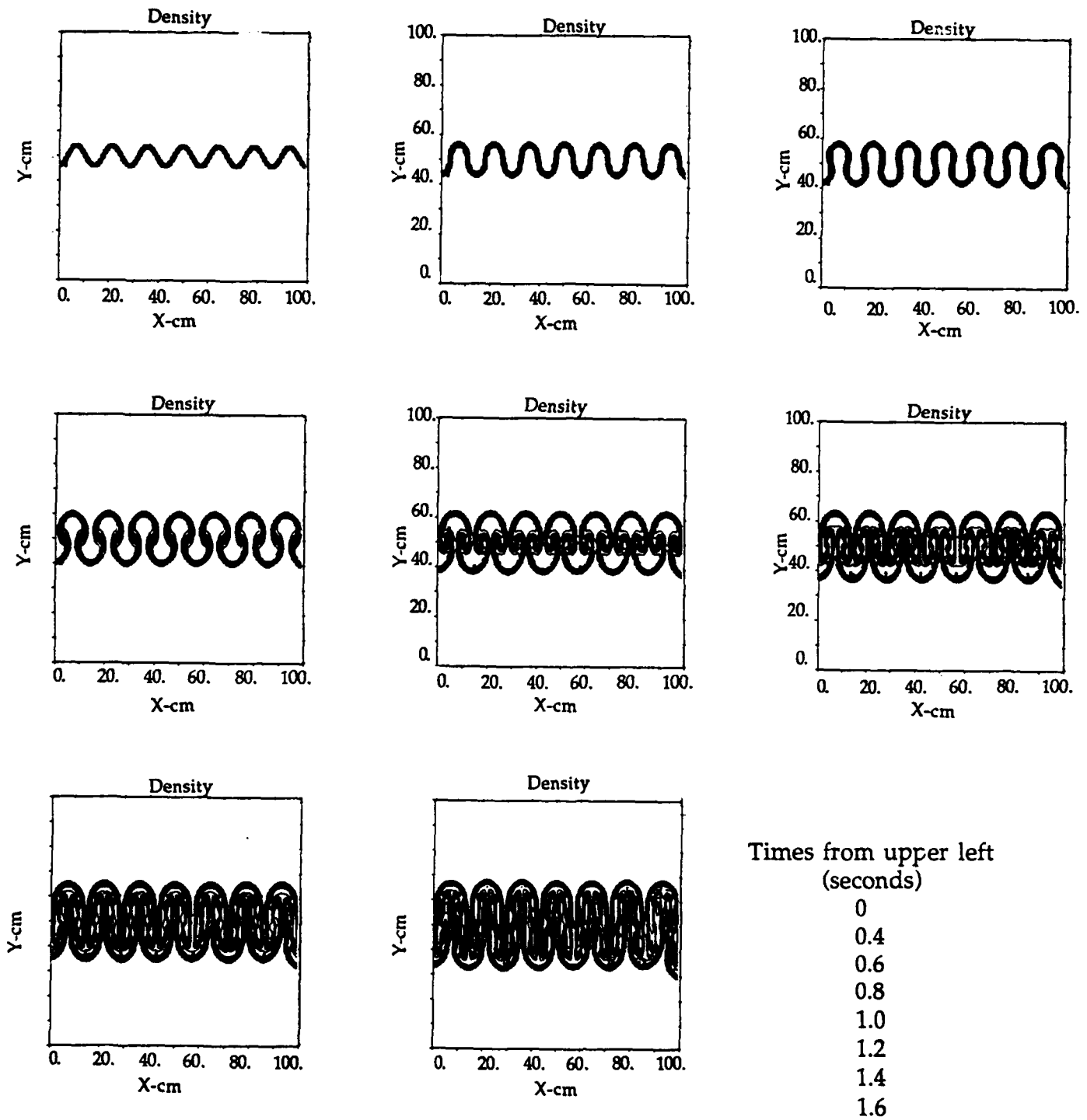
Figure 28. 1-cm resolution, 4-zone initial amplitude, wave number = 0.14 •π.

Times from upper left
(seconds)
0
0.4
0.6
0.8
1.0
1.2
1.4
1.6

Times from upper left
(seconds)
0
0.4
0.6
0.8
1.0
1.2
1.4
1.6
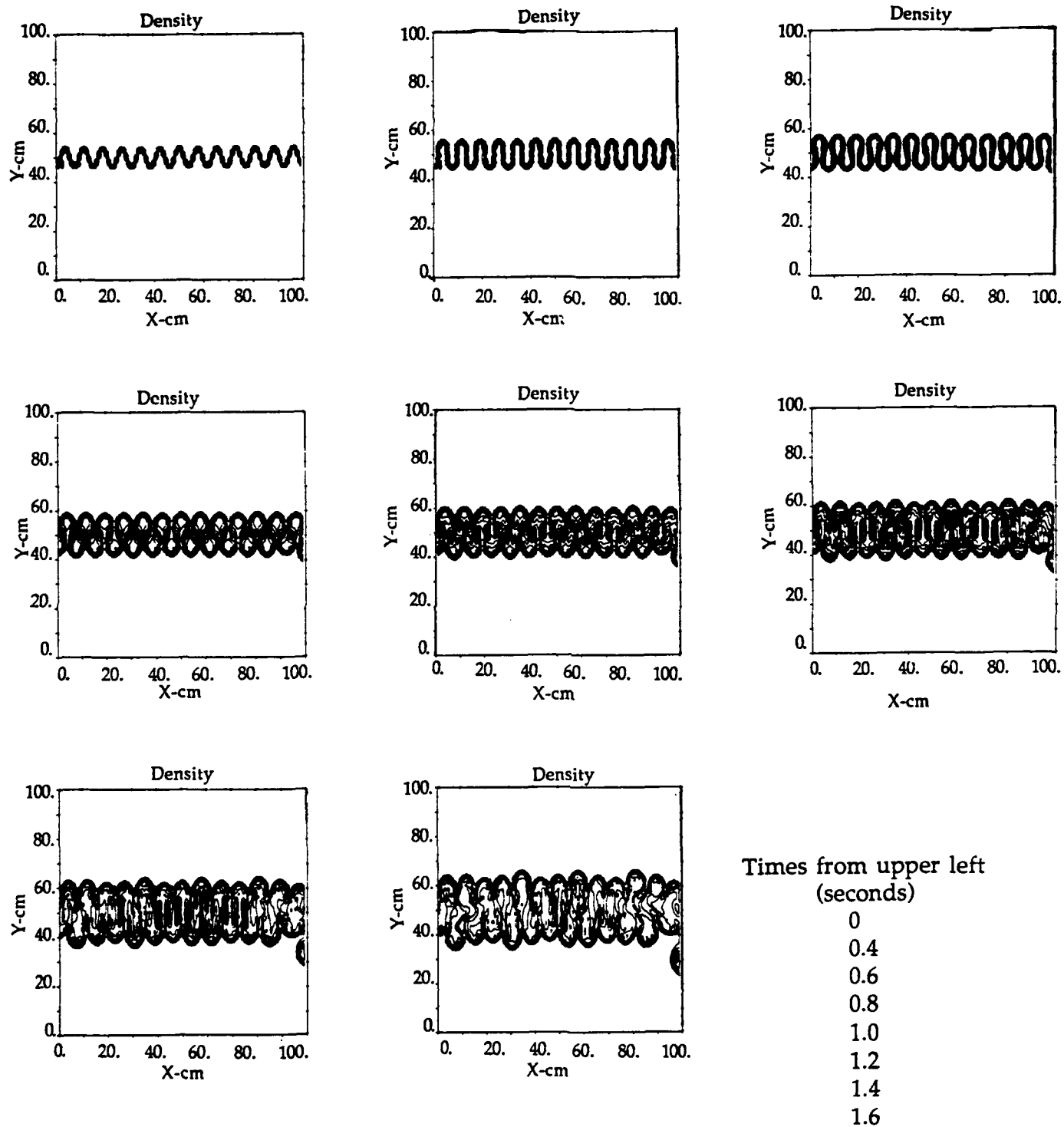
Figure 29. 1-cm resolution, 4-zone initial amplitude,
wave number = 0.26 •π.

APPENDIX C
RAYLEIGH-TAYLOR EXPERIMENTS AT 1-CM RESOLUTION,
2-ZONE INITIAL AMPLITUDE

—

Times from upper left
(seconds)
0
0.4
0.6
0.8
1.0
1.2
1.4
1.6

Figure 30. 1.0-cm resolution, 2-zone initial amplitude,
wave number = 0.04 •π.

Times from upper left
(seconds)
0
0.4
0.6
0.8
1.0
1.2
1.4
1.6
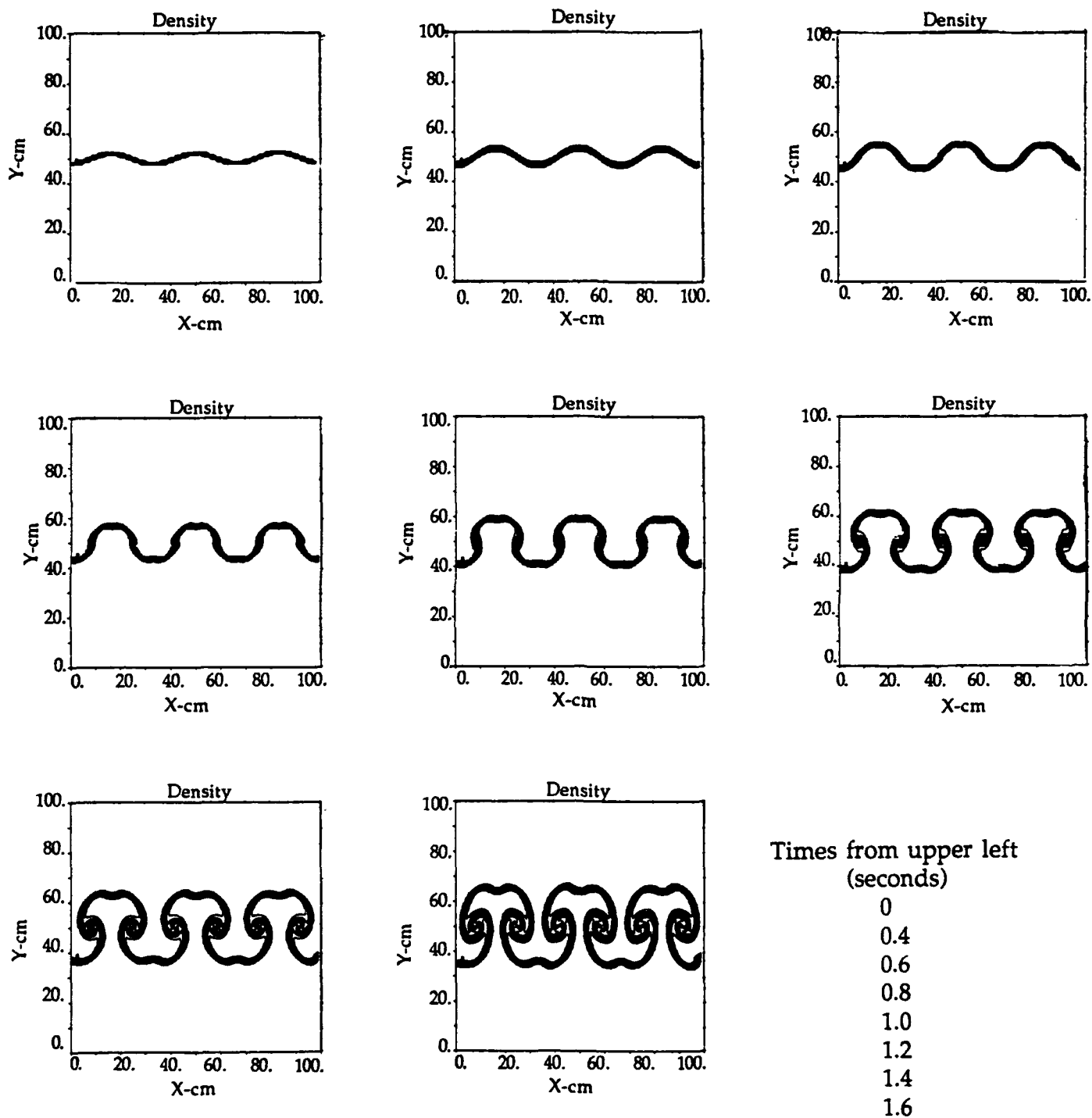
Figure 31. 1.0-cm resolution, 2-zone initial amplitude,
wave number = 0.06 •π.
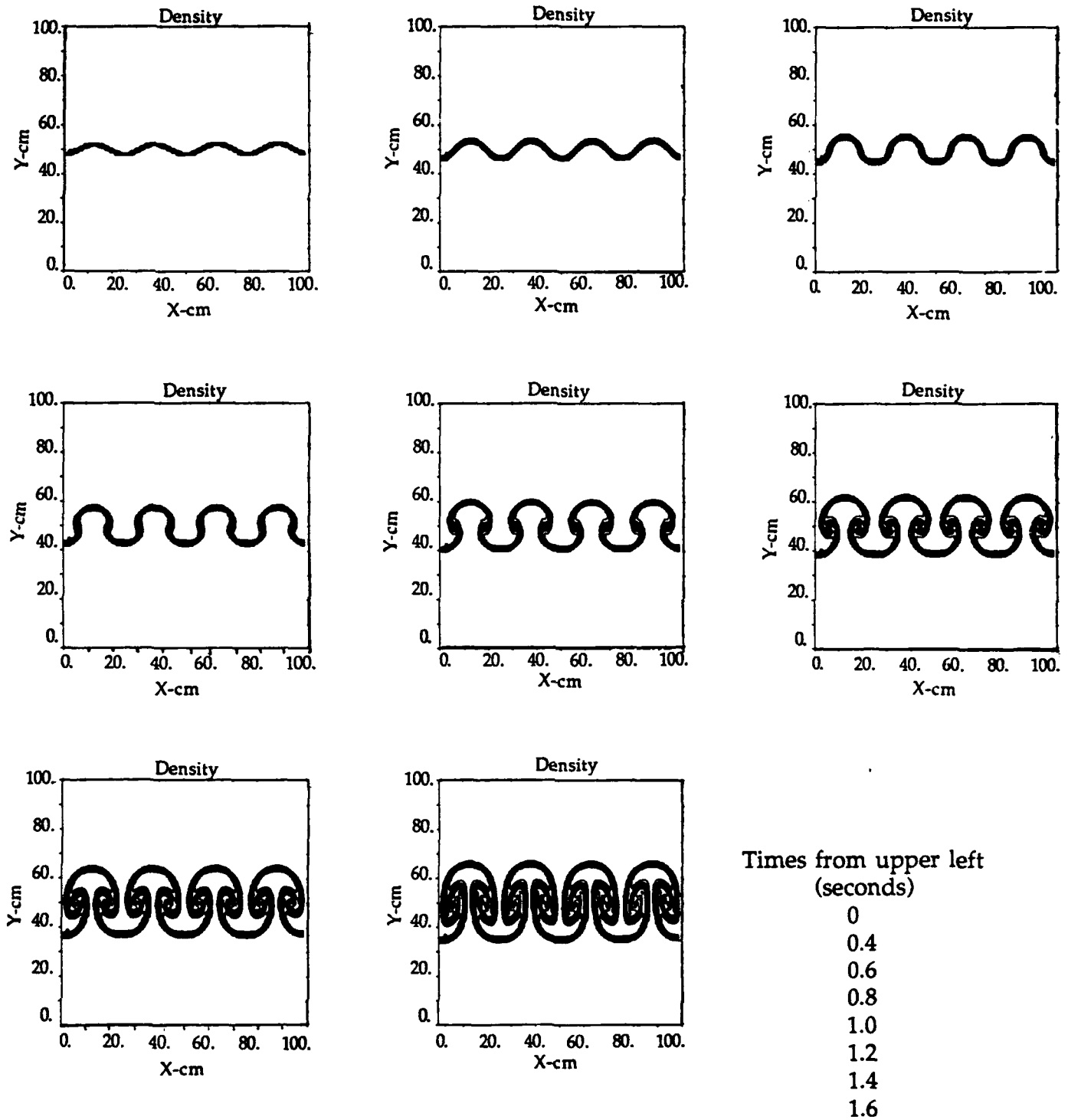
Figure 32. 1.0-cm resolution, 2-zone initial amplitude, wave number = 0.08 •π.

Times from upper left
(seconds)
0
0.4
0.6
0.8
1.0
1.2
1.4
1.6

Times from upper left
(seconds)

0

0.4

0.6

0.8

1.0

1.2

1.4

1.6
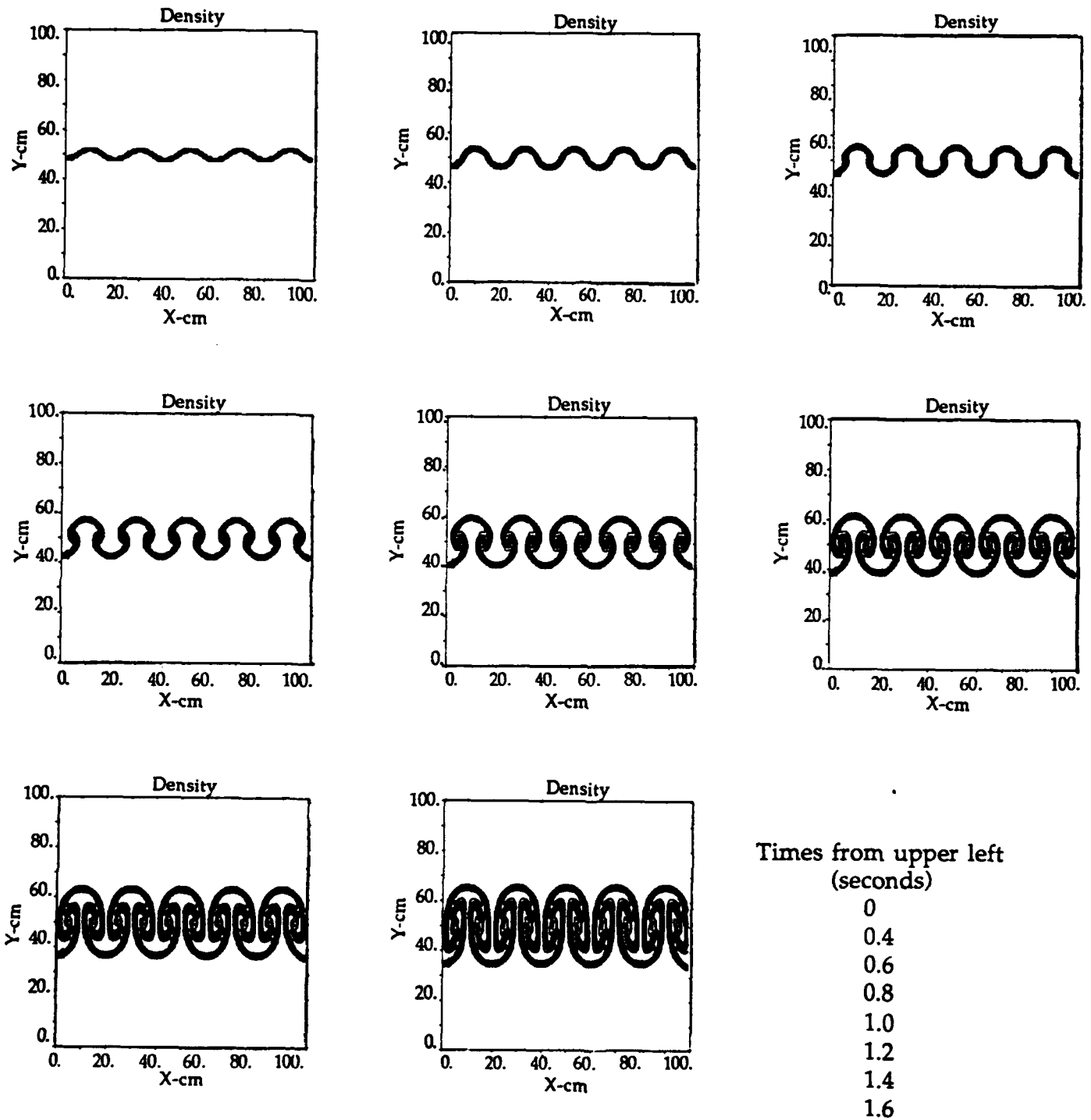
Figure 33. 1.0-cm resolution, 2-zone initial amplitude,
wave number = 0.10 •π.

Times from upper left
(seconds)

0

0.4

0.6

0.8

1.0

1.2

1.4

1.6
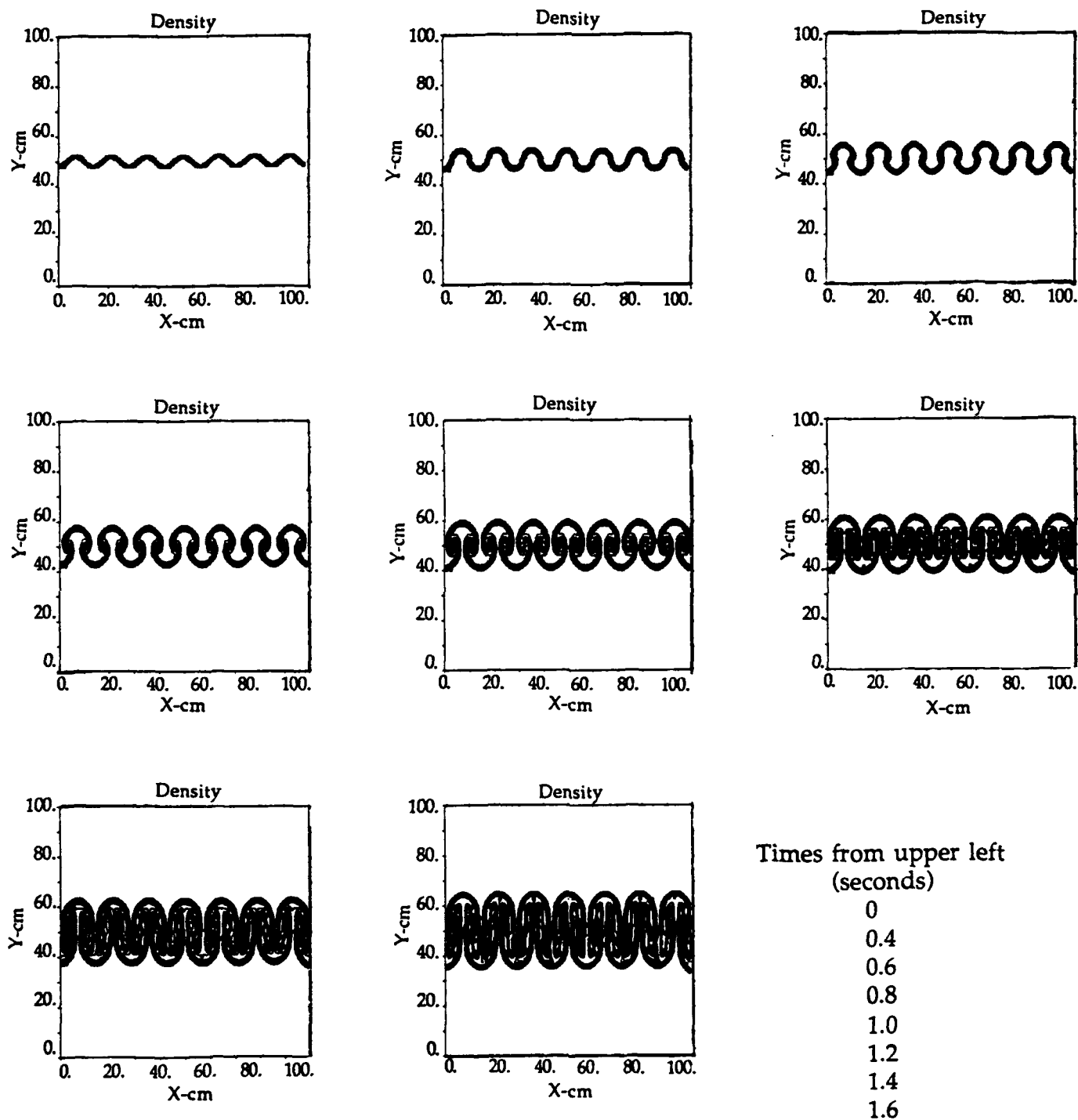
Figure 34. 1.0-cm resolution, 2-zone initial amplitude,
wave number = 0.14 • π.

Times from upper left
(seconds)
0
0.4
0.6
0.8
1.0
1.2
1.4
1.6
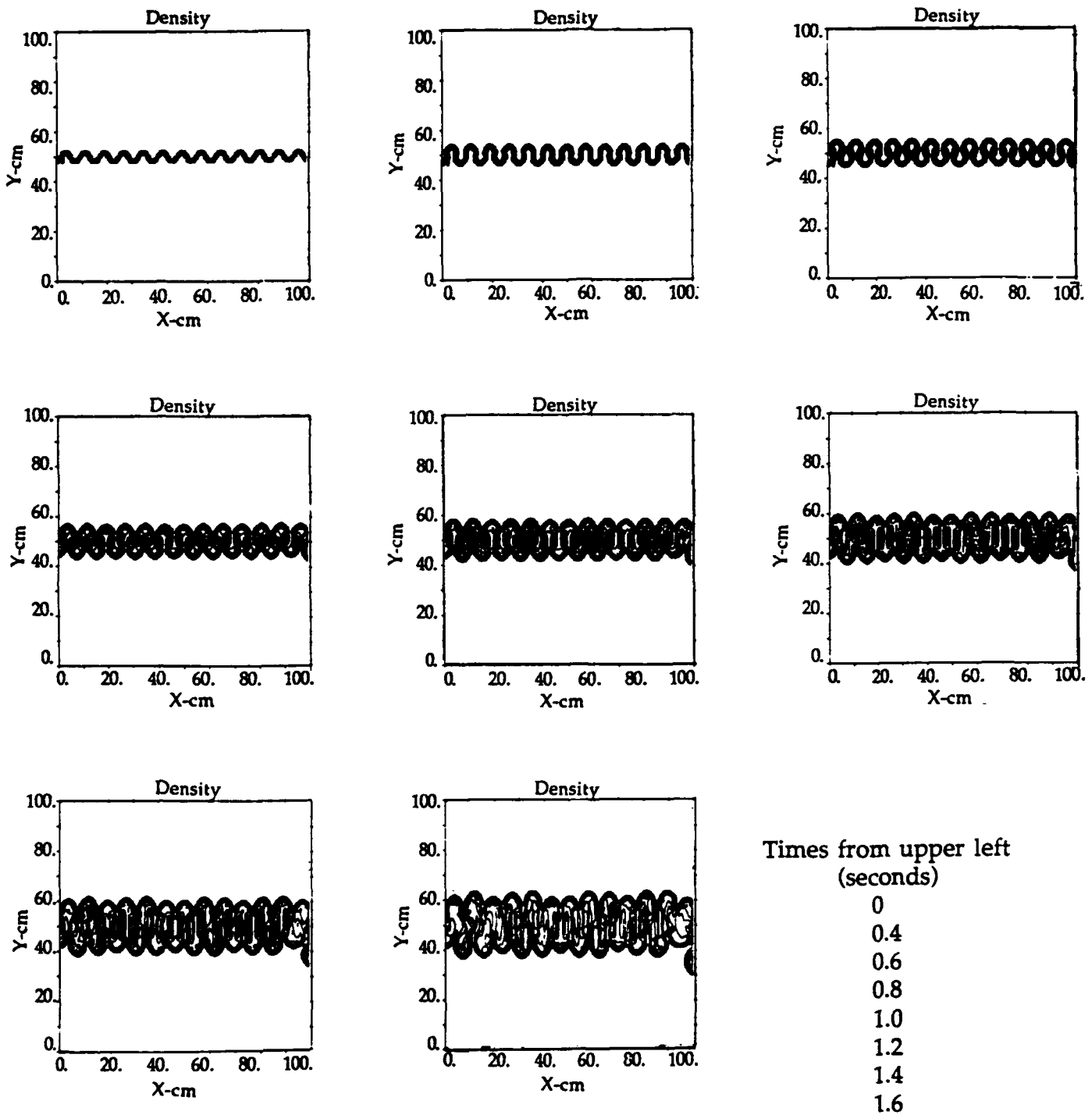
Figure 35. 1.0-cm resolution, 2-zone initial amplitude,
wave number = 0.26 •π.

APPENDIX D
RAYLEIGH-TAYLOR EXPERIMENTS AT 0.5-CM RESOLUTION, 2-ZONE INITIAL AMPLITUDE
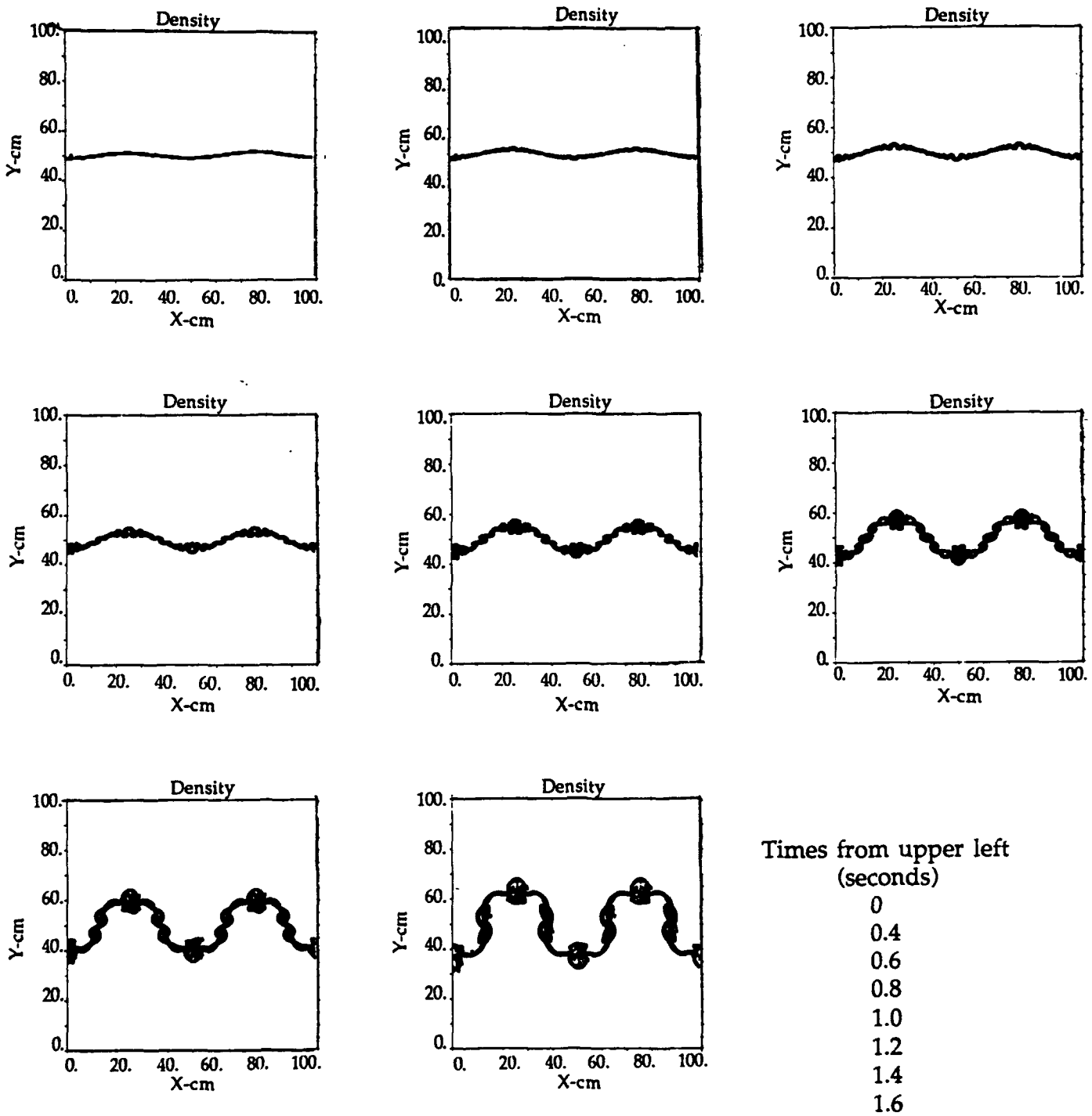
Figure 36. 0.5-cm resolution, 2-zone initial amplitude, wave number = 0.04 •π.

Times from upper left
(seconds)
0
0.4
0.6
0.8
1.0
1.2
1.4
1.6

Rayleigh-Taylor Experiments with CLOUD Code

Density (×8 panels with Y-cm vs X-cm axes)

Times from upper left
(seconds)
0
0.4
0.6
0.8
1.0
1.2
1.4
1.6
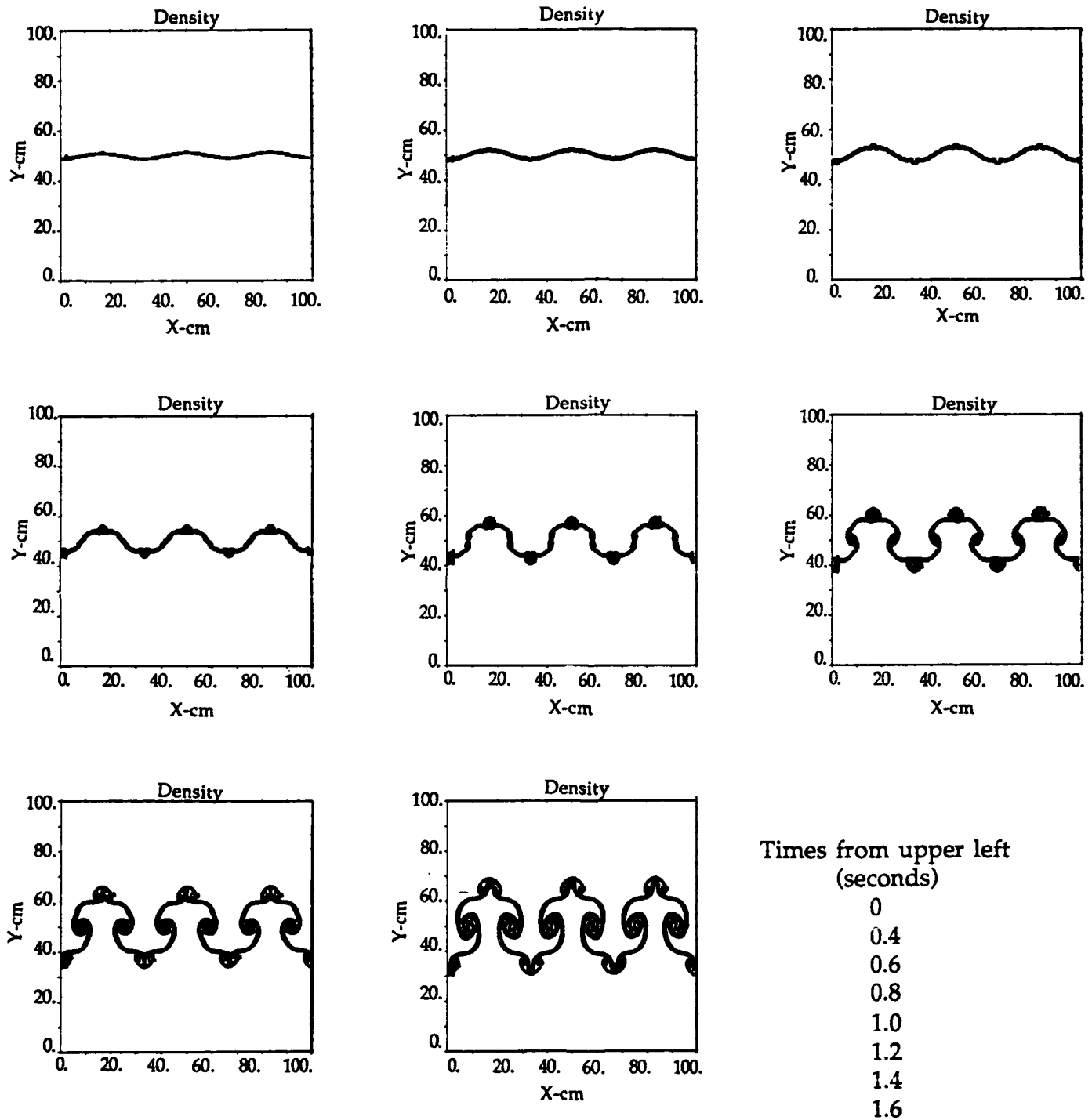
Figure 37. 0.5-cm resolution, 2-zone initial amplitude,
wave number = 0.06 •π.

Density

Density

Density

Density

Density

Density

Density

Density

Times from upper left
(seconds)

0

0.4

0.6

0.8

1.0

1.2

1.4

1.6
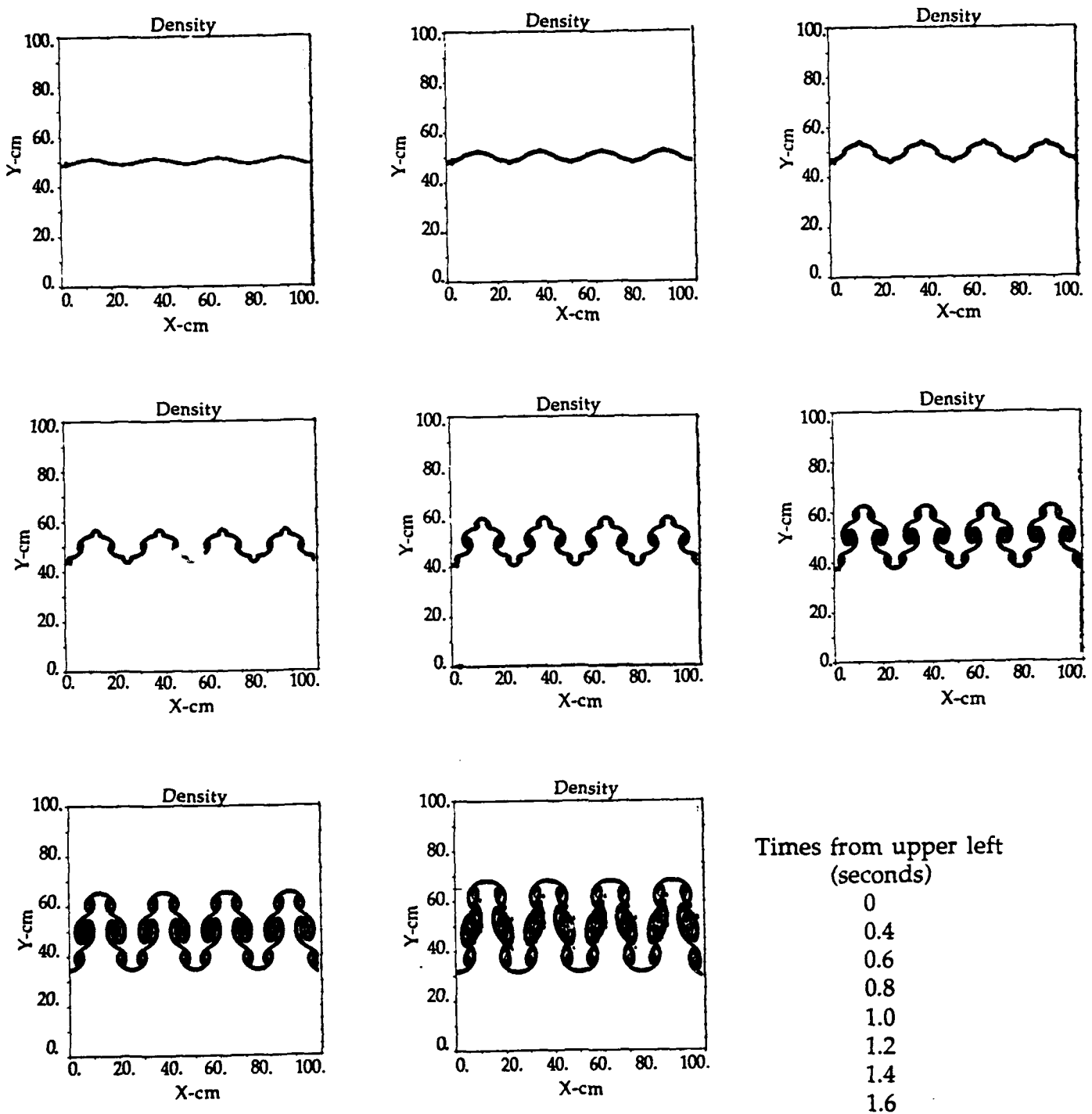
Figure 38. 0.5-cm resolution, 2-zone initial amplitude,
wave number = 0.08 •π.

Times from upper left
(seconds)

0

0.4

0.6

0.8

1.0

1.2

1.4

1.6
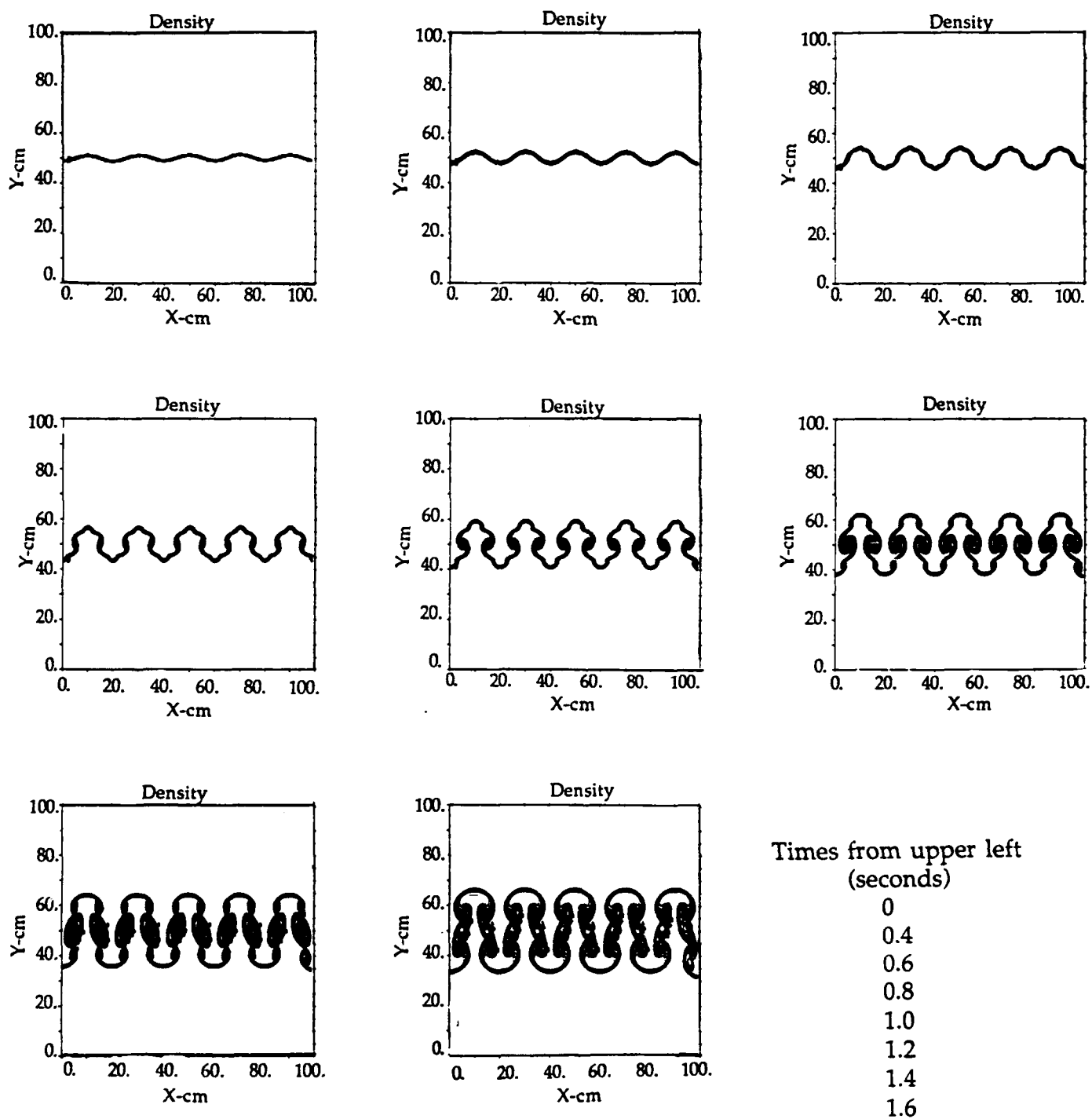
Figure 39. 0.5-cm resolution, 2-zone initial amplitude,
wave number = 0.10 •π.

Times from upper left
(seconds)
0
0.4
0.6
0.8
1.0
1.2
1.4
1.6
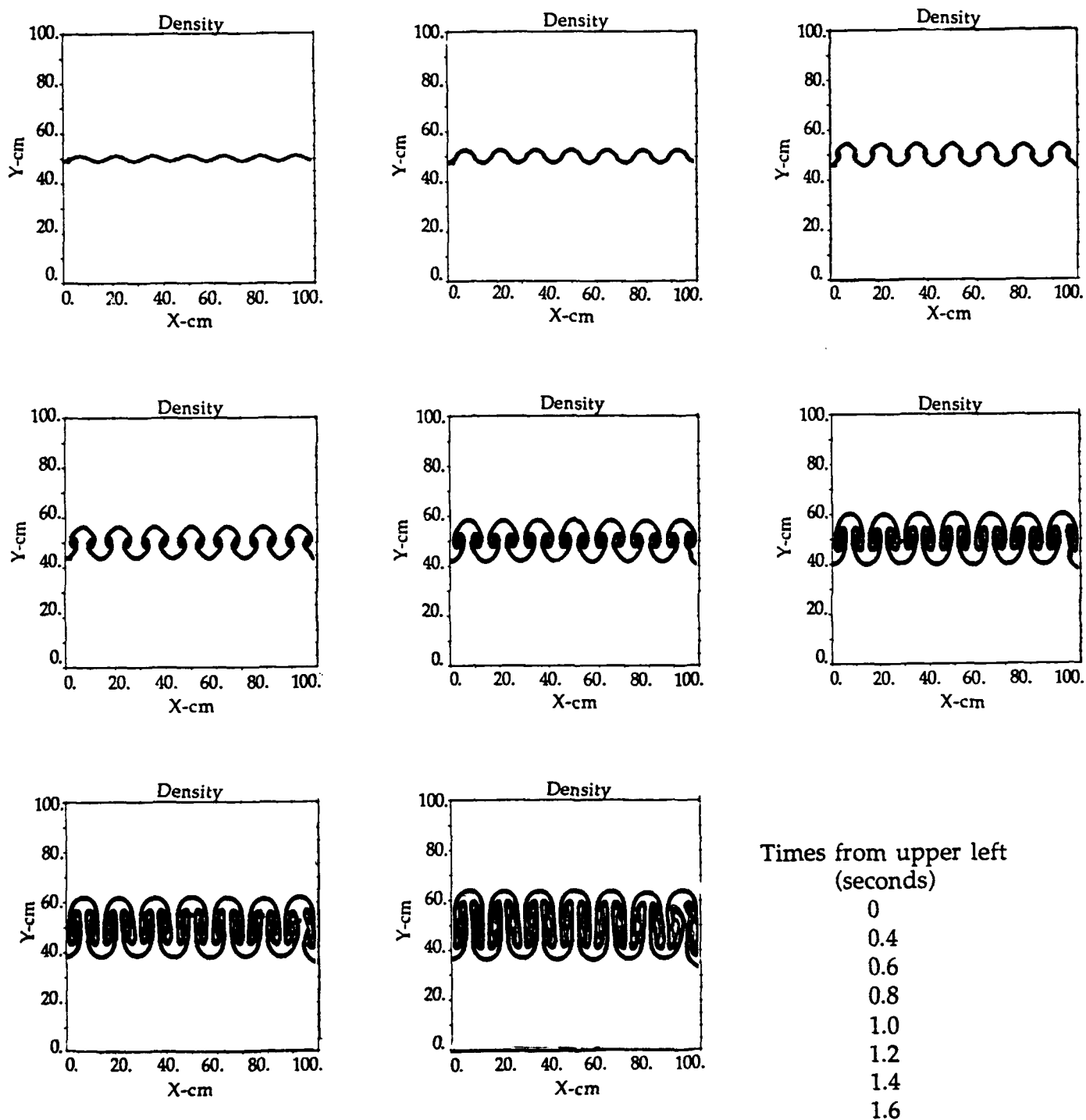
Figure 40. 0.5-cm resolution, 2-zone initial amplitude,
wave number = 0.14 •π.

Times from upper left
(seconds)

0

0.4

0.6

0.8

1.0

1.2

1.4

1.6
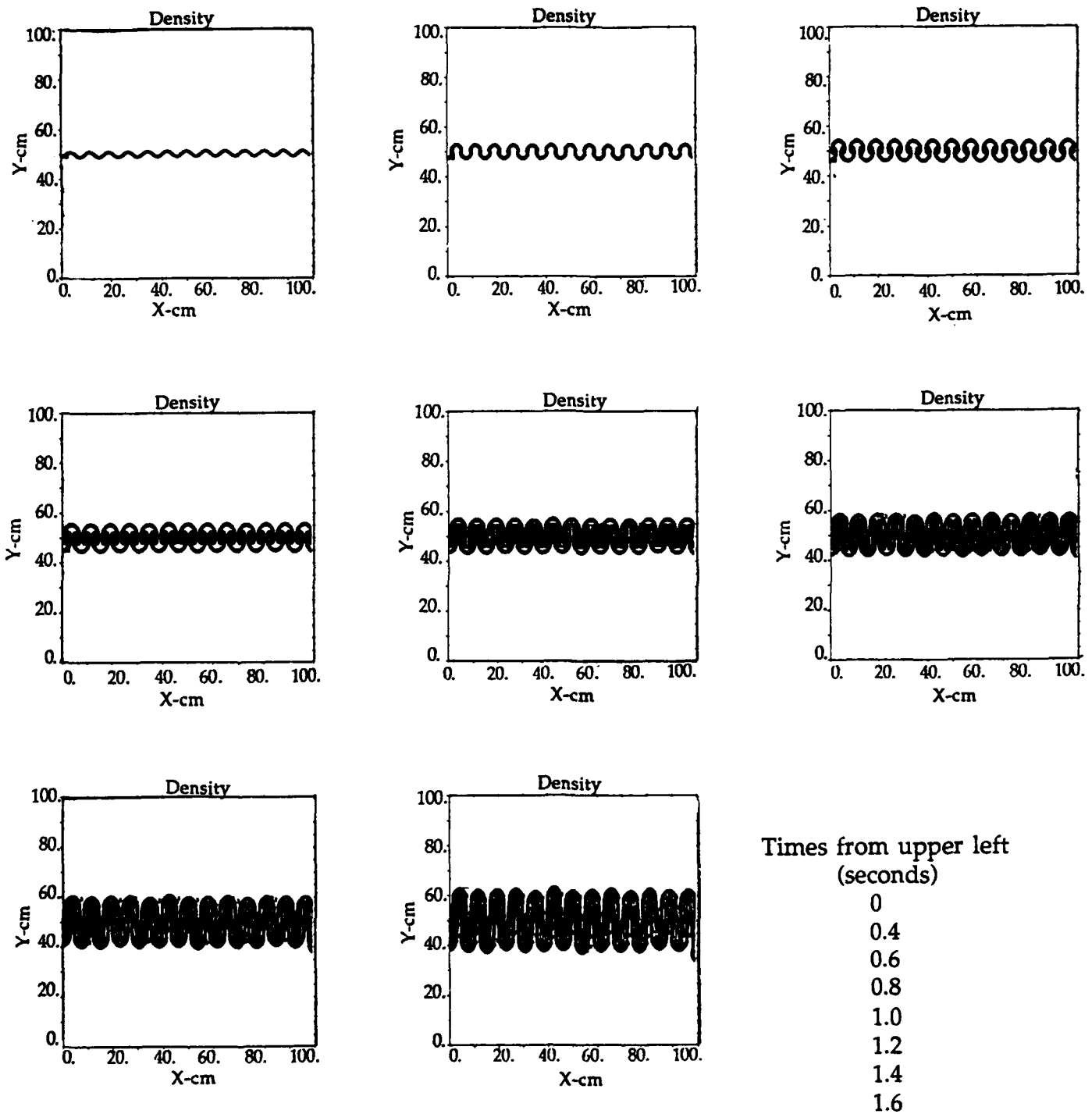
Figure 41. 0.5-cm resolution, 2-zone initial amplitude,
wave number = 0.26 •π.

71

APPENDIX E
RICHTMYER-MESKHOV EXPERIMENTS AT 2-CM RESOLUTION

Times from upper left
(μs)
50
100
200
300
400
500
600
700
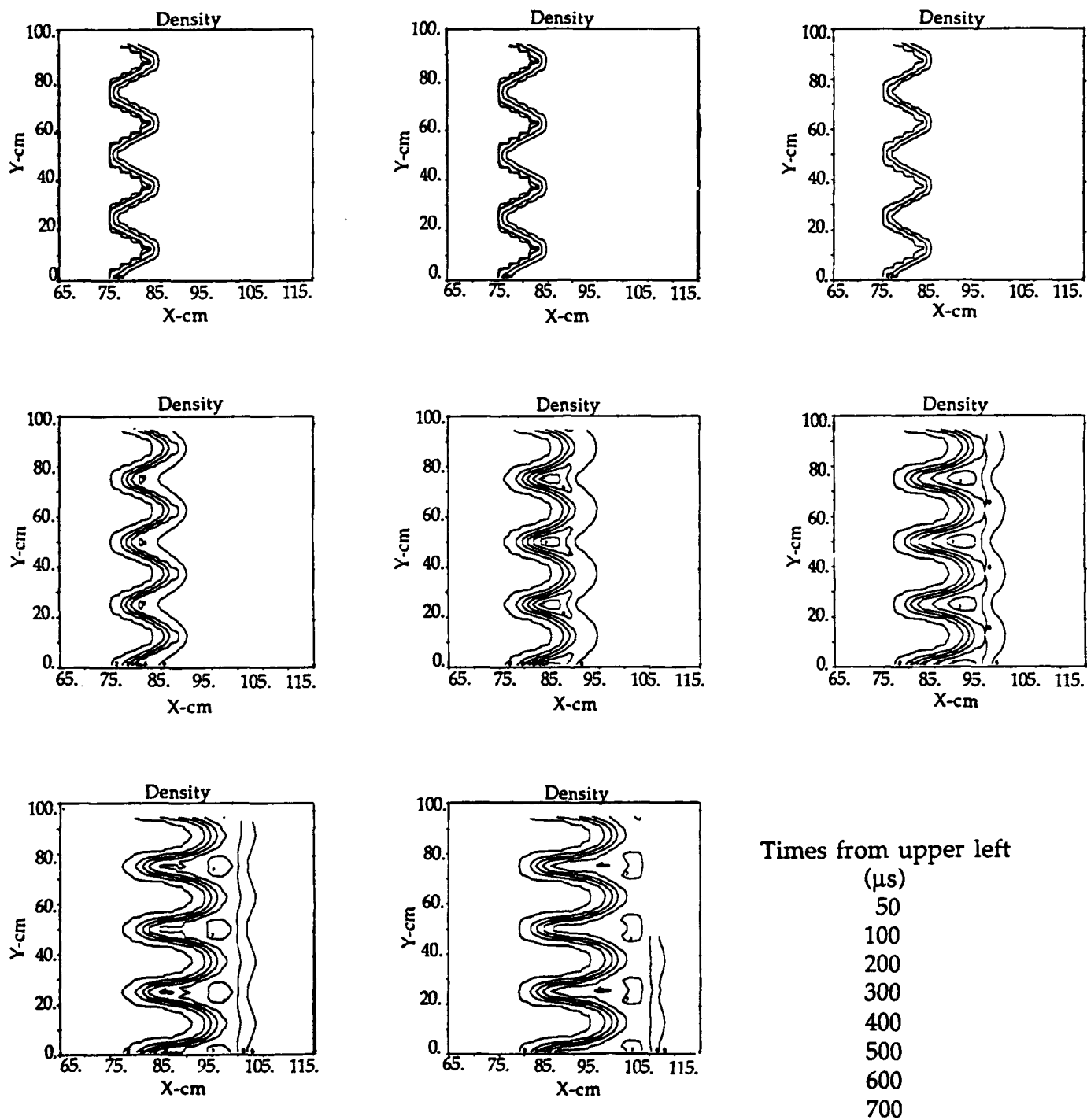
Figure 42. 2-cm resolution, 2-zone initial amplitude,
wave number = 0.08 •π.

74

Times from upper left
(μs)
50
100
200
300
400
500
600
700
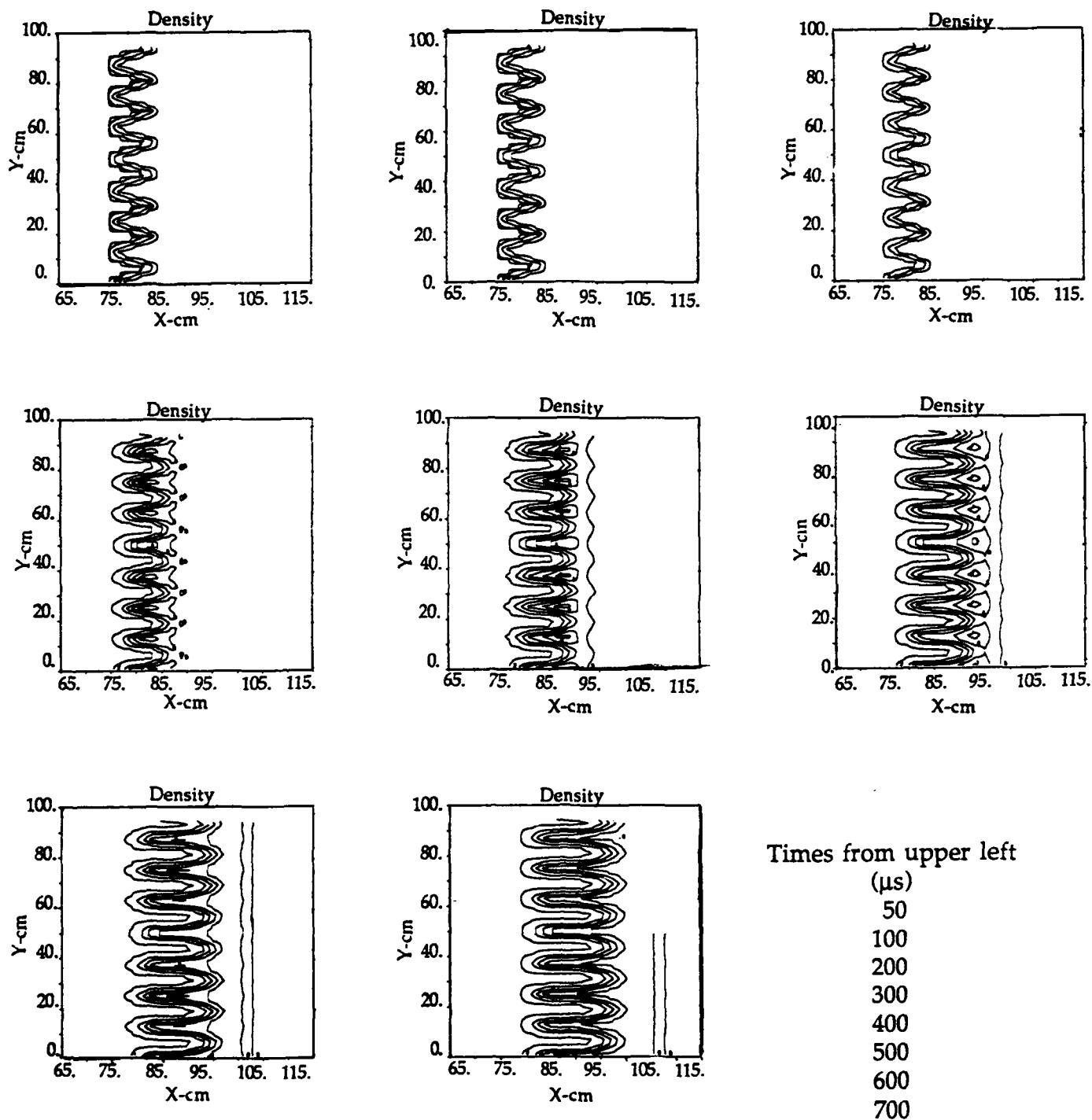
Figure 43. 2-cm resolution, 2-zone initial amplitude,
wave number = 0.16 •π.

75
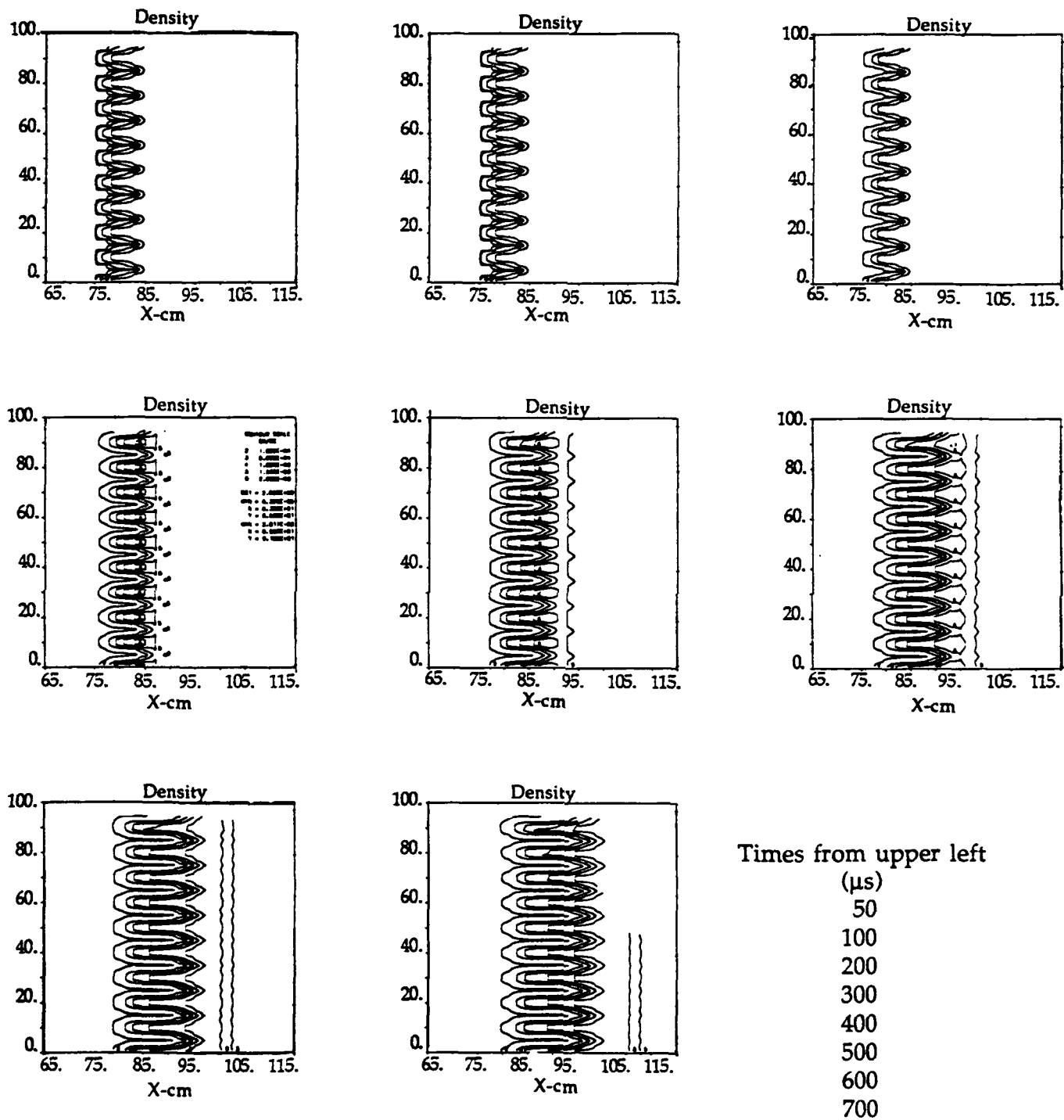
Figure 44. 2-cm resolution, 2-zone initial amplitude, wave number = 0.20 •π.

Times from upper left (μs)
50
100
200
300
400
500
600
700

Times from upper left
(μs)
50
100
200
300
400
500
600
700
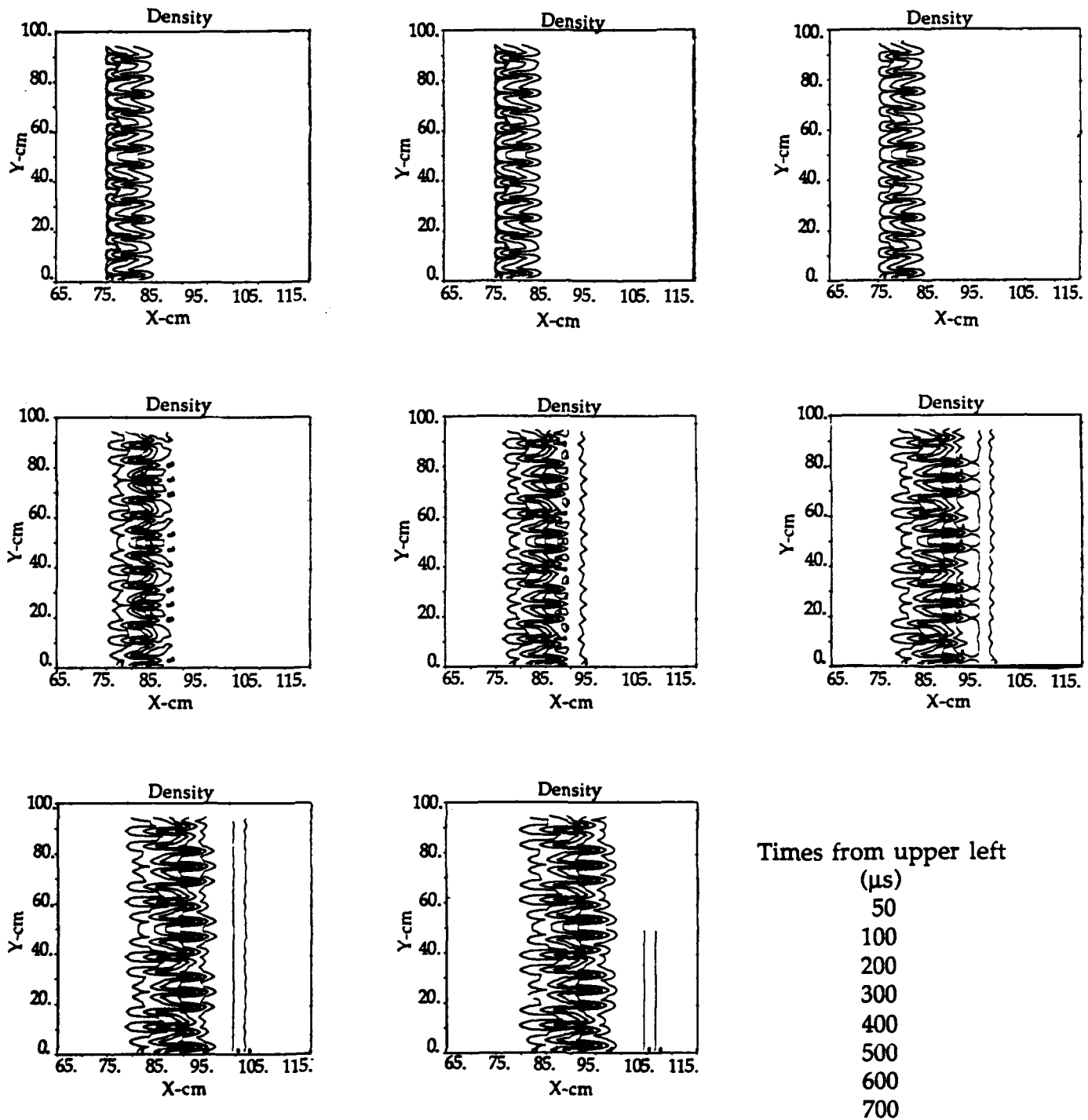
Figure 45. 2-cm resolution, 2-zone initial amplitude,
wave number ≈ 0.36 •π.

APPENDIX F
RICHTMYER-MESKHOV EXPERIMENTS AT 1-CM RESOLUTION

Times from upper left
(µs)

50
100
200
300
400
500
600
700
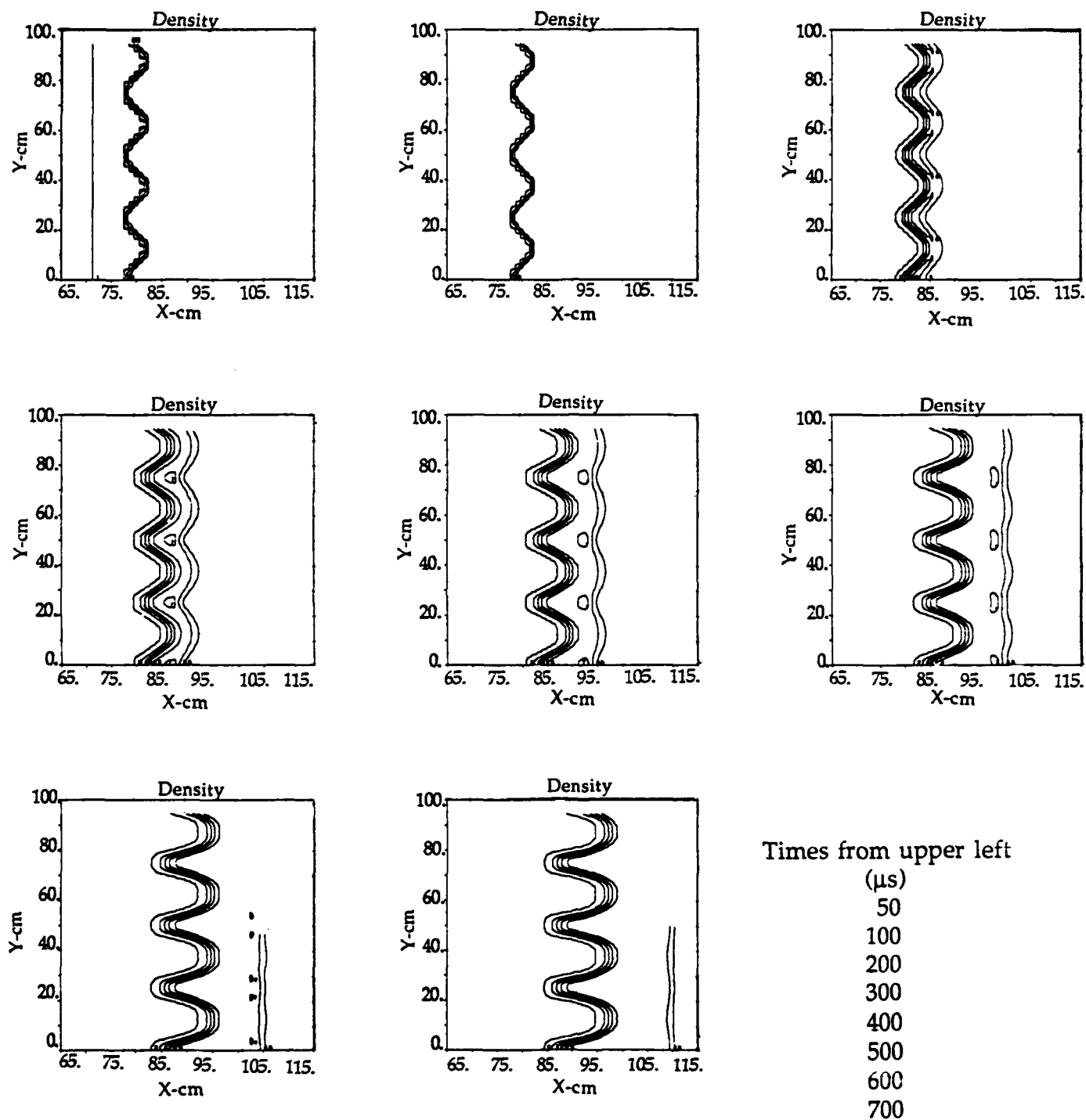
Figure 46. 1-cm resolution, 2-zone initial amplitude,
wave number = 0.08 •π.
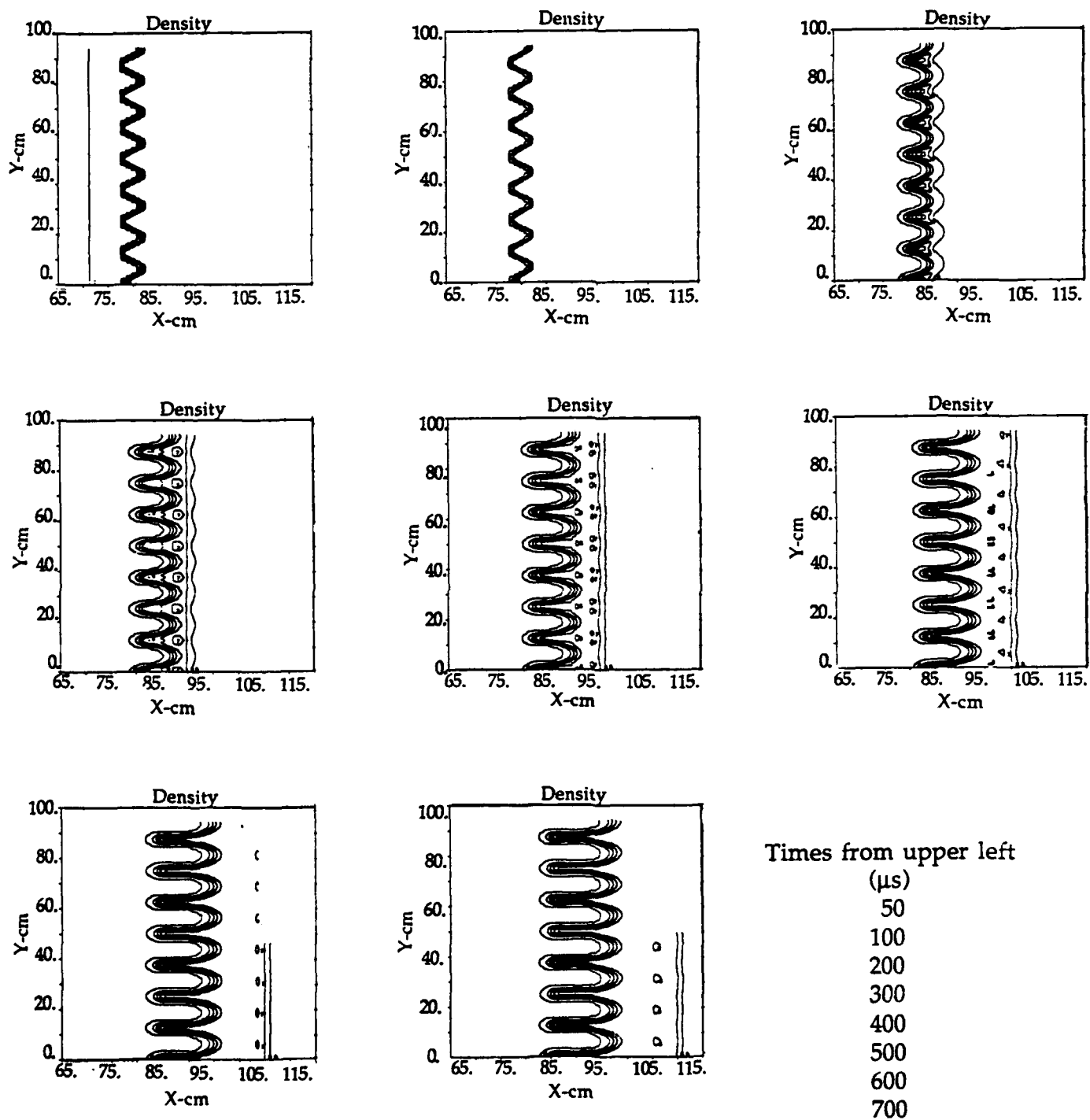
Figure 47. 1-cm resolution, 2-zone initial amplitude, wave number = 0.16 •π.

Times from upper left
(µs)
50
100
200
300
400
500
600
700
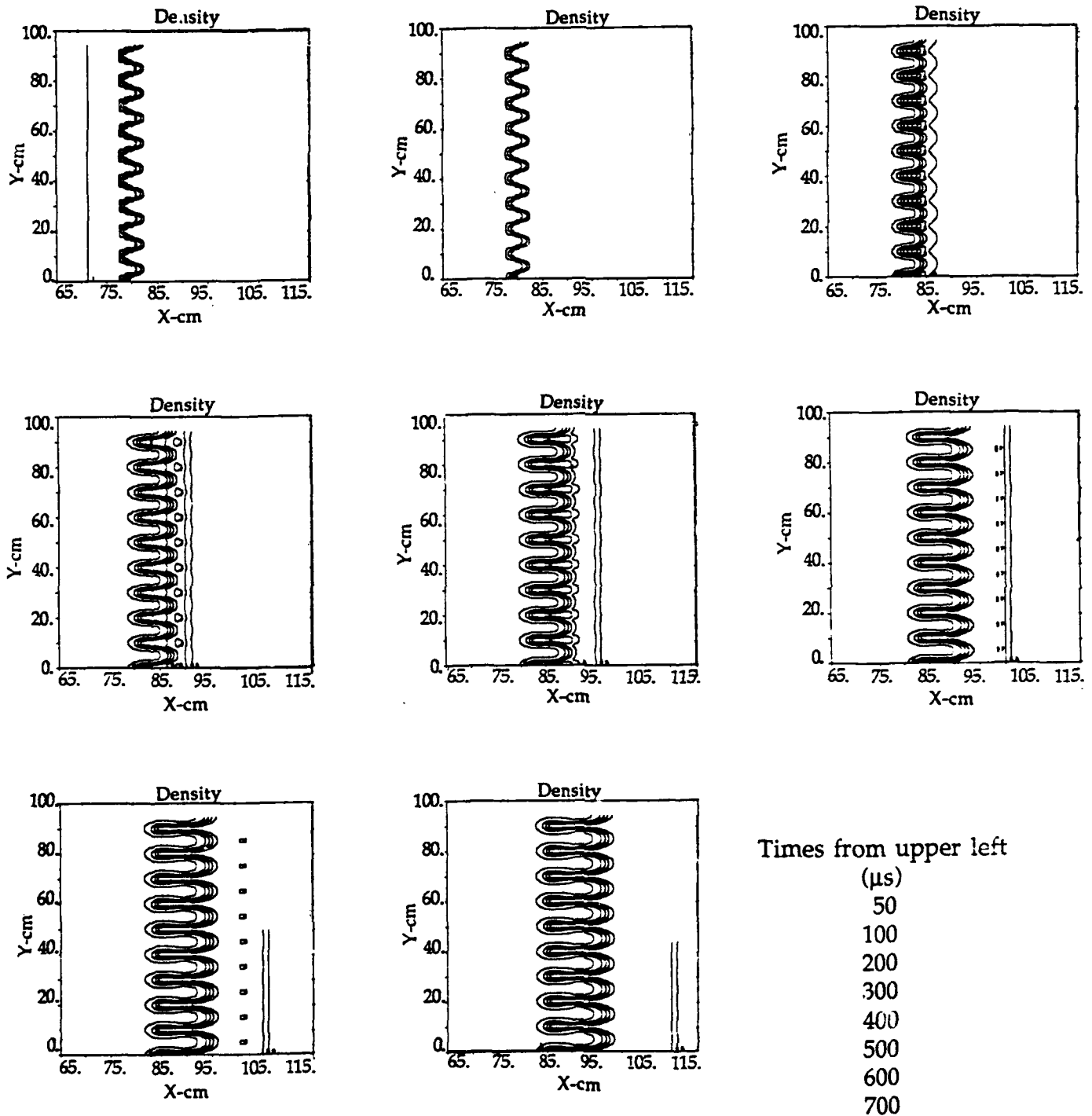
Figure 48. 1-cm resolution, 2-zone initial amplitude,
wave number = 0.20 •π.
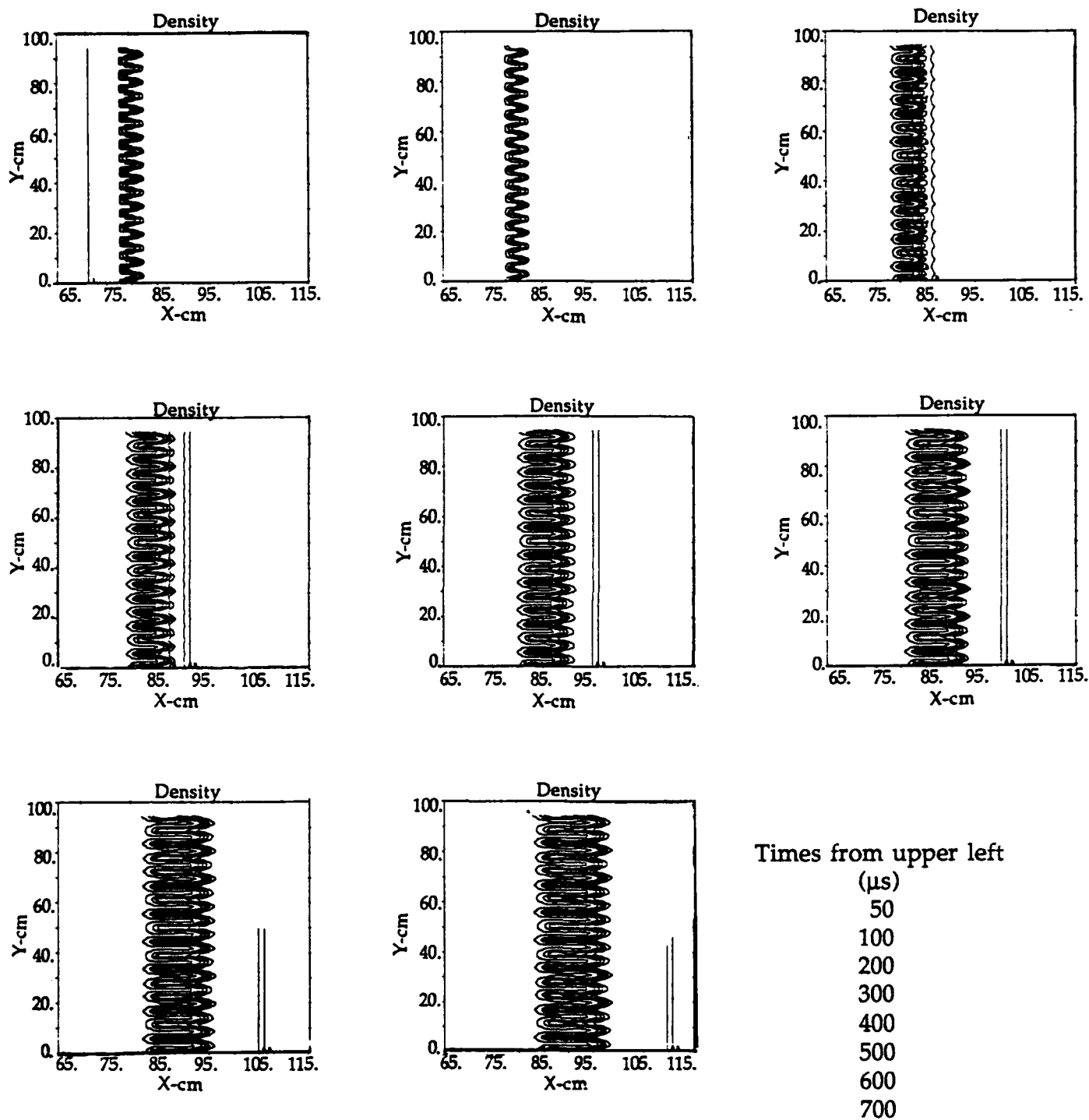
Figure 49. 1-cm resolution, 2-zone initial amplitude,
wave number = 0.36 •π.

Times from upper left
(μs)
50
100
200
300
400
500
600
700

83

APPENDIX G
RICHTMYER-MESKHOV EXPERIMENTS AT 0.5-CM RESOLUTION
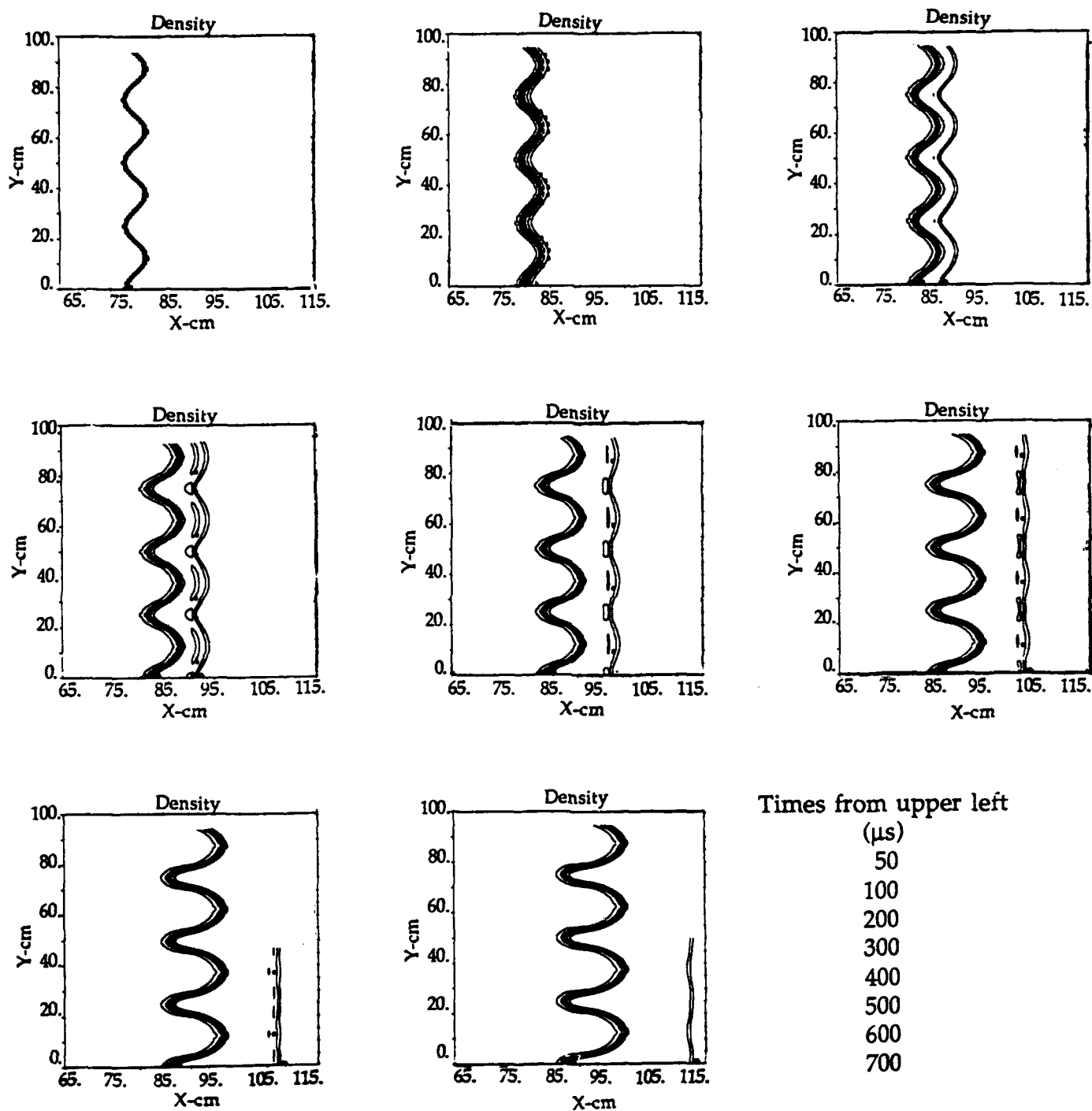
Figure 50. 0.5 cm resolution, 4-zone initial amplitude,
wave number = 0.08 • π.
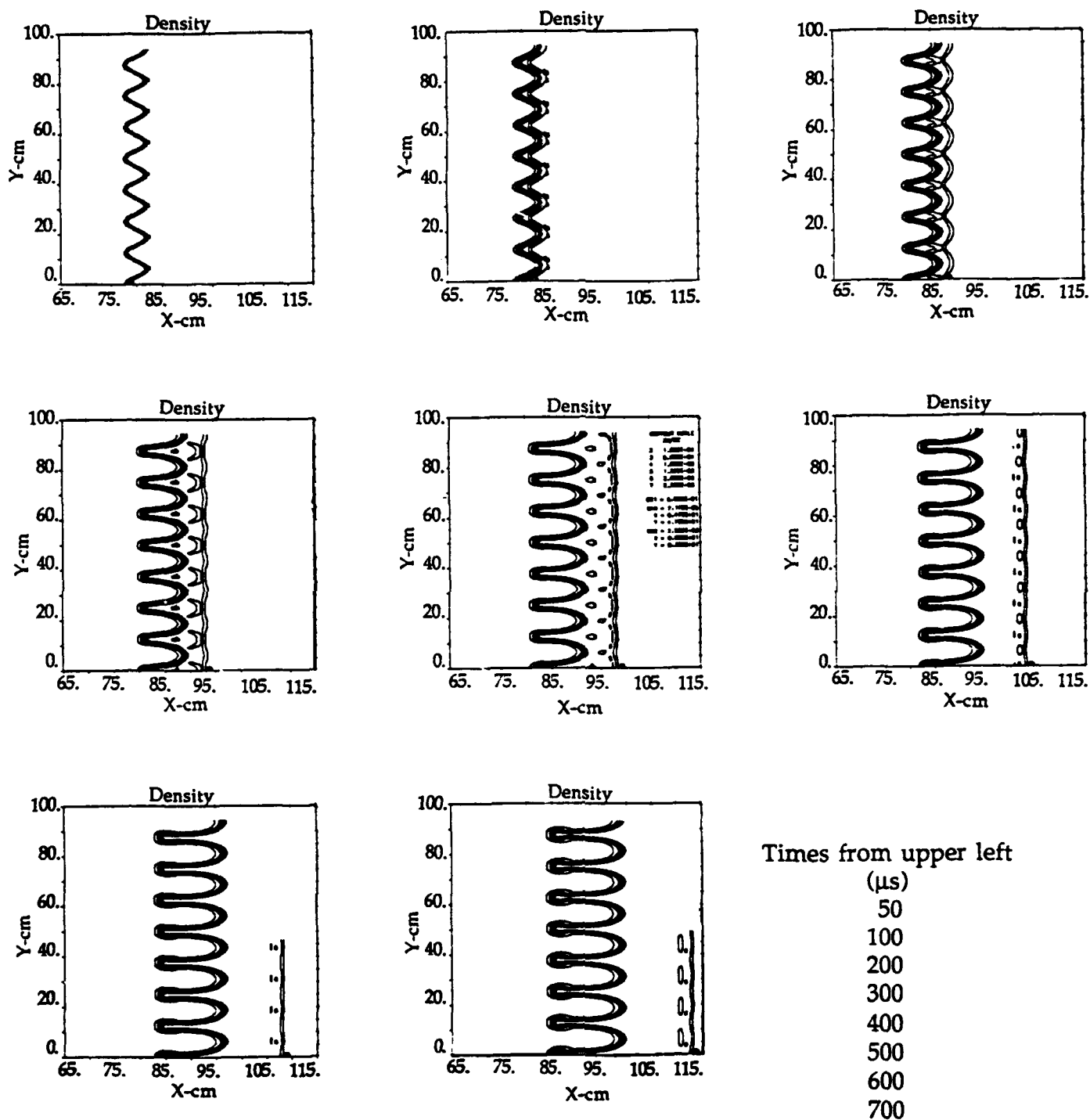
Figure 51. 0.5-cm resolution, 4-zone initial amplitude,
wave number = 0.16 •π.

Times from upper left
(μs)
50
100
200
300
400
500
600
700
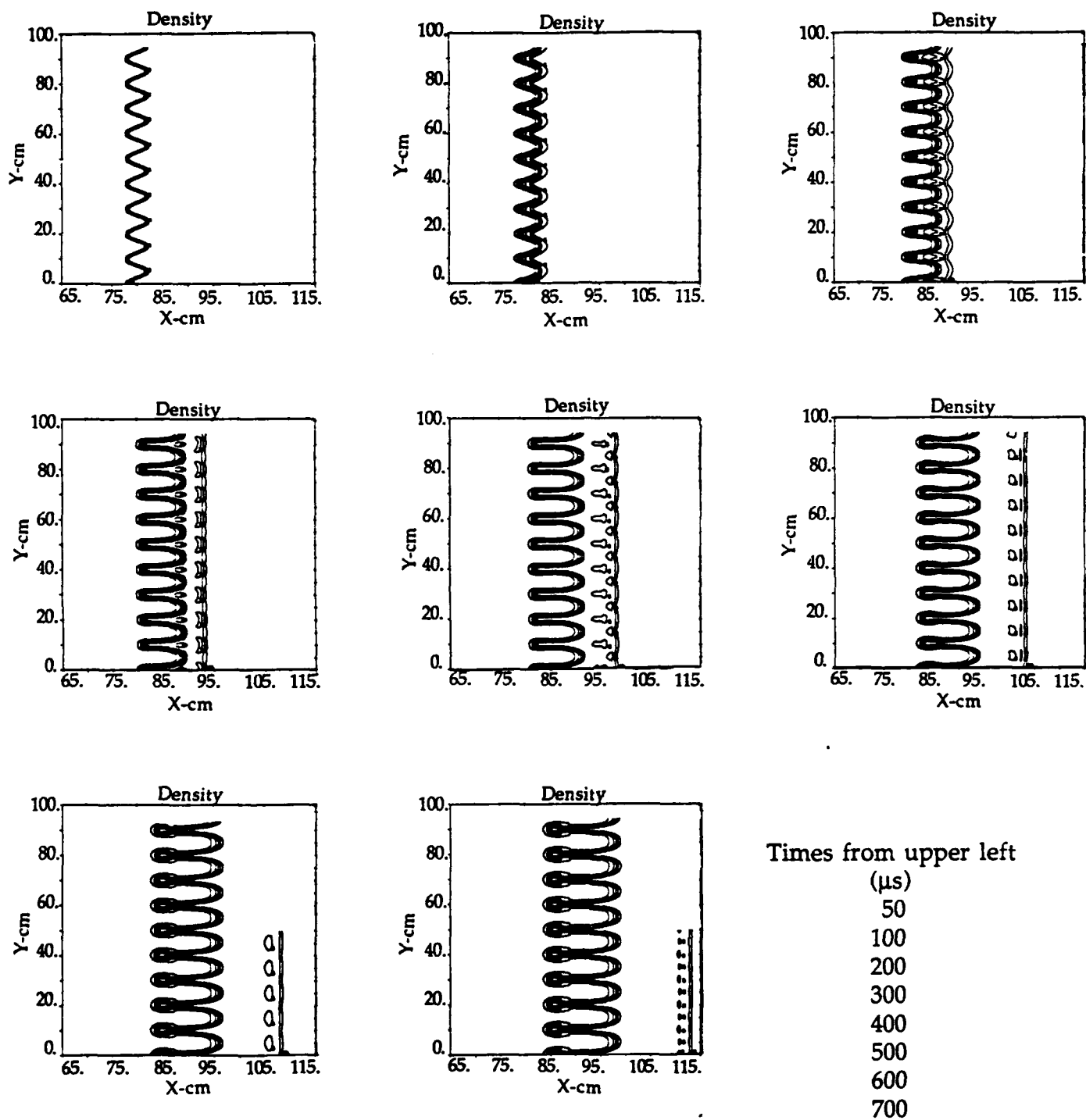
Figure 52. 0.5-cm resolution, 4-zone initial amplitude,
wave number = 0.20 •π.
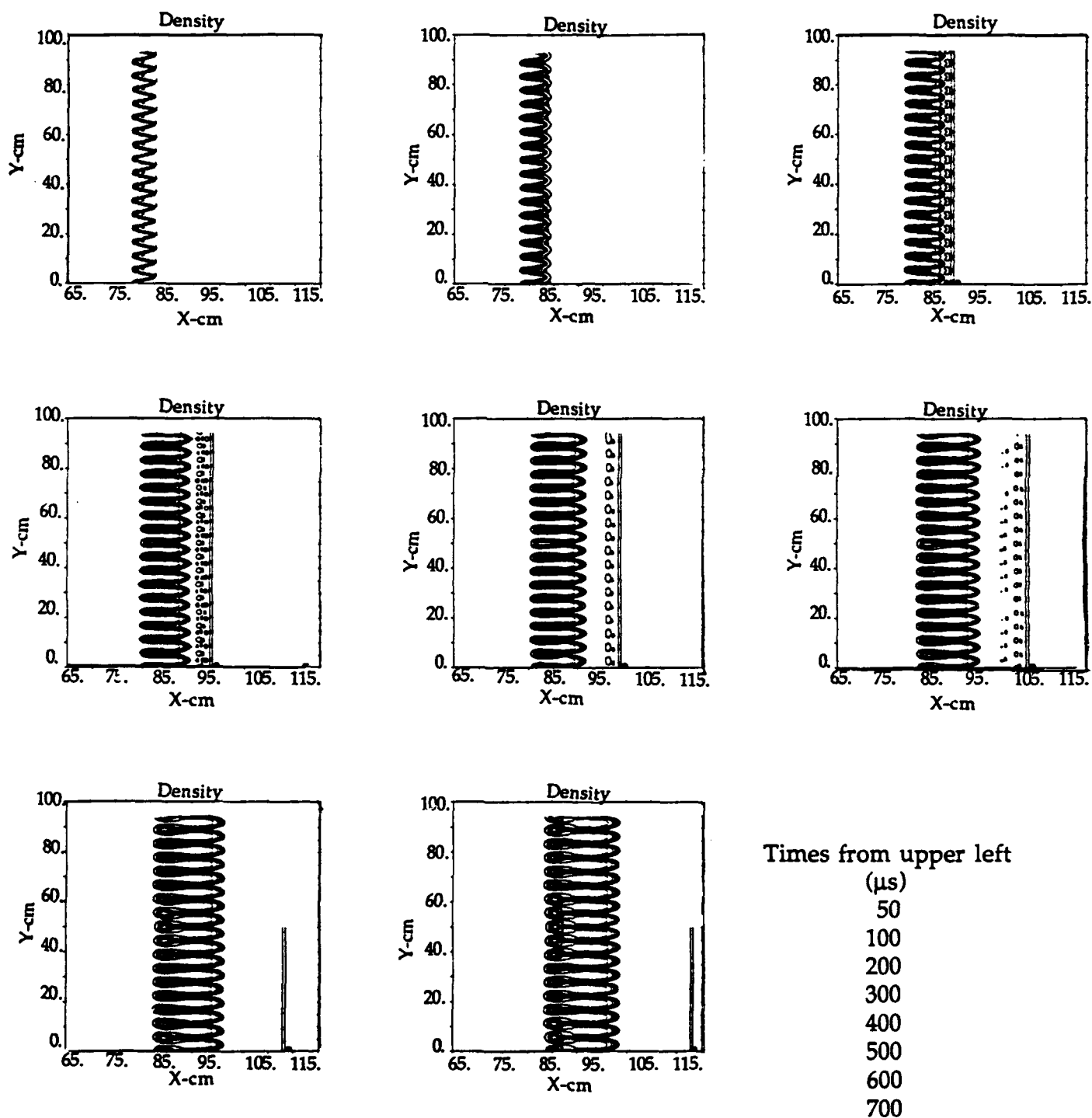
Figure 53. 0.5-cm resolution, 4-zone initial amplitude,
wave number = 0.36 •π.

APPENDIX H
FIRST-ORDER VERSUS SECOND-ORDER COMPARISON OF 200 KT AT 50 KM

This section provides comparison plots of first order and second order SHARC calculations of 200 KT at 50 km. The plots clearly illustrate the magnitude of the differences brought about by a second order advection algorithm.

By 30 seconds in the second-order calculation, the density gradients at the fireball edge are much steeper than those in the first-order calculation, and the speed contours suggest the presence of an instability near the fireball top. By 60 seconds, the instability is evident in the pressure field and a secondary thermal has begun to form at the fireball top. The minimum density in the second-order calculation is smaller by more than a factor of two by this time. By 90 seconds, the secondary thermal is well developed and a bulge of approximately the same wavelength has begun to form at the side. At two minutes, the torus in the second-order calculation is still very well-defined and apparently undisturbed by the unstable region above.
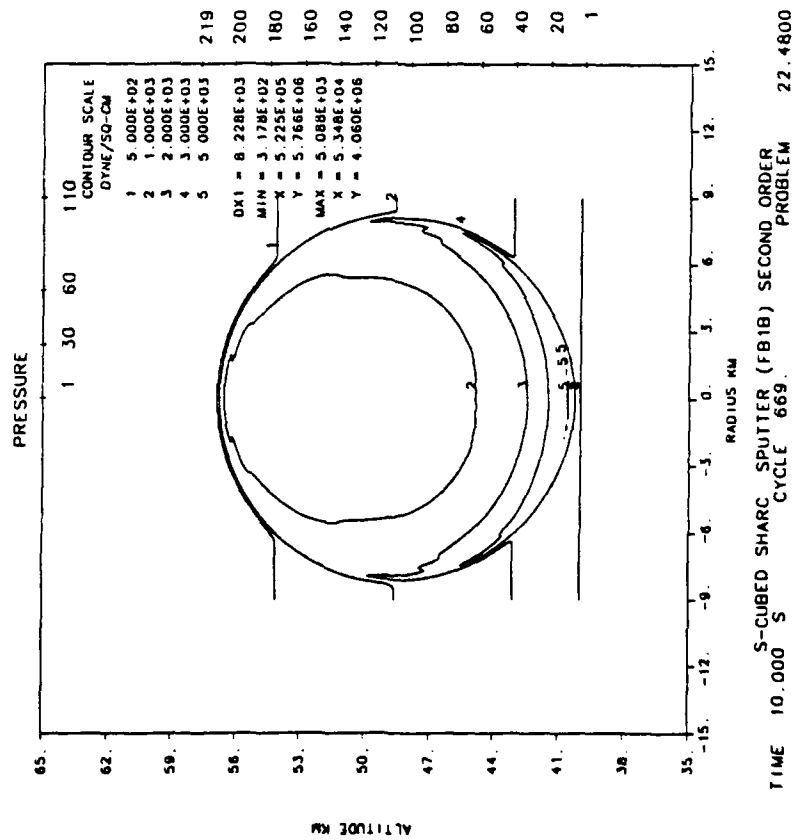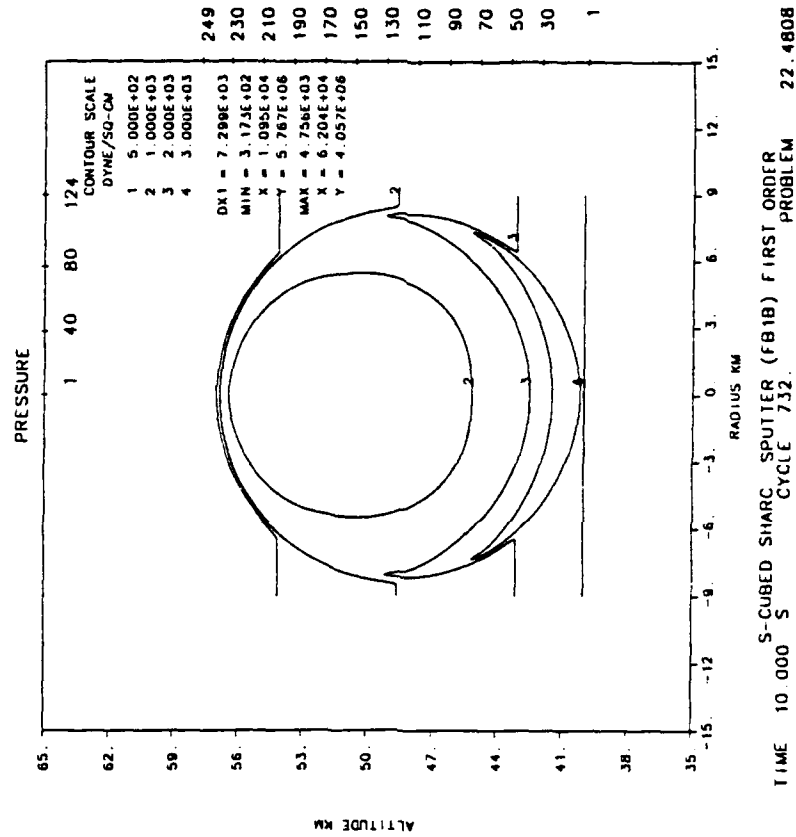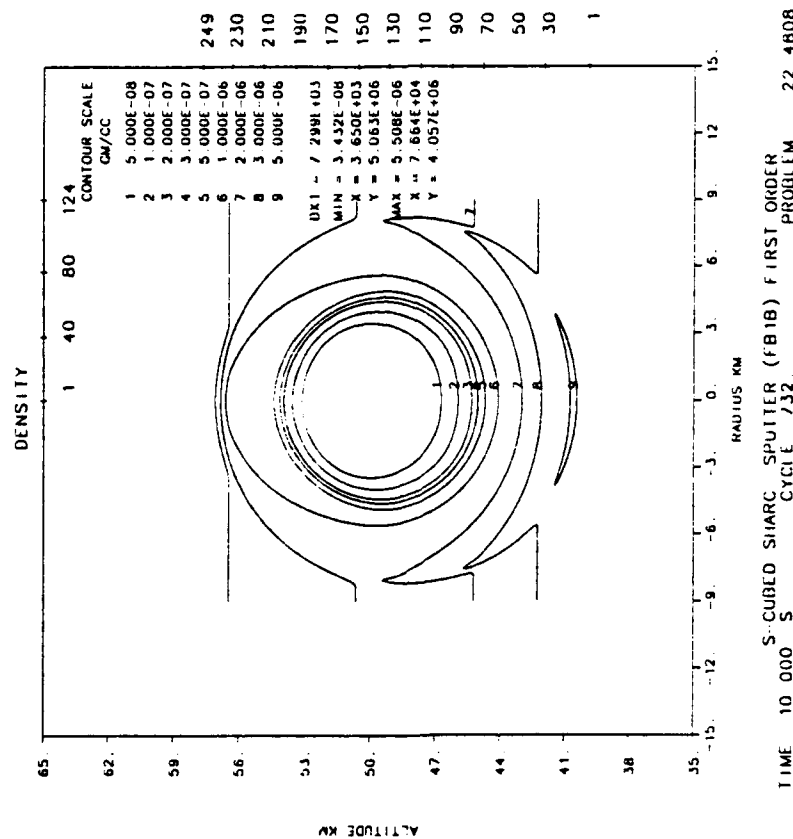
Figure 54. 200 KT at 50 km. Pressure contours at 10 seconds.

92
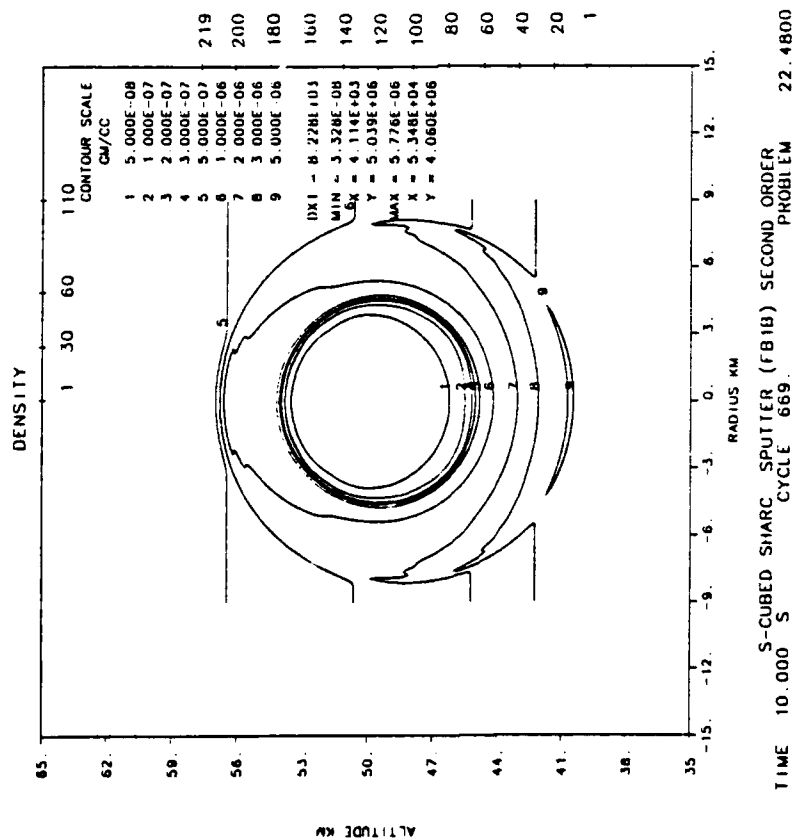
Second Order

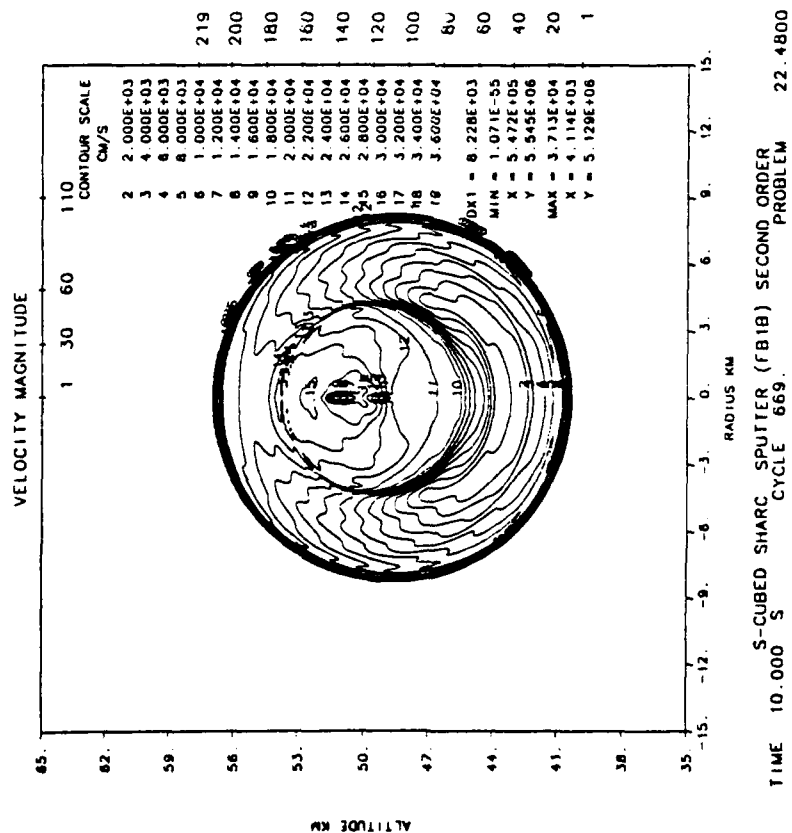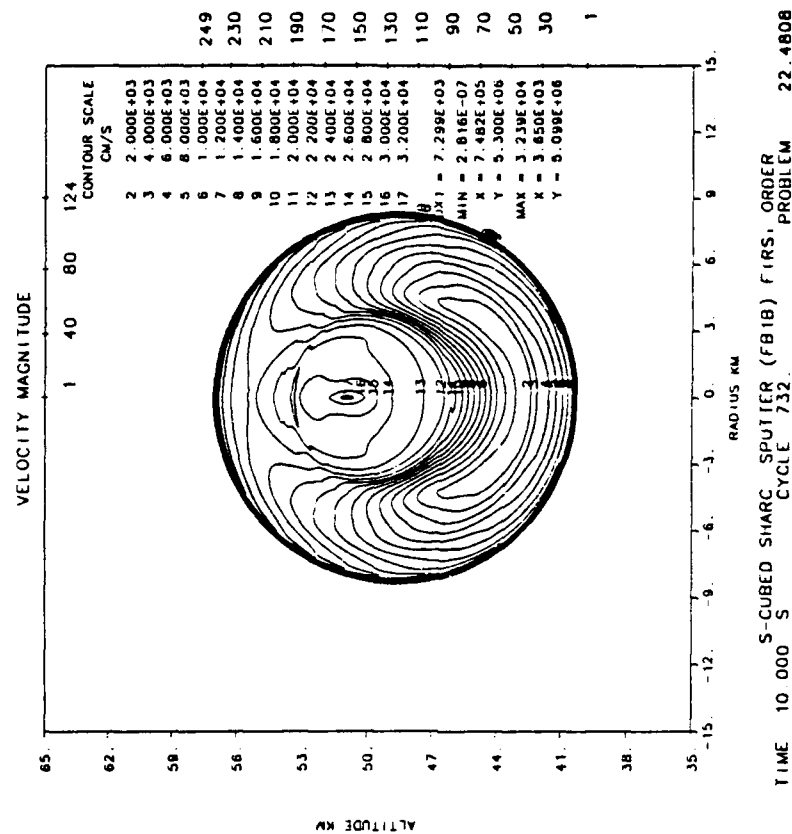## First Order

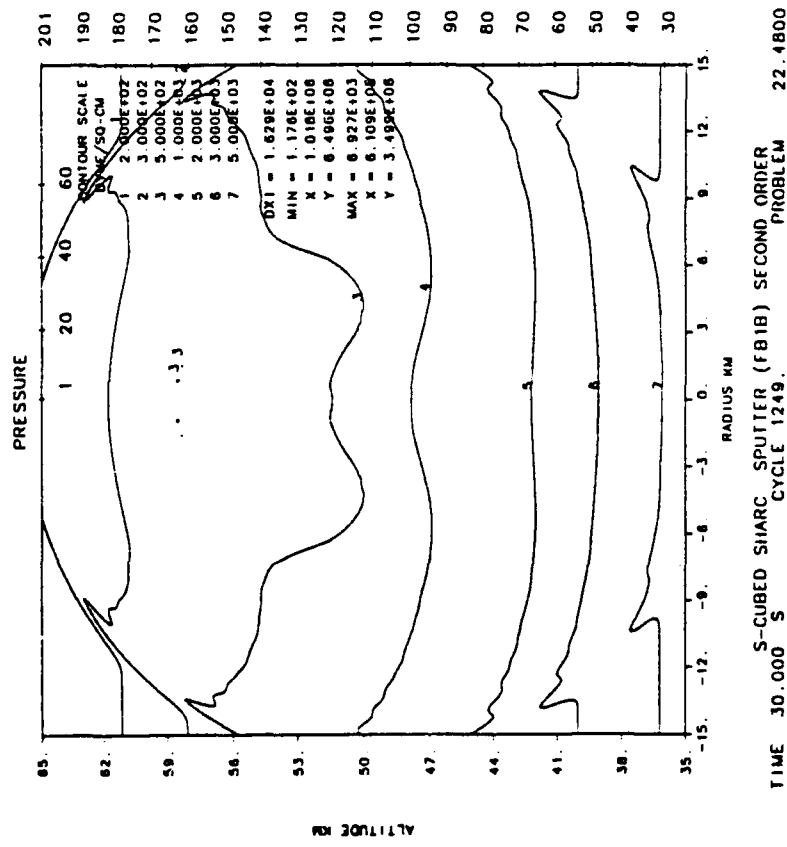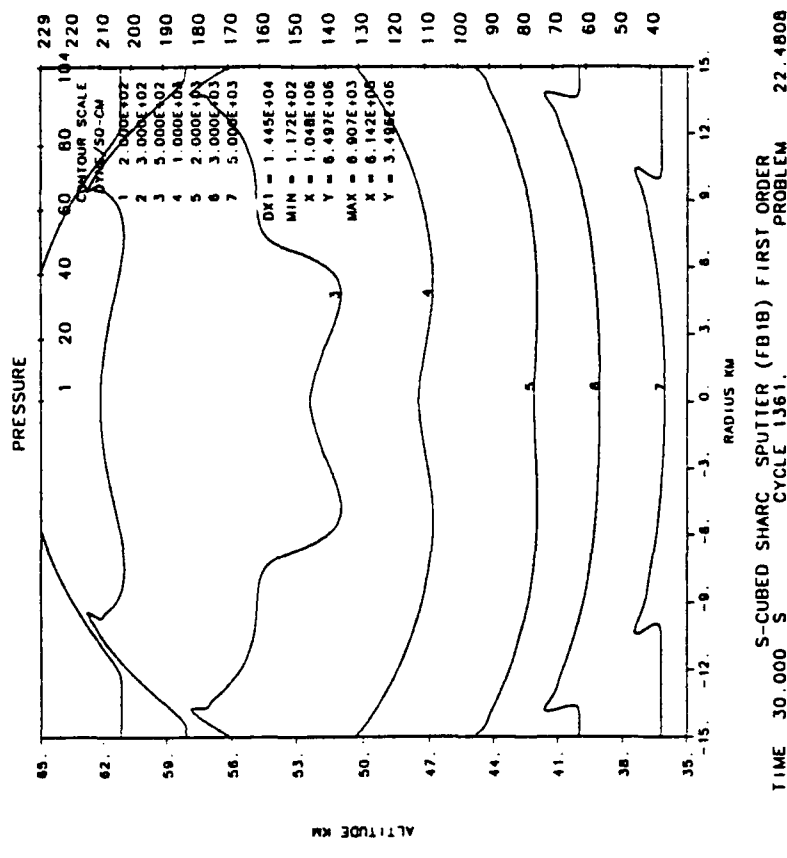Figure 55. 200 KT at 50 km. Density contours at 10 seconds.

First Order

Second Order

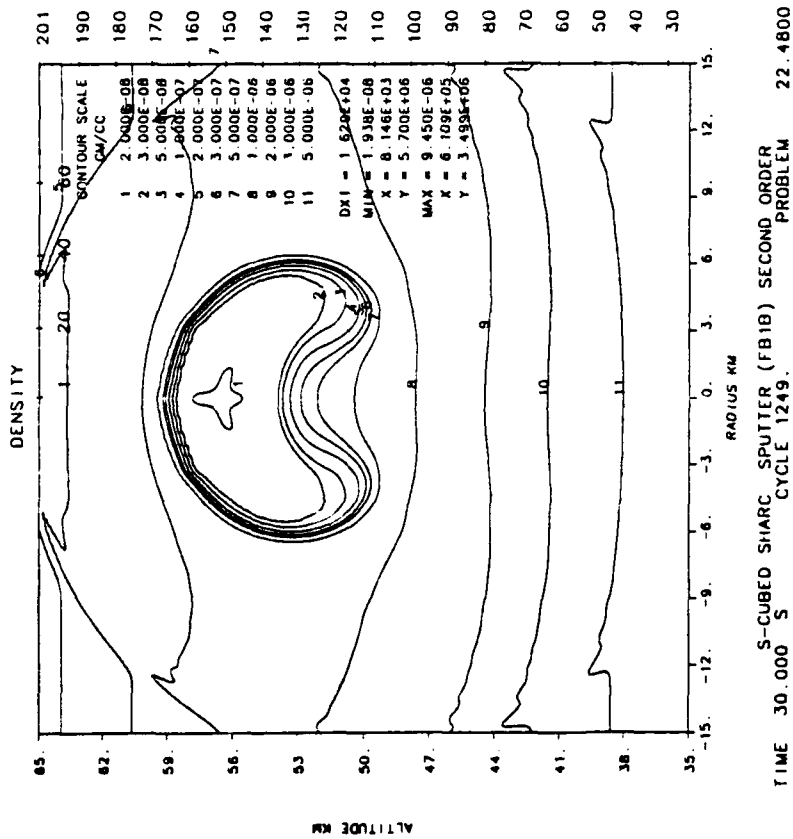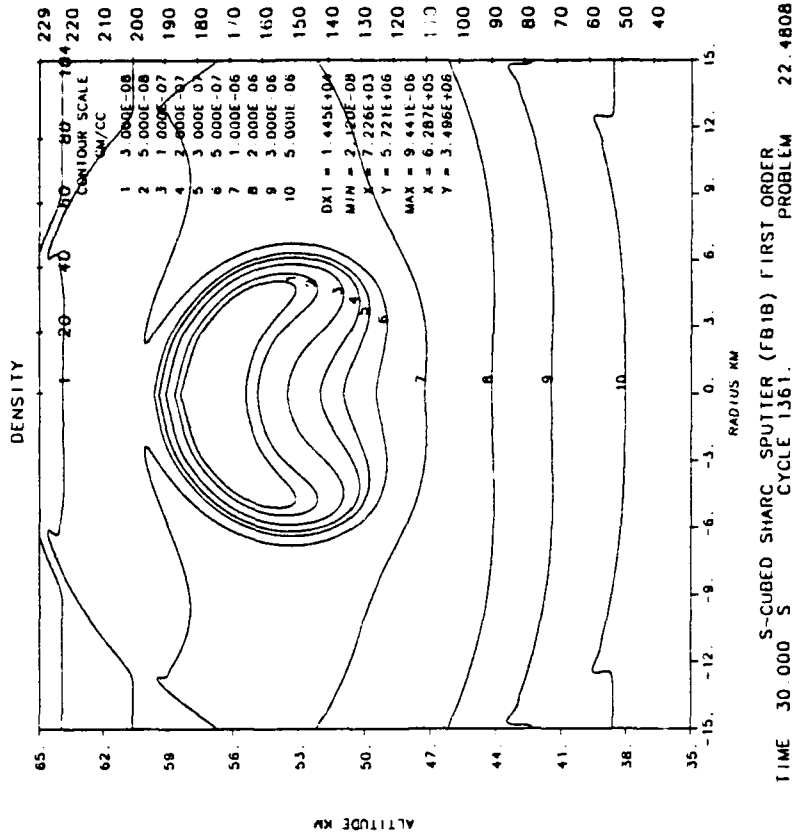Figure 56. 200 KT at 50 km. Velocity magnitude contours at 10 seconds.

94

First Order

Second Order

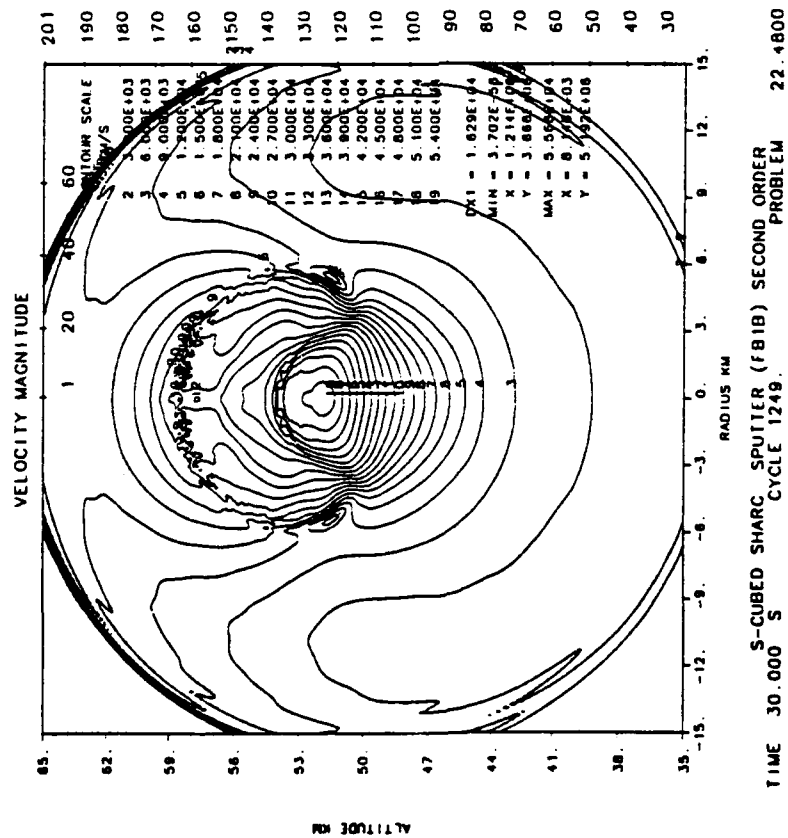Figure 57. 200 KT at 50 km. Pressure contours at 30 seconds.
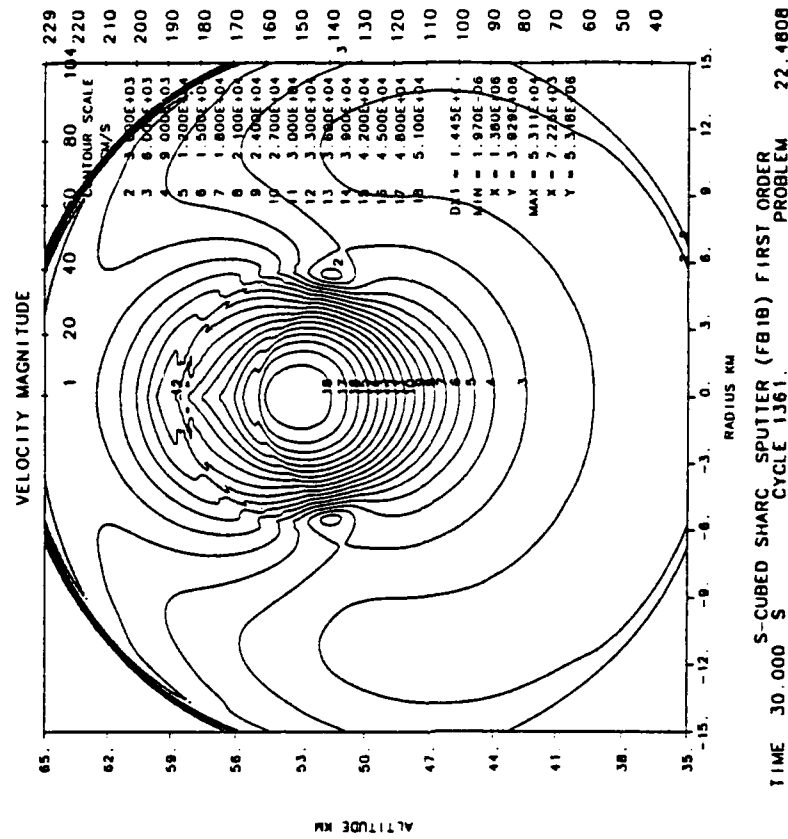
95

First Order

Second Order

Figure 58. 200 KT at 50 km. Density contours at 30 seconds.

96

First Order

Second Order

Figure 59. 200 KT at 50 km. Velocity magnitude contours at 30 seconds.

First Order

Second Order

Figure 60. 200 KT at 50 km. Pressure contours at 60 seconds.

98

Second Order

First Order

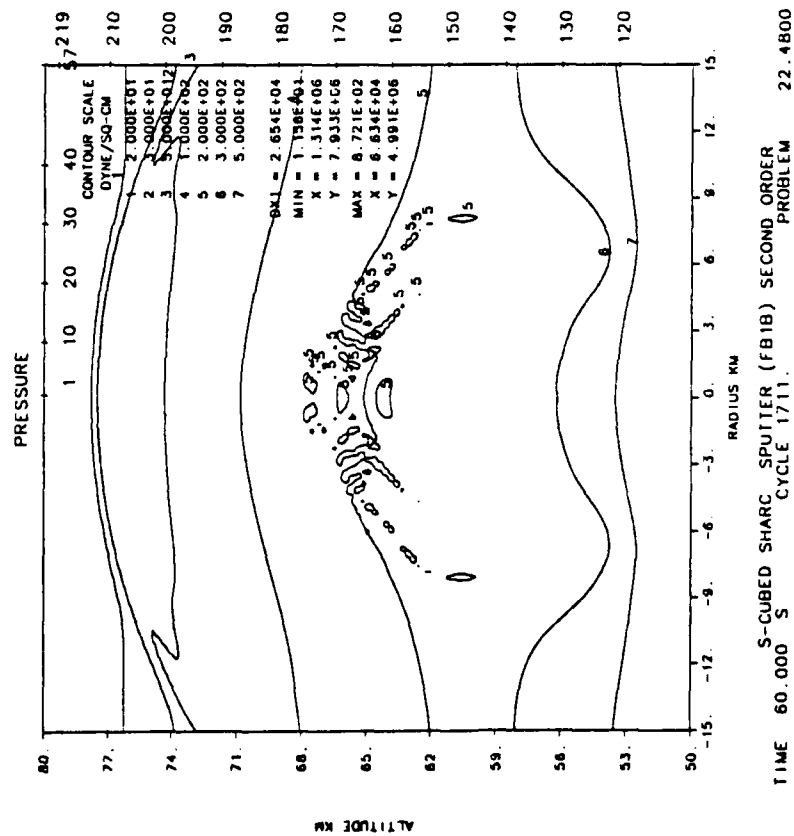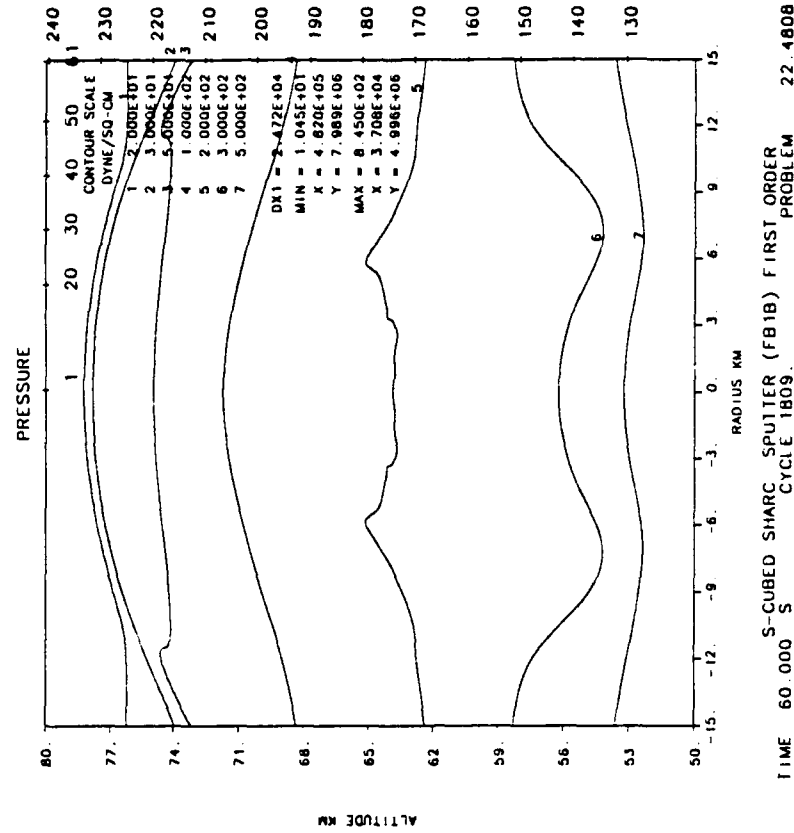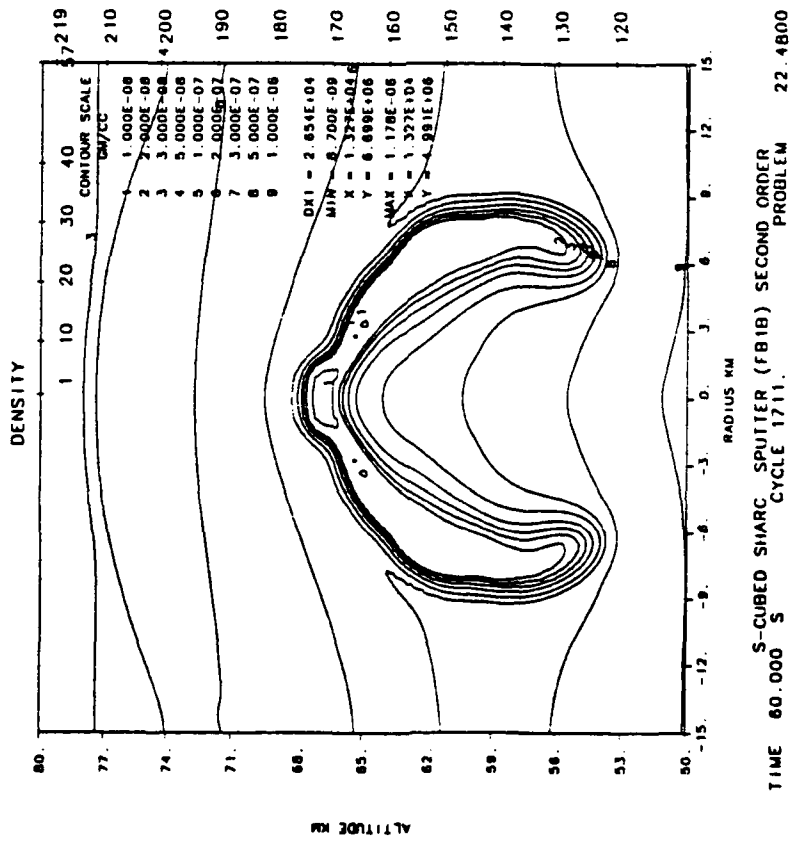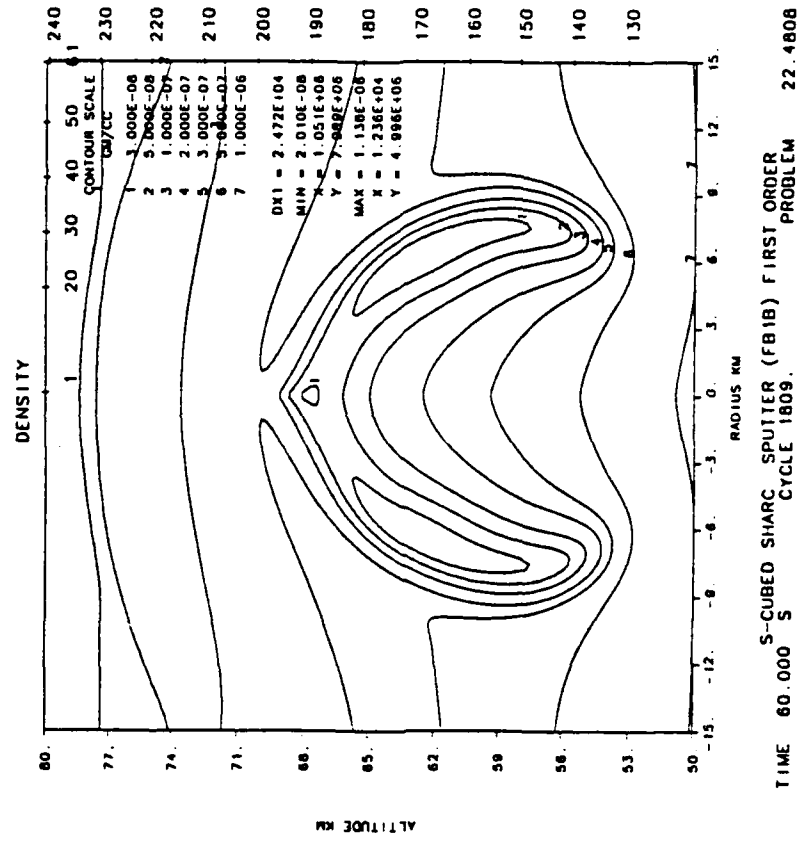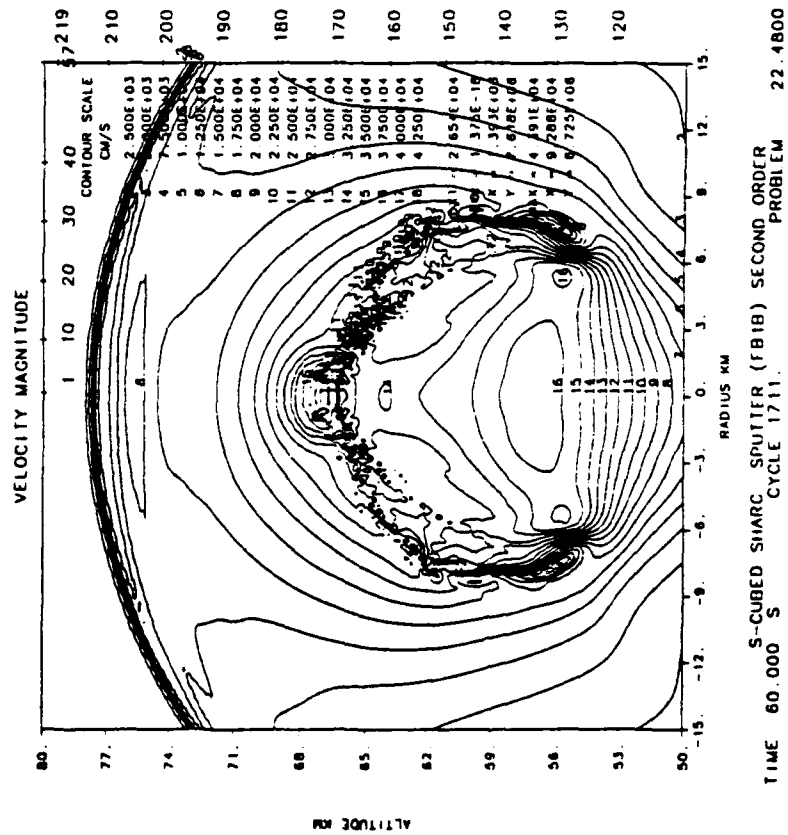Figure 61. 200 KT at 50 km. Density contours at 60 seconds.

99

First Order

Second Order

Figure 62. 200 KT at 50 km. Velocity magnitude contours at 60 seconds.

100
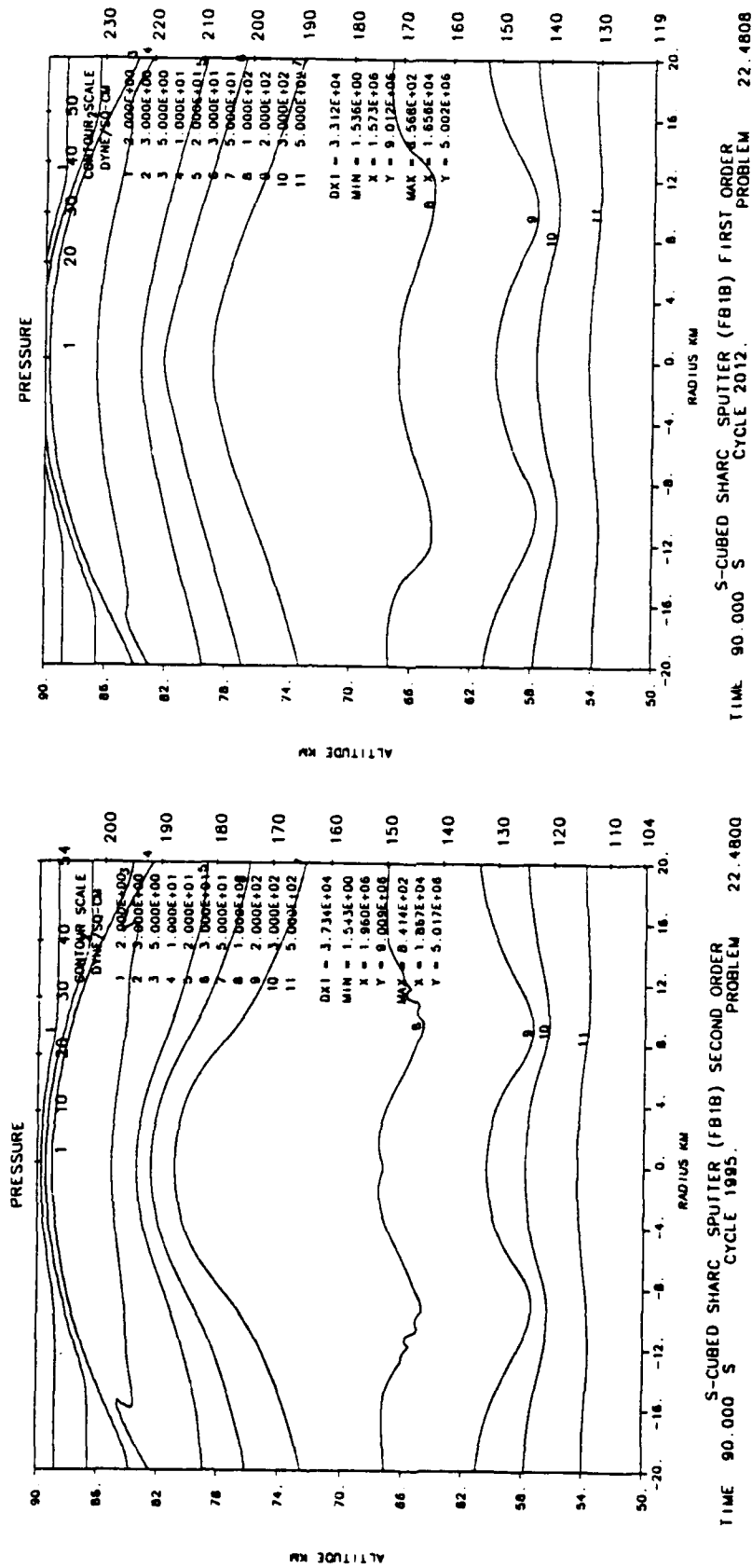
First Order

Second Order

Figure 63. 200 KT at 50 km. Pressure contours at 90 seconds.

101

First Order

Second Order

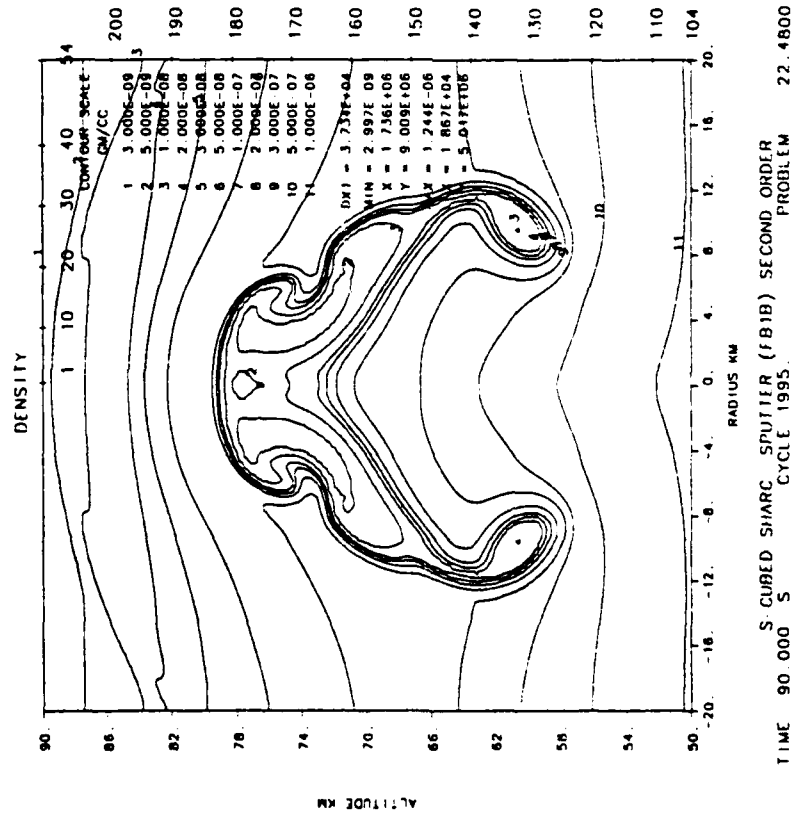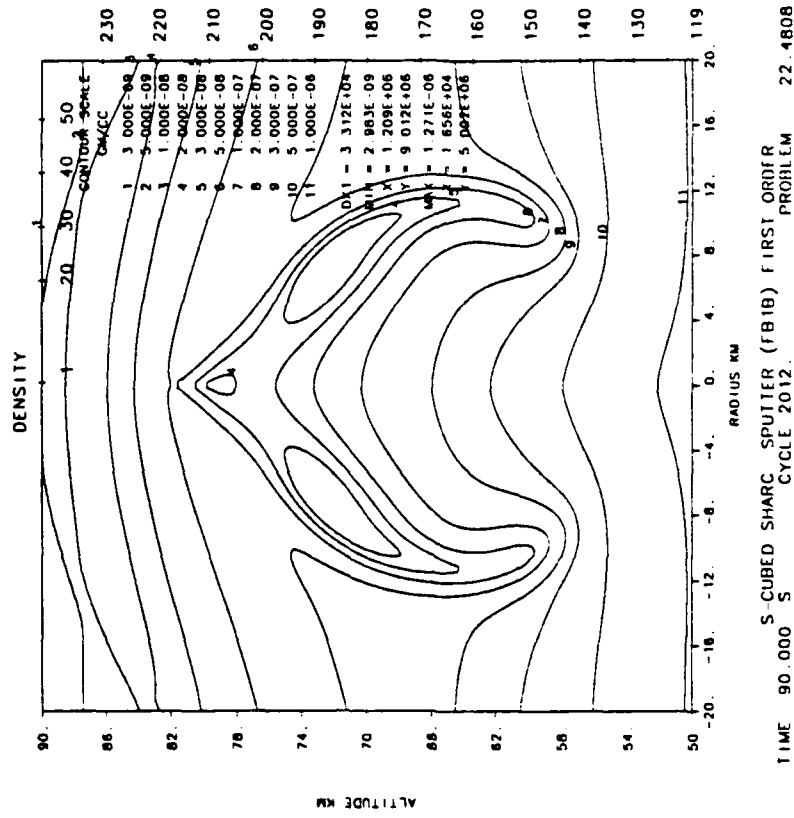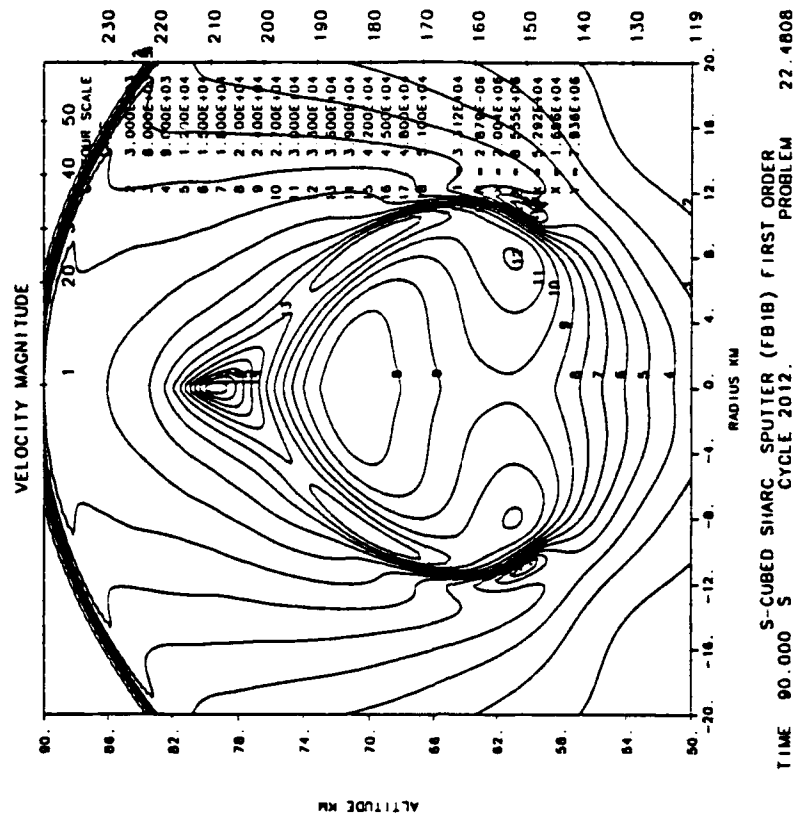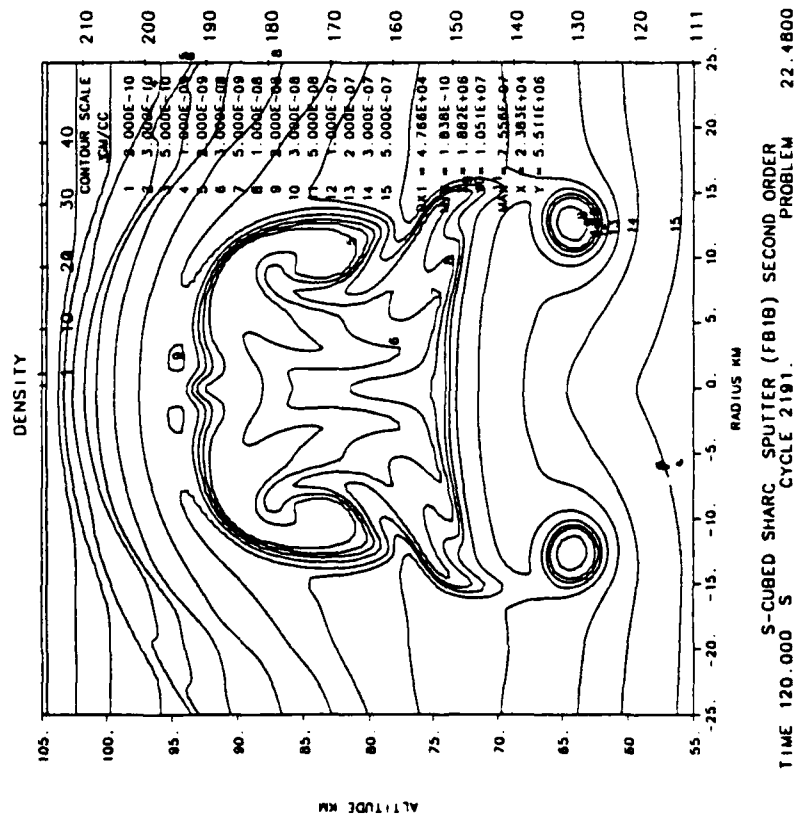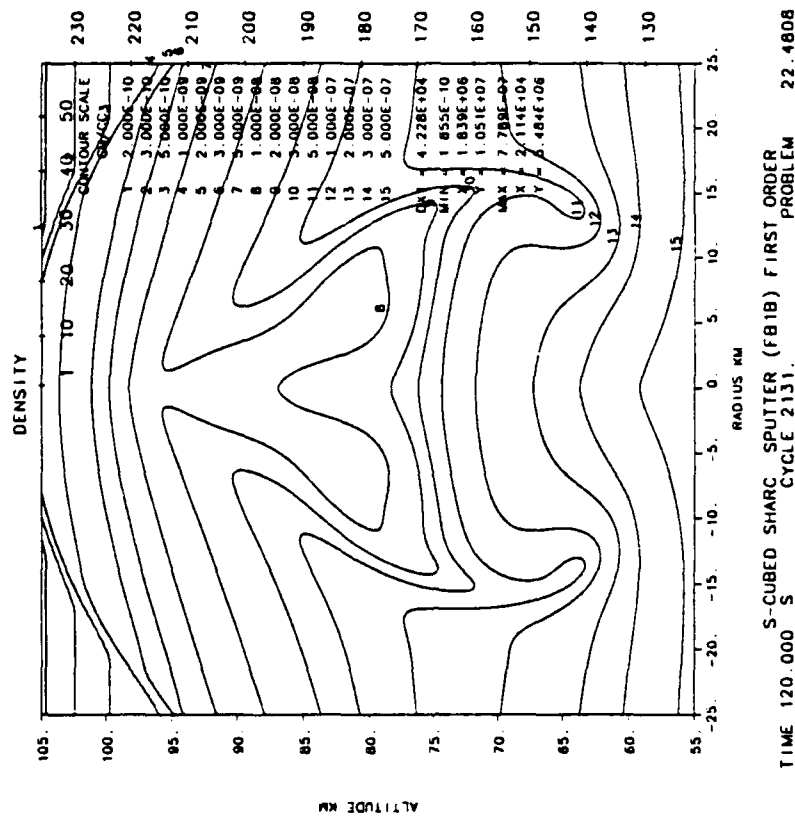Figure 64. 200 KT at 50 km. Density contours at 90 seconds.
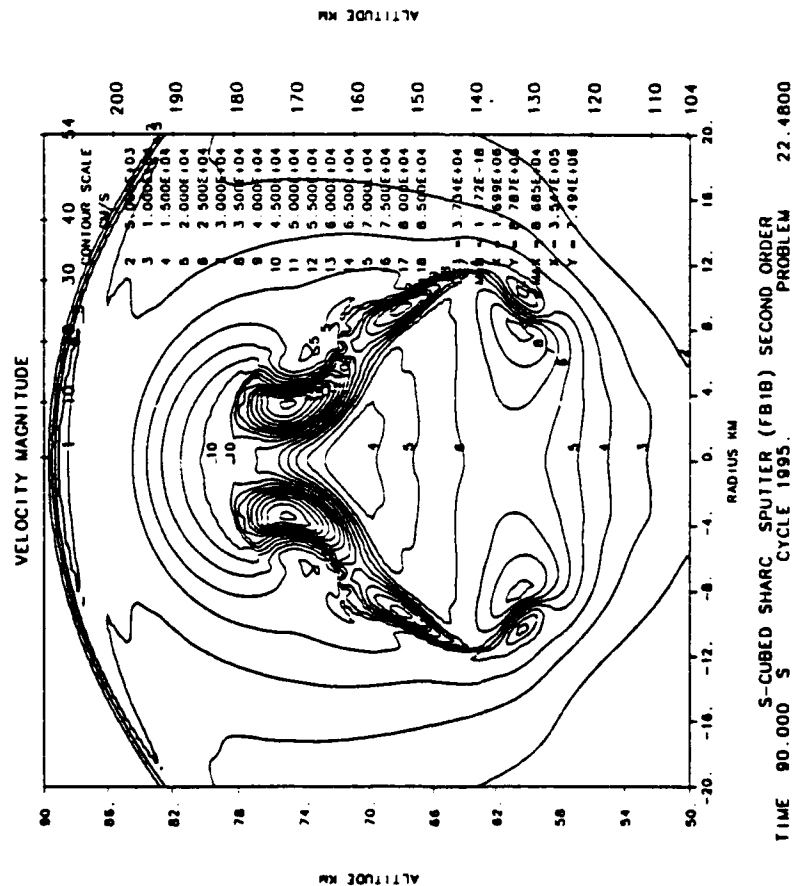
First Order

Second Order

Figure 65. 200 KT at 50 km. Velocity magnitude contours at 90 seconds.

First Order

Second Order

Figure 66. 200 KT at 50 km. Density contours at 120 seconds.

104

DISTRIBUTION LIST

DNA-TR-91-195

DEPARTMENT OF DEFENSE

ASSISTANT TO THE SECRETARY OF DEFENSE
    ATTN: EXECUTIVE ASSISTANT

DEFENSE ADVANCED RSCH PROJ AGENCY
    ATTN: CHIEF SCIENTIST

DEFENSE INTELLIGENCE AGENCY
    ATTN: DB-6

DEFENSE NUCLEAR AGENCY
    ATTN: OPNA
    ATTN: RAAE
3 CYS ATTN: RAAE K SCHWARTZ
    ATTN: RAAE D RIGGIN
    ATTN: RAAE S BERGGREN
    ATTN: T BAZZOLI
2 CYS ATTN: TITL

DEFENSE TECHNICAL INFORMATION CENTER
2 CYS ATTN: DTIC/FDAB

FIELD COMMAND DEFENSE NUCLEAR AGENCY
    ATTN: FCNM
2 CYS ATTN: FCTT W SUMMA

STRATEGIC DEFENSE INITIATIVE ORGANIZATION
    ATTN: EN
    ATTN: EN LTC C JOHNSON
    ATTN: TDW

THE JOINT STAFF
    ATTN: JKC DNA REP
    ATTN: JKCS
    ATTN: JLWT THREAT ANALYSIS
    ATTN: JPEM

DEPARTMENT OF THE ARMY

U S ARMY ATMOSPHERIC SCIENCES LAB
    ATTN: SLCAS-AE DR NILES

U S ARMY FOREIGN SCIENCE & TECH CTR
    ATTN: AIFRTA

U S ARMY STRATEGIC DEFENSE CMD
    ATTN: CSSD-H-SA
    ATTN: CSSD-H-SAV
    ATTN: CSSD-SA-EV RON SMITH

U S ARMY STRATEGIC DEFENSE COMMAND
    ATTN: CSSD-TD W O DAVIES

USA SURVIVABILITY MANAGMENT OFFICE
    ATTN: SLCSM-SE J BRAND

DEPARTMENT OF THE NAVY

OFFICE OF NAVAL RESEARCH
    ATTN: A TUCKER

SPACE & NAVAL WARFARE SYSTEMS CMD
    ATTN: G BRUNHART
    ATTN: S KEARNEY

THEATER NUCLEAR WARFARE PROGRAM OFC
    ATTN: D SMITH

DEPARTMENT OF THE AIR FORCE

AIR FORCE CTR FOR STUDIES & ANALYSIS
    ATTN: AFCSA/SAMI

AIR FORCE OFFICE OF SCIENTIFIC RSCH
    ATTN: AFOSR/NP

AIR UNIVERSITY LIBRARY
    ATTN: AUL-LSE

DEPARTMENT OF ENERGY

LOS ALAMOS NATIONAL LABORATORY
    ATTN: R W WHITAKER

SANDIA NATIONAL LABORATORIES
    ATTN: D DAHLGREN 6410
    ATTN: DIV 9014 R BACKSTROM

OTHER GOVERNMENT

CENTRAL INTELLIGENCE AGENCY
    ATTN: OSWR/NED
    ATTN: OSWR/SSD L BERG

DEPARTMENT OF DEFENSE CONTRACTORS

AEROSPACE CORP
    ATTN: C CREWS

ATMOSPHERIC AND ENVIRONMENTAL RESEARCH INC
    ATTN: M KO

AUSTIN RESEARCH ASSOCIATES
    ATTN: J THOMPSON

BDM INTERNATIONAL INC
    ATTN: W LARRY JOHNSON

BERKELEY RSCH ASSOCIATES, INC
    ATTN: J WORKMAN
    ATTN: S BRECHT

GENERAL RESEARCH CORP INC
    ATTN: J EOLL

INSTITUTE FOR DEFENSE ANALYSES
    ATTN: E BAUER

JAYCOR
    ATTN: J SPERLING

KAMAN SCIENCES CORP
    ATTN: DASIAC
    ATTN: E CONRAD
    ATTN: G DITTBERNER

KAMAN SCIENCES CORPORATION
    ATTN: B GAMBILL
    ATTN: DASIAC
    ATTN: R RUTHERFORD

LOCKHEED MISSILES & SPACE CO, INC
    ATTN: R SEARS

LOCKHEED MISSILES & SPACE CO, INC
    ATTN: D T RAMPTON

LOGICON R & D ASSOCIATES
    ATTN: D CARLSON
    ATTN: S WOODFORD

LOGICON R & D ASSOCIATES
    ATTN: J WALTON

MISSION RESEARCH CORP
    ATTN: J KENNEALY
    ATTN: R ARMSTRONG
    ATTN: S DOWNER
    ATTN: W WHITE

MISSION RESEARCH CORP
    ATTN: R L BOGUSCH

MISSION RESEARCH CORP
    ATTN: DAVE GUICE

MISSION RESEARCH CORP
    ATTN: B R MILNER
    ATTN: D LANDMAN
    ATTN: R BIGONI
    ATTN: R DANA
    ATTN: S GUTSCHE
    ATTN: TECH LIBRARY

PACIFIC-SIERRA RESEARCH CORP
    ATTN: H BRODE

RJO ENTERPRISES/POET FAC
    ATTN: STEVEN KRAMER

S-CUBED
    4 CYS ATTN: C NEEDHAM
    2 CYS ATTN: T CARNEY

SCIENCE APPLICATIONS INTL CORP
    ATTN: D SACHS

SPARTA INC
    ATTN: K COSNER

SPARTA INC
    ATTN: D DEAN

SRI INTERNATIONAL
    ATTN: W CHESNUT

TELEDYNE BROWN ENGINEERING
    ATTN: J WOLFSBERGER JR
    ATTN: RONALD E LEWIS

TOYON RESEARCH CORP
    ATTN: J ISE

VISIDYNE, INC
    ATTN: J CARPENTER